

**NOVEL EFFECTS IN WAVEGUIDE
SECOND HARMONIC GENERATION**

by

CARLOS GERARDO TREVIÑO-PALACIOS
B.Ph. Universidad Nacional Autónoma de México, 1990
M.S.(Optica) Centro de Investigaciones en Optica, 1992
M.O.S.E. University of Central Florida, 1994

A dissertation submitted in partial fulfillment of the requirements
for the degree of Doctor of Philosophy in Optical Science and Engineering
in the Department of Electrical and Computer Engineering
in the College of Engineering
at the University of Central Florida
Orlando, Florida

Spring Term
1998

Major Professor: George I. Stegeman

UNIVERSITY OF CENTRAL FLORIDA
DISSERTATION APPROVAL

Date: March 3, 1998

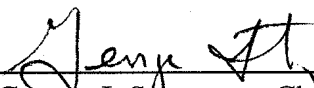
I hereby recommend that the dissertation prepared and successfully defended under my supervision entitled: Novel Effects in Waveguide Second Harmonic Generation

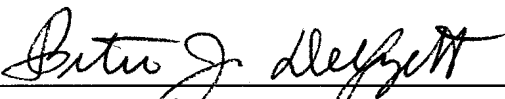
by: Carlos G. Treviño-Palacios

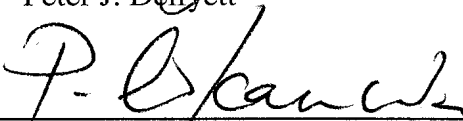
be accepted in partial fulfillment of the requirements for the degree of

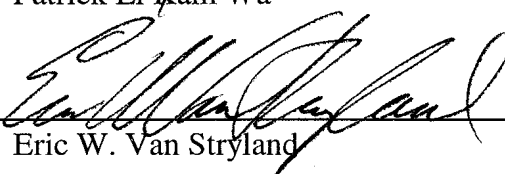
Doctor of Philosophy in Optical Science and Engineering

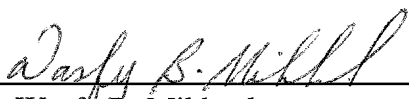
from the Department of Electrical Engineering, College of Engineering.

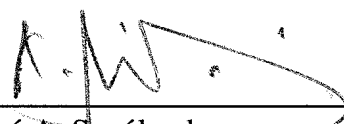

George I. Stegeman, Chair



Peter J. Delfyett


Patrick Li Kam Wa



Eric W. Van Stryland


Wasfy B. Mikhael
Department Chair


José A. Sepúlveda
Director of Graduate Affairs


Martin P. Wanielista
Dean

FINAL EXAMINATION COMMITTEE


Diane M. Jacobs
Vice President for Research and
Graduate Studies

The material presented within this report does not necessarily reflect the opinion of the committee, the College, or the University of Central Florida.

© 1998 Carlos G. Treviño-Palacios

ABSTRACT

Research which resulted in the identification of novel effects in waveguide second harmonic generation is presented in this dissertation. This work started with the investigation of experimental and numerical inconsistencies in the second harmonic generation (SHG) process which were at variance with traditional concepts of SHG. Some of these inconsistencies were caused by conditions usually overlooked when studying SHG in waveguides that support many modes or the SHG field evolution in waveguides with a spatially nonuniform-nonsymmetrical distribution of parameters along the light propagation path.

Examining second harmonic generation in detail for these conditions led to the identification of two fundamental effects in waveguide second harmonic generation, namely waveguide multimode competition and spatial nonreciprocity. This research has led to additional mathematical tools for investigating the evolution of second harmonic fields when the key parameters have a spatially nonuniform distribution along the propagation path further.

For SHG in waveguides that support many modes, some of the general features that we found are that the wavelength and peak conversion efficiency for different harmonic modes changes with input fundamental intensity and that power-dependent competition occurs between them at high powers. This is an important effect to consider, and if possible avoid, in the design of waveguides to be used for harmonic generation.

For the evolution of SHG fields in waveguides with spatially nonuniform-nonsymmetrical distributions of parameters along the propagation path we found that the SHG output depends on the direction into which the fundamental is launched and hence is spatially nonreciprocal. This opens the possibility for an optical diode using second order processes. In a more general context the results obtained are encouraging for the pursuit of all-optical switching devices at room temperature based on cascading, and for new ways of enhancing the SHG bandwidth, etc. by controlling the SHG evolution with an arbitrary, nonuniformly chirped grating.

To my mother

To my friends

"The finest emotion of which we are capable is the mystic emotion. Herein lies the germ of all art and all true science. Anyone to whom this feeling is alien, who is no longer capable of wonderment and lives in a state of fear is a dead man. To know that what is impenetrable for us really exists and manifests itself as the highest wisdom and the most radiant beauty, whose gross forms alone are intelligible to our poor faculties - this knowledge, this feeling ... that is the core of the true religious sentiment. In this sense, and in this sense alone, I rank myself among profoundly religious men"

Albert Einstein
What I Believe (1930).

ACKNOWLEDGEMENTS

How can I acknowledge the many people that contributed to this work? What is an acknowledgement anyway? It is a way for me to credit the - sometimes undeserved - contribution either personal or professional made by a person; even if they were not aware of it. It is impossible to account the many people that, for the last five years, have made me feel at home - away from home -. Risking the involuntary omission of some names I will try to list a few of them.

I guess the words, “Get the hell out of here!,” from the people back home were the first encouraging words I, now, gratefully acknowledge. My mother, my sibyls (Leonardo, Ariadna and Aliata) with their respective smurfs (Aliatar and Darian), as well as the rest of my family, said these same words over and over. Thank you for not allowing me to quit even before I started. These words were repeated by the gang back home: Pedro A., Juan and Edna, Carlos del Castillo, Claudia, Gerardo, Miriam, the Ortíz-clan, and all the others in the F-less club. Jordi, Gonzalo, and Armando also spoke these words quite eloquently. From the people at the INAOE expressed the same support by saying, “let’s see who finish first” (for the record: *I lost*). This group includes Ruben and Emilia Ramos, David and Gloria Iturbe, Miguel and Leonor Torres, Edgar Alvarado, Magarita Ojeda, and Jose Luis Juarez. I guess Eunice was also there at the beginning. Dr. Jose Javier Sanchez-Mondragon was quite arduous in the use of the same words, and supported me more than once. In memorium to Dr. Gustavo Torres-Cisneros who expressed his support in a different way, “Go out and have fun. See you back soon.”

Here in Orlando the names are even harder to distinguish and list all the people that contributed is impossible. Matthias Jäger, Brian Lawrence, Vincent Ricci, and Lars Friedrich were a constant factor in improving professionally; and, a few beers later, didn’t allow me to become a complete nerd. The people in the lab that showed me the correct meaning of “work after hours”, as well as the difference between a “switch-hitter” and a “double-sided-batman”: Yongsoon, Mike, María, Jin, Myoungsik, Dug, Stefan, Armin, Jim Wilson, Russell (baseball requirement completed), and Jim Ross (I swear I didn’t ride in a vegetable truck!).

The post-docs from which I learned a few experimental tricks (among other things): Peter Wigley, Pascal Baldi, Luca Baraldi, Gijs Krijnen, Yoshiyasu Ueno, Lluís Torner, William Torruellas, Alain Villeneuve, Mingguo Liu, Hoon Shim, Michael Canva, Johannes Moll, Gaetano Assanto, and Roland Schieck. Outside the laboratory to some fellows that showed me how to enjoy life: Arnold Daniels, Mike Hasselback, Alexandra, Irina, Brian Mathason, Steve Dunn, Steve Grantham, Thierry, Carl, Todd, and Fred Smith (still can't believe he went white-water rafting), among others. Jamie and Tomas O'Neal deserve particular mention in this marathonic work to help me fighting the crusade against bureaucracy, taught me how to sail, and allowed me to eat descent food once in a while. Also, thanks to those guys that share with me a perspective on the world, and didn't allow me to become a whuffo: Lexi and Shane, Sean, Alex, Eli, Bill Coutu, Bill and Magan Snow, Jeff, Stu, Rocky and Patty Evans, Bill and Conie, and Andy (I owe you one).

To my advisor, Professor George I. Stegeman, I can't find all the right words to thank him for his friendship, the knowledge obtained, and the opportunity to share a great time with so many good people (BTW: it is "Chore", not "Corche"). Thank you also for trusting me even after one too many games of minesweeper. I must extend my appreciation to the members of my doctoral committee: Professors Eric Van Stryland, Patrick Li Kam Wa, and Peter Delfyett. The time they spent over the years to answer some of my philosophical questions helped form the ideas presented in this work. In addition to my advisor and committee member, several other people helped me along the journey: Dr. Mark De Micheli, Daniel Ortega, and Dr. Stewart Aitchinson for the experimental samples used in this work. Dr. Marcela del Rio for showing me that anybody can be an actor. And to all the great faculty, students and staff at CREOL whose names I'll always remember with a smile, thanks. There are a great many more names that I could add to this list, but while their contribution are not individually identified, I am no less thankful for their help.

Finally, from Mexico, the support from the "Consejo Nacional de Ciencia y Tecnología" through the Fullbrighth-CONACyT scholarship program, and the "Instituto Nacional de Astrofísica, Óptica y Electrónica" through the "Programa de Superación Académica" provided me with the means to complete this work.

TABLE OF CONTENTS

| | |
|--|----|
| LIST OF TABLES | x |
| LIST OF FIGURES | xi |
| CHAPTER 1 INTRODUCTION | 1 |
| 1.1 Scope of Research | 5 |
| CHAPTER 2 THEORY OF CASCADED SECOND ORDER NONLINEARITIES ... | 7 |
| 2.1 Review of Nonlinear Optics | 9 |
| 2.2 Second Harmonic Generation | 16 |
| 2.3 Physics of Cascading | 23 |
| 2.4 Characteristic Lengths | 41 |
| 2.5 Phase-Matching Techniques | 51 |
| CHAPTER 3 WAVEGUIDE SHG MULTIMODE COMPETITION | 57 |
| 3.1 Review of Waveguides | 59 |
| 3.2 Waveguide SHG | 64 |
| 3.3 Numerical Simulations in the Multimode Domain | 68 |
| 3.4 Experimental Setup | 75 |
| 3.5 Experimental Measurements | 77 |
| 3.6 Higher Harmonic Generation | 84 |
| 3.7 Limits of Influence of the Multimode Competition | 88 |

| | |
|--|-----|
| CHAPTER 4 SHG SPATIAL NONRECIPROCITY | 89 |
| 4.1 Intuitive Explanation for Spatial Nonreciprocity | 92 |
| 4.2 Coupled Mode Equations for Nonuniform profiles | 95 |
| 4.3 Numerical Calculations on a Step Profile | 101 |
| 4.4 Experimental Results on a Step Profile | 105 |
| CHAPTER 5 SPATIAL NONUNIFORM PROFILES | 112 |
| 5.1 Low Depletion SHG Detuning Curve from a Known Profile | 113 |
| 5.2 Numerical Calculations for Arbitrary Nonuniform Profiles | 117 |
| 5.3 Inverse Problem | 125 |
| 5.4 Experimental Results in a General Profile | 131 |
| CHAPTER 6 CONCLUSIONS | 141 |
| 6.1 Summary of Results | 142 |
| REFERENCES | 146 |

LIST OF TABLES

| | |
|--|----|
| 2.1 Comparison between characteristic lengths for low and high power beams | 52 |
|--|----|

LIST OF FIGURES

| | | |
|-----|---|----|
| 2.1 | Schematic representation of the physical origin of the nonlinear phase shift on the fundamental wave due to cascading. v_1 and v_2 are the phase velocities of the fundamental and SH respectively. | 24 |
| 2.2 | (a) Nonlinear phase shift $\Delta\phi_{\text{NL}}$ and (b) normalized fundamental intensity as a function of the normalized propagation z/L for various wavevector detunings. In both cases $\kappa A_\omega(0)L = 20$ | 29 |
| 2.3 | Intensity dependence of (a) nonlinear phase shift $\Delta\phi_{\text{NL}}$ and (b) normalized fundamental intensity as a function of the input fundamental intensity $ A_\omega(0) ^2$ for different wavevector detunings. In each cases $\kappa L = 4$ | 31 |
| 2.4 | Typical variation in (a) the nonlinear phase shift $\Delta\phi_{\text{NL}}(L)$ and (b) SHG versus detuning from phasematch $\Delta k_0 L$ for different input parameters. | 33 |
| 2.5 | Phase matching vector diagram for (a) birefringent phasematching, (b) non-phasematched case and (c) quasi-phasematching. | 55 |
| 3.1 | (a) Channel and (b) planar waveguide typical geometries. In both cases: $n > n_s, n_c$. . . | 60 |
| 3.2 | Slab waveguide (a) TM and (b) TE vectors (left) and typical electric field mode profiles (right). | 61 |
| 3.3 | Variation in the effective refractive index N_{eff} with normalized film thickness for the first two TE and TM modes for a slab waveguide with substrate index n_s , film index n_o , and film thickness h | 63 |
| 3.4 | (a,c,e) SHG detuning curve and (b,d,f) total nonlinear phase shift for different input powers. (a,b) $I_o = 0.25$, (c,d) $I_o = 1.0$, and (e,f) $I_o = 2.25$. In all cases $\kappa_1 L = 4$, $\kappa_2 L = 4$, and $\Delta K_0 L = 2\pi$. The arrows show phasematching position for each independent mode interaction. | 71 |
| 3.5 | (a,b) SHG detuning curve and (c,d) nonlinear phase shift for two independent mode interactions. Low power interaction are shown on the left hand side, and high power interaction are shown on the right hand side. Notice the nonzero phase shift from one interaction in the phasematching condition for the other. | 73 |
| 3.6 | Experimental setup used to characterize $\chi^{(2)}$ waveguides. | 76 |

| | | |
|------|--|-----|
| 3.7 | Wavelength scans in a LiNbO ₃ QPM 4 μm width waveguide at different peak power in the vicinity of the TM ₀₀ (ω) → TM ₀₁ (2ω) + TM ₂₀ (2ω). Solid (dotted) arrows track the position of the peak conversion to the TM ₀₁ (2ω) (TM ₂₀ (2ω)) mode. | 79 |
| 3.8 | (a) TM ₀₁ (2ω) and (b) TM ₂₀ (2ω) mode profiles correspondent to Figure 3.7. | 80 |
| 3.9 | Wavelength scans in a LiNbO ₃ QPM 4 μm width waveguide at different peak power in the vicinity of the interaction TM ₀₀ (ω) → TM ₀₂ (2ω) + TM ₄₀ (2ω) + TM ₂₁ (2ω). These curves were normalized to the solid arrow points in . Solid (dotted and dashed) arrows track the position of the peak conversion to the TM ₀₂ (2ω) (TM ₄₀ (2ω) and TM ₂₁ (2ω)) mode. | 81 |
| 3.10 | (a)TM ₂₁ (2ω), (b)TM ₄₀ (2ω), and (c)TM ₀₂ (2ω) mode profiles for 3.9 . . . | 82 |
| 3.11 | Low depletion detuning SHG curve in the vicinity of the interaction between TM ₀₀ and TM ₁₀ fundamental modes and (a) TM ₂₂ , (c) TM ₁₁ , (e) TM ₀₁ , (g) TM ₃₀ , and (i) TM ₄₀ second harmonic modes. Modes in (b), (d), (f) and (h) represent mixed modes. The inset show a binary representation of the mode profiles at the position shown by the arrows. | 83 |
| 3.12 | Spectral scan of generated harmonics of 1619.4 nm color center laser source in a 6 μm mask width QPM PE LiNbO ₃ channel waveguide with 20 μm domain inversion period. | 86 |
| 4.1 | SHG detuning curve in a 3 μm by 2 μm waveguide PE-QPM LiNbO ₃ . Notice the break up in the TM ₀₀ (ω)→ TM ₀₁ (2ω) resonance. The magnitude of the maximum conversion depends in the propagation direction (in coupling at end A or end B). | 91 |
| 4.2 | Local spatial second harmonic generation representation. | 93 |
| 4.3 | Directional response in symmetric and asymmetric structures. For symmetric structures the outcome will be the same (E ₁ '(ω,2ω) = E ₂ '(ω,2ω)) in both directions. For nonsymmetrical structures, in general may not be the same (E ₁ '(ω,2ω)≠E ₂ '(ω,2ω)). | 93 |
| 4.4 | Spatial nonuniform and nonsymmetrical dependence of wavevector mismatch and nonlinear strength used to observe nonreciprocal SHG. | 102 |
| 4.5 | SHG intensity detuning curves in the presence of a discontinuity at position L ₁ along propagation. Parameters used are: A _o =1, κ=1, L=1, ΔK(L ₁)=[K ₁ -K ₂]=5.65, where K ₁ = K(z) for 0<z<L ₁ and K ₂ = K(z) for L ₁ <z<L, and L ₁ = (a) 0, (b) 0.25L, (c) 0.50L, (d) 0.75L and (e) L. | 104 |

| | | |
|-----|--|-----|
| 4.6 | Wavelength scan of SHG in the LiNbO ₃ QPM waveguide showing a nonreciprocal behaviour in the (a) high and (b) low depletion regimes ($\eta_{\max} = 39\%$ and 0.8% respectively) without (dashed line) and with a layer of photoresist on half the waveguide for forward (open circles) and backward (solid circles) propagation. Solid arrows show phase matching in the region without photoresist. Dotted arrows show the phase-matching peak induced by the photoresist layer. | 106 |
| 4.7 | Comparison between (a) forward and (b) backward detuning curves in Figure 4.6. Effective conversion efficiencies are (a) 16.4% and 0.11% , and (b) 21% and 0.21% for high and low conversion efficiencies, respectively. | 108 |
| 4.8 | Theoretical curves (solid line) fitted to the experimental high power detuning curve (closed circles) from 2 for the case of (a) backward and (b) forward propagation. Complementary calculations (forward for (a) and backward for (b)) are shown as dashed lines for comparison. Parameters used are $A_0=1$, $L=1$, $\Delta K = 5.65$, with a change in nonlinear strength κ from 1 to 0.8 at $L_1=0.4L$ | 110 |
| 5.1 | Normalized SHG detuning curves in the low depletion regime for a uniform nonlinear strength and different nonuniform wavevector distribution along the axis of the form $K(z)=\beta(z-0.5)^n$. Values of $\beta = 21 \cdot 2^n$ for (a) $n = 0$, (b) $n = 1$, (c) $n = 2$, and (d) $n = 3$ were used. Solid lines were calculated solving with a fourth order Runge-Kutta method with $\kappa A_\omega(0) L = 0.04$. Dashed lines were calculated using the result | 119 |
| 5.2 | High depletion regime SHG detuning curves for a uniform nonlinear strength and different nonuniform wavevector distribution along the axis of the form $K(z)=\beta(z-0.5)^n$. Values of $\beta = 21 \cdot 2^n$ for (a) $n = 0$, (b) $n = 1$, (c) $n = 2$, and (d) $n = 3$ were used. Calculation was done solving with a fourth order Runge-Kutta method with $\kappa A_\omega(0) L = 4$ | 121 |
| 5.3 | Cascaded nonlinear phase shift corresponding to the curves in . A wavevector distribution along the axis of the form $K(z)=\beta(z-0.5)^n$ is assumed. Values of $\beta = 21 \cdot 2^n$ for (a) $n = 0$, (b) $n = 1$, (c) $n = 2$, and (d) $n = 3$ were used. Calculation was done solving with a fourth order Runge-Kutta method with $\kappa A_\omega(0) L = 4$ | 123 |
| 5.4 | Exact coupled mode equation solutions in the presence of a linear nonuniform wavevector variation in the in the low depletion regime ($\kappa A_\omega(0) L= 0.04$). (a) Fundamental intensity throughput, (b) second harmonic intensity generated, (c) fundamental cascaded nonlinear phase shift using the coupled mode equations type III (dashed) and type IV (solid), and (d) second harmonic nonlinear phase shift using the coupled mode equations type iii (dashed) and type iv (solid). | 127 |

| | | |
|------|---|-----|
| 5.5 | Result from the inverse problem method for (a) linear and (b) adiabatic spatial nonuniform profiles. Dashed line show the original profiles used to calculate the detuning curves using (5.1). Solid lines are the reconstruction using the inverse problem method. | 128 |
| 5.6 | Experimental uniform PSW SHG detuning curve. This curve is for a segmented grating period of 19 μm . A binary representation of the phasematched modes is also shown | 132 |
| 5.7 | Phase matching wavelenght vs. PSW grating period for the $\text{TM}_{00}(\omega) \rightarrow \text{TM}_{00}(2\omega)$ (dashed line), $\text{TM}_{00}(\omega) \rightarrow \text{TM}_{01}(2\omega)$ (solid line) and $\text{TM}_{00}(\omega) \rightarrow \text{TM}_{20}(2\omega)$ (dotted line). Average SHG conversion efficiencies for 100 W input fundamental are 0.09%, 1.5%, and 0.2%, respectively. The dash-dotted lines represents the PSW grating period range used in the nonuniform profile mask design. | 133 |
| 5.8 | Nonuniform profiles engineer in a chirped PSW. (a) Quadratic grow (design1), (b) quadratic grow with a sharp discontinuity (design 2), and (c) quadratic grow without the discontinuity (design 3). | 135 |
| 5.9 | Experimental detuning curves for the spatial nonuniform profiles shown in in a chirped PSW using 30 segments. (a) Design 1 (forward), (b) Design 1 (backward), (c) Design 2 (forward), (d) Design 2 (backward), (e) Design 3 (forward), and (f) Design 3 (backward), Dotted arrows show the position for phasematching at the extremes values of the grating. Two different waveguides are shown in each curve to show reproducibility. | 137 |
| 5.10 | Detuning curves for the spatial nonuniform profiles shown in in a chirped PSW using 60 segments with the calculated detuning curve (dashed line) using . The amplitude of the profile was multiplied by a factor of 40.2. (a) Design 1 (forward) and (b) Design 2 (forward). Dotted arrows show the position for phasematching at the extremes values of the grating. | 139 |

CHAPTER 1

INTRODUCTION

A fool ... is a man who never tried an experiment in his life

Letter to Sophy Ruxton, 9 March 1792.

Erasmus Darwin

(English Physician; grandfather of Charles Darwin)

A Pope once said about Sir Issac Newton “*Nature and Nature’s laws lay hid in night. God Said, let Newton be, -and all was light.-*” A couple of a hundred years ago the understanding of the furthestmost details of light propagation were not even contemplated. Starting with Newton’s *Opticks* at the dawn of the eighteenth century and later in 1864 a unified theory of electromagnetic fields by J.C. Maxwell established the foundations for the interaction of light with matter. The invention of the laser in 1960 made available intense, directional, coherent light beams, opened up new perspectives and introduced two new fields into the study of the interaction of light with matter: optical telecommunications and nonlinear optics.

The need for communication is inherent among humans. Optical signals have been used for telecommunications for hundreds of years by simple signal transmission through air.

Limiting processes such as absorbance and scattering in air limits this communication method. The use of an electrical signal for transmitting information between a transmitter and a receiver introduced new conveniences into everyday life since the middle of the nineteenth century. Research and development into new ways to improve communication capabilities has continued since then. It is a lit candle stretching the communion between science and technology.

In the 1980's the development of the diode laser combined with low loss optical fibers led to optical telecommunication over long distances. A mayor impetus for this type of communication was the discovery of erbium doped fiber amplifiers (EDFAs). These components are the pavement of the "information superhighway" currently in vogue by mundane citizens due to the massive demand of information through the Internet. The advantage of using optical signals over electrical signals is the huge bandwidth available with the THz carrier frequency of the carrier signal. Optical components of today's optical telecommunications are limited to light emitters, guiding conduits, amplifiers and receivers, and other components are required to perform switching, routing and modulation. Typically the information is processed electronically by converting the optical signal into an electronic signal, manipulating it and then reconvertng the signal to an optical signal for further transmission. Unfortunately such processing is inherent slow. The information cannot be realized by electrical signal processing and maintain the 10-100's Gb/s rates potentially available. Parasite capacitances limit the processing to the GHz regime.

The only way to exploit the huge available capabilities of optical communication is by means of photonics. Photonic signal processing in which optical signals are controlled directly

with another optical signal or electric signal is still in the early stages of development. Even with all the improvement to date, the reality is that all-optical switching devices have not yet reached the point where they have become practical. All-optical devices are functionally similar to electronic transistors. That is, these devices use light to switch light, or more specifically, the amplitude of one optical signal determines the output of either itself or a second signal. The basic principle on which an all-optical switch device operates is the generation of a phase shift that depends on intensity. The intensity-dependent phase shift can be obtained from a variety of nonlinear optical processes. Much research is currently being done to understand and exploit fully these phenomena, as evidenced by this dissertation. As just mentioned, the field of nonlinear optics was a direct result of the invention of the laser which allowed the creation of extremely intense optical fields that are comparable in magnitude to those found in intra-atomic charge interactions. When such an intense optical field interacts with matter, the response of the medium is no longer “linear” (i.e., proportional to the incident electric field), but is in fact proportional to the second, third and higher order powers of the electric fields. Most of the fundamental ideas involved in nonlinear optics were conceived and explained in the seminal paper by Armstrong *et al* [1]. Until a few years ago, with just a few exceptions, the sharp division established in nonlinear optics between second and third order nonlinearities produced two almost independent fields. The efforts to control light with light, known as all-optical processing [2] and the study of optical solitons [3], both milestones in nonlinear optics, used exclusively third order processes while second order processes mainly concentrated on the mixing or generation of new frequencies.

Nonlinear optical processes require high intensity light beams to make their effects observable and useful. As we will see, the efficiency of processes like second harmonic generation (SHG) typically increases with the interaction length and with the intensity of the optical fields involved. In bulk materials the intensity is increased by focusing a laser beam into them. However, the tighter the beam is focused, the faster it diverges due to diffraction, thus limiting the interaction length. This situation is greatly simplified by using optical waveguides. The ability of waveguides to maintain high intensities over relatively long lengths has made them ideal structures for the study of nonlinear optics. Traditionally, all-optical devices have relied on the Kerr nonlinear refractive index of a waveguide, which is a third order nonlinear effect. The nonlinear directional coupled (NLDC) [4] is the classic example of an all-optical switch based on the nonlinear refractive index.

Although known in principle from the early days of nonlinear optics, it is only in this decade that the concept that nonlinear phase shifts can also be derived from second order processes has been exploited in well developed crystalline materials, such as LiNbO_3 , KTP or LiTaO_3 . The promise of reasonably low driving powers led to a recent resurgence of interest in second order processes [5] and to the realization that our understanding of second order nonlinear phenomena is incomplete and allows the possible conception of completely new phenomena. One process with which we can achieve a large nonlinear phase shift using second order nonlinearities is second harmonic generation. For the non-phase-matched case, it evolves from successive up- and down-conversion processes. This phenomenon has been designated as “cascading”. Because the SHG conversion efficiency depends on the input intensity and the net phase shift of the fundamental depends on the intensity of the second

harmonic, the resulting phase shift is also nonlinear. In this sense this process generates an apparent change in refractive index, just as third order nonlinearities do. On the other hand cascading nonlinearities have their own distinctive characteristics which are fundamentally different from Kerr nonlinearities.

SHG technology has advanced sufficiently far so that factors other than conversion efficiency limit the utility of waveguide frequency conversion. For example, for a fundamental wavelength of 850 nm, the SHG acceptance-length products ($\Delta\lambda L$) are 0.6, 0.7 and 0.8 Åcm in bulk LiNbO₃, LiTaO₃ and KTP, respectively [6]. Useful conversion efficiencies require interaction lengths of ~1 cm, resulting in very narrow bandwidths that can put serious constraints on the SHG device fabrication tolerances on devices at laser diode wavelengths. Therefore new techniques for increasing the bandwidth acceptance of these devices have been proposed [7]. These new technologies allow tailoring of the phase matching distribution along the propagation.

1.1 Scope of Research

The goal of this dissertation is to present research which resulted in the identification of novel effects in waveguide second harmonic generation. This work started with an investigation of experimental and numerical inconsistencies that departed from the traditional scope of second harmonic generation, to be discussed in Chapter 2. In this chapter a general description of nonlinear optics will be formulated, with emphasis on standard second harmonic generation. A detail description of the characteristic lengths involved in SHG will be described. Phase-matching techniques such as quasi-phase matching and birefringent phase

matching will be revisited. Some of the inconsistencies that we are referring are caused by conditions usually overlooked when studying second harmonic generation. In Chapter 3 we study one of these, namely SHG in waveguides that support many modes. Examining second harmonic generation in detail under these conditions led to the identification of multimode competition in waveguide SHG. Numerical simulations and experimental results on QPM-LiNbO₃ waveguides that support many modes are presented.

In Chapter 4 a different type of inconsistency is explored, namely SHG field evolution in waveguides with spatially nonuniform and non-symmetrical distributions of parameters along the propagation path. Examining second harmonic generation in detail under these conditions led to the identification of SHG spatial nonreciprocity. The mathematical tools required to describe SHG in a spatially nonuniform distribution of parameters are revisited in detail. Numerical simulations and experimental results in QPM-LiNbO₃ waveguides with an explicit nonuniform-nonsymmetrical wavevector distribution are presented.

In Chapter 5 a more general study of spatially nonuniform distributions of parameters along the propagation path is presented. An elegant and simple result is observed in the low depletion regime. This result led to insights into the inverse problem in SHG. Numerical simulations and experimental measurements on controlled PSW-LiNbO₃ waveguides with an engineered nonuniform wavevector distribution are presented.

This dissertation is concluded in Chapter 6 with a summary of the results obtained in this research. In this chapter the basic results of this research will be summarized and conclusion will be drawn from these results.

CHAPTER 2

THEORY OF CASCADED SECOND ORDER NONLINEARITIES

“What is it you want to buy?” the Sheep said at last, looking up for a moment from her knitting.

“I don’t quite know yet,” Alice said very gently. “I should like to look around me first, if I might.”

“You may look in front of you, and on both sides, if you like,” said the Sheep; “but you can’t look all round you-unless you’ve got eyes at the back of your head.”

But these, as it happened, Alice had not got: so she contented herself with turning around, looking at the shelves as she came to them.

Through the looking Glass
Lewis Carroll

Not long after the invention of the laser the first optical nonlinear process was reported [8]. Franken *et al* observed that when an intense ruby laser beam was focused into a quartz crystal, ultraviolet light was created, which was the second harmonic of the incident laser frequency. This was the beginning of an entirely new field based on the study of the interaction of intense light with matter. This is a divergence from day-to-day experience involving weak optical fields where the response is proportional to the incident electric field, hence the term “linear optics.” Examples of linear optics are the refraction of light through

glass, reflection of light from specular and diffuse surfaces, and perception of a color through selective absorption. Most of the fundamental ideas involved in nonlinear optics were conceived in the seminal paper by Armstrong *et al.* [1] It is astonishing to realize that all contemporary nonlinear optics involves at least one of the ideas introduced in this work.

Until a few years ago, except for a few cases, the sharp division established by Armstrong *et al* between second and third order nonlinearities produced two almost independent fields. The efforts to control light with light known as all-optical processing [2] and the study of optical solitons [3], both milestones in nonlinear optics, used exclusively third order processes while second order processes mainly concentrated on the mixing or generation of frequencies.

Although it has been known since the early days of nonlinear optics that cascaded nonlinearities can produce a nonlinear phase shift [1,9] (and more recently by Karamzin and Sukhorukov [10,11]), it was not until after the observation by De Salvo *et al* [5] of such phase changes a few years ago that the idea was revisited. Since then the thin line between second and third order nonlinearities has started to disappear. To date, multiple π phase shifts in waveguides [12], all-optical switching devices [13], transistor action [14], solitons in one [15] and two dimensions [16], etc. have all been reported based on second rather than third order nonlinearities.

The theory of cascaded second order nonlinearities comes directly out of the theory of second order nonlinear processes, of which Second Harmonic Generation (SHG) is the best known example. As mentioned previously, emphasis has historically been on creating efficient SHG, which requires wave-vector matching of the fundamental to the second harmonic (SH).

Away from phasematching there are successive up-conversion and down-conversion processes that generate a nonlinear phase shift onto the fundamental, thus producing an apparent change in refractive index reminiscent of third order nonlinearities. Hence the term “cascading”.

As pointed out by Issac Asimov *the most exciting phrase to hear in science, the one that heralds new discoveries, is not “Eureka!” (I found it) but “That’s funny . . .”* SHG is not an exception to the rule. Having found some inconsistencies between theory and experiments is not unusual. The reason is always attributed to “an experimental error” and no further investigation is done. Nevertheless, some of these inconsistencies are the manifestation of fundamental factors missed in the theory. Assuming that every single discrepancy leads to a new theory, or that the existing theory is wrong may be presumptuous. The key point is to identify the truly relevant and consistent differences. In this dissertation some of these discrepancies in SHG and waveguide SHG are identified and incorporated into the theory. In the rest of this chapter the basic theory of SHG will be presented, with emphasis on waveguide SHG. To distinguish the different “relevant” effects highlighted in this dissertation, characteristic lengths are introduced, explained and discussed.

2.1 Review of Nonlinear Optics

Nonlinear optics is a branch of the study of interaction of light with matter. When light passes through matter, it interacts with individual atoms or molecules of the material and induces dipole moments. The average of these dipole moments is called the polarization. This polarization acts as a source and can generate an optical field. The response of the material

depends on the strength of the incident optical field, ranging from a linear response to catastrophic damage. When the input intensity is small, the response of the induced dipoles is linear to the applied optical field. In other words the fields radiated by the dipoles have the same frequency as the input beam and the end result is a delay of the optical field or a transfer of the incident electromagnetic energy to another type of energy. This gives rise to the linear refractive index and linear absorption. On the other hand, if the intensity of the incident beam is large and starts to be comparable to the electric fields binding the electrons to the nucleus, the response of the dipole is no longer linear and begins to oscillate anharmonically. Now the dipoles can generate an optical field at a different frequency than that of the incident field, induce a delay of the optical field dependent on the amount of light or change the absorptive characteristics of the matter, among other effects. Ultimately, if the incident field is strong enough it can even disassociate the electron from the nucleus and create catastrophic damage.

Our understanding of the interaction of light with matter as we know it is mathematically represented by Maxwell's equations. For a source free dielectric material, Maxwell's equations can be cast into the wave equation:

$$\nabla^2 \vec{E}(\vec{r}, t) - \frac{1}{c^2} \frac{\partial^2 \vec{E}(\vec{r}, t)}{\partial t^2} = \mu_0 \frac{\partial^2 \vec{P}(\vec{r}, t)}{\partial t^2} \quad (2.1)$$

where the vector \mathbf{P} is the polarization of the medium, n_0 is the linear refractive index, c is the speed of light in vacuum, μ_0 is the permittivity of free space, and $\nabla^2 = \partial^2/\partial x^2 + \partial^2/\partial y^2 + \partial^2/\partial z^2$ is the three dimensional Laplacian. To solve this equation, a relationship between \mathbf{P} and \mathbf{E} must be written. Formally this relationship must come from a quantum mechanical analysis

of the dipoles in the medium. Fortunately for optical frequencies far from material resonances and for media with response times faster than the probe-pulse duration, the so called instantaneous response, the driving term of the polarization can be described by a phenomenological relationship written as a Taylor series in the powers of the electric field based on an electron on a spring model of the atom [17]:

$$\vec{P}(t) = \epsilon_0 \left[\int_{-\infty}^{\infty} \vec{\chi}^{(1)}(t-t') \cdot \vec{E}(t') dt' + \int_{-\infty}^{\infty} \int_{-\infty}^{\infty} \vec{\chi}^{(2)}(t-t', t-t'') : \vec{E}(t') \vec{E}(t'') dt' dt'' + \int_{-\infty}^{\infty} \int_{-\infty}^{\infty} \int_{-\infty}^{\infty} \vec{\chi}^{(3)}(t-t', t-t'', t-t''') : \vec{E}(t') \vec{E}(t'') \vec{E}(t''') dt' dt'' dt''' + \dots \right] \quad (2.2)$$

where ϵ_0 is the permittivity of vacuum and $\chi^{(n)}$ are the n-th order susceptibilities tensors. The dot operators are dyad products of the tensors and field vectors. Usually these susceptibilities are tensors whose rank increases as the order of the nonlinear expansion increases, resulting in a complex material response. In this subject Nature is kind and material symmetries often reduce the number of independent elements, and many are zero. Further assumptions such as the slow-varying envelope approximation (SVEA) and the use of quasi-monochromatic traveling waves allows the problem to be manageable. We will use these assumptions shortly, but first we need to have a closer look at the different terms in equation (2.2). There is an extensive bibliography describing each term involved [17, 18, 19]. Only those aspects pertinent to this dissertation are discussed here.

The first term in equation (2.2) ($\propto \chi^{(1)}$) represents the linear response of the matter and leads to linear optics. From this term the linear refractive index (n_0) and absorption coefficient

(α_o) are obtained. Most everyday optics needs only this term to explain the behavior of basic effects [20]. In particular the linear refractive index far from absorption is related to $\chi^{(1)}$ by:

$$n_o^2 = 1 + \Re e[\chi^{(1)}] \quad (2.3)$$

This term is relevant in linear optics because it introduces the notion of linear phase delay of the electrical field, also known as the optical path difference. In the scope of this dissertation the phase of the electrical field plays a key role. The linear phase accumulated by the electrical field after propagating a distance L in a dense medium is

$$\Delta\phi_{linear} = \frac{2\pi}{\lambda} n_o L \quad (2.4)$$

where λ is the wavelength of the optical field.

The second term in the expansion, $\propto \chi^{(2)}$, describes second-order nonlinear optics. It often describes wave-mixing processes. Examples of second-order effects are second harmonic generation (SHG), sum and difference frequency generation (SFG and DSG) among others [21,22]. SHG will be discussed in detail in the next section.

The third term in the expansion, $\chi^{(3)}$, leads to some of the better known nonlinear optical effects such as third harmonic generation, self and cross phase modulation, two photon absorption, four wave mixing and the optical Kerr effect [3]. Among them the optical Kerr effect requires special consideration because it is responsible for the most commonly studied nonlinear phase shift. It is convenient to assume through this treatment that the fields are quasi-monochromatic traveling plane waves of the form

$$\vec{E}(\vec{r},t) = \frac{1}{2} \vec{E}_o(\vec{r},t) e^{i(\vec{k}\cdot\vec{r}-\omega t)} + c.c. \quad (2.5)$$

where \mathbf{k} is the propagation vector ($|\mathbf{k}| = 2\pi n_o/\lambda$) and $E_o(\mathbf{r},t)$ represents the slowly-varying envelope of the electric field. In other words, the field amplitude changes slowly relative to the fast optical carrier frequency. Using this assumption, we can analyze the problem in the spectral instead of the temporal domain. To derive the spectral response of the material, the Fourier transforms of both the electric field and the susceptibility are required, as well as the definition of the Dirac delta distribution $\delta(\omega)$. These are given by

$$\begin{aligned} E(\omega) &= \int_{-\infty}^{\infty} E(t) e^{-i\omega t} dt \\ E(t) &= \frac{1}{2\pi} \int_{-\infty}^{\infty} E(\omega) e^{i\omega t} d\omega \\ \chi_{ijk}^{(2)}(\omega_1, \omega_2) &= \int_{-\infty}^{\infty} \int_{-\infty}^{\infty} \chi_{ijk}^{(2)}(t_1, t_2) e^{-i(\omega_1 t_1 + \omega_2 t_2)} dt_1 dt_2 \\ \delta(\omega - \omega_o) &= \frac{1}{2\pi} \int_{-\infty}^{\infty} e^{-i(\omega - \omega_o)t} dt \end{aligned} \quad (2.6)$$

Assuming additionally that the material has an instantaneous response so only the components of E exist at $\{\omega, -\omega\}$ the polarization (2.2) can be written as

$$\begin{aligned} \vec{P}(\omega) = \epsilon_o \left[\vec{\chi}^{(1)}(\omega) \cdot \vec{E}(\omega) + \vec{\chi}^{(2)}(\omega; \omega_1, \omega_2) : \vec{E}(\omega_1) \vec{E}(\omega_2) \right. \\ \left. + \vec{\chi}^{(3)}(\omega; \omega_1, \omega_2, \omega_3) : \vec{E}(\omega_1) \vec{E}(\omega_2) \vec{E}(\omega_3) + \dots \right] \end{aligned} \quad (2.7)$$

The term in the polarization that leads to the third order nonlinear refractive index is

$$P_i(\omega) = \epsilon_o D \chi_{ijkl}^{(3)}(\omega: -\omega, -\omega, \omega) E_j(\omega) E_k(\omega) E_l^*(\omega) \quad (2.8)$$

where the i,j,k,l indices refer to the polarization components of the field. Einstein's notation is used to represent summation over repeated indices, leading to the degeneracy factor D . Considering the same frequency ω and assuming polarization along the x-axis for all three fields, the magnitude of the polarization term becomes [18]

$$P_{NL} = \frac{3}{4} \epsilon_o \chi_{xxxx}^{(3)} E_x E_x^* E_x \quad (2.9)$$

Including the linear polarization, the total polarization becomes

$$P = \epsilon_o \left(\chi^{(1)} + \frac{3}{4} \chi_{xxxx}^{(3)} |E_x|^2 \right) E_x \quad (2.10)$$

By analogy with the linear refractive index, an intensity dependent refractive index can be obtained. Assuming $\chi_{xxxx}^{(3)}$ real and considering that the nonlinear contribution to the refractive index is typically small, we can calculate the total refractive index:

$$\begin{aligned}
n &= \sqrt{n_o^2 + \frac{3}{4} \chi_{xxxx}^{(3)} |E|^2} \approx n_o \left[1 + \frac{3}{8} \frac{\chi_{xxxx}^{(3)}}{n_o^2} |E|^2 \right] \\
&= n_o + \frac{3}{4} \frac{\chi_{xxxx}^{(3)}}{n_o^2 \epsilon_o c} I \quad \equiv n_o + n_2 I
\end{aligned} \tag{2.11}$$

where I is the intensity in W/cm^2 ($I = \frac{1}{2} \epsilon_o c |E|^2$). Using a similar procedure, if we consider complex $\chi^{(3)}$, it can be shown that the real part leads to the nonlinear refractive index in (2.11) and the imaginary part to a two-photon absorption coefficient (α_2). Following a similar train of thought, it can be shown that higher odd order elements in the polarization (2.2) also contribute to the refractive index and to the absorption coefficient by multiphoton absorption

$$\begin{aligned}
n &= n_o + n_2 I + n_3 I^2 + \dots \\
\alpha &= \alpha_o + \alpha_2 I + \alpha_3 I^2 + \dots
\end{aligned} \tag{2.12}$$

where $\{n_2, n_3, \dots\}$ are the nonlinear contributions to the refractive index and $\{\alpha_2, \alpha_3, \dots\}$ are the $\{$ two, three, $\dots\}$ photon absorption associated with the $\{$ third, fifth, $\dots\}$ order nonlinear susceptibilities respectively. In general these quantities are small (n_2 for silica is only $3 \times 10^{-16} \text{ cm}^2/\text{W}$) and in practice higher order terms of the expansion (2.2) are seldom included due to the extremely high fields needed to make these terms significant.

To conclude the general review of nonlinear optics, it is noteworthy that the existence of this material nonlinear refractive index has allowed the development of traditional all-optical switches as discussed in chapter one based on nonlinear phase shifts imparted to the

field. In a similar way as the linear phase shift (2.4), we can calculate the nonlinear phase shift during propagation over length L due to the optical Kerr effect as

$$\Delta\phi_{NL} = \frac{2\pi}{\lambda} n_2 I L \quad (2.13)$$

or in general considering material properties as

$$\Delta\phi_{NL} = \frac{2\pi}{\lambda} (n_2 I + n_3 I^2 + \dots) L \quad (2.14)$$

This is a key point to highlight in the study of nonlinear optics. It is not the nonlinear refractive index, the interaction length or the intensity inside a material which is the cause of a particular effect. It is the combination of the three elements simultaneously which is responsible for the effect.

2.2 Second Harmonic Generation

The second term of the expansion (2.2) describes second-order nonlinear optics. The polarization induced by this term is usually much stronger than that induced by higher order nonlinearities. Therefore, the experimental observation of a second order effect such as second harmonic generation as the first modern manifestation of nonlinear optics was not strange. The endless demand for new wavelength sources and the large number of accessible effects, among other reasons, have ensured that second order processes are under continuous

study and new effects and ideas are still being considered. The second-order processes are driven by the second order term in the polarization expansion

$$P_i^{(2)}(\omega) = \epsilon_o \chi_{ijk}^{(2)}(\omega = \omega_1 + \omega_2; \omega_1, \omega_2) E_j(\omega_1) E_k(\omega_2) \quad (2.15)$$

It can be seen from symmetry arguments that this term is present only in materials which lack a center of symmetry, known as noncentrosymmetric materials. For centrosymmetric materials the $\chi_{ijk}^{(2)}$ -tensor is identically zero. In this dissertation, the focus will be on the second harmonic generation process although the discussion can be easily extended to other parametric processes. Therefore, we will be only interested in terms including either ω or 2ω . Furthermore, we will only consider the process in which two photons with the same polarization at frequency ω (fundamental) combine and generate one photon at frequency 2ω (second harmonic - SH). This process is known in the literature as type I phasematching. An additional discussion on phase-matching methods will be made later in the chapter.

In regions of low spectral dispersion the $\chi_{ijk}^{(2)}$ -tensor exhibits symmetry properties known as Kleinman symmetry. When this symmetry holds, it is customary to contract the last two indices in the $\chi_{ijk}^{(2)}$ -tensor known as the Voigt contraction of indices as follows:

$$\begin{array}{l} jk: \quad 11 \quad 22 \quad 33 \quad 23,32 \quad 31,13 \quad 12,21 \\ \Rightarrow j: \quad 1 \quad 2 \quad 3 \quad 4 \quad 5 \quad 6 \end{array}$$

$$\begin{pmatrix} 11 & 12 & 13 \\ 21 & 22 & 23 \\ 31 & 32 & 33 \end{pmatrix} \Rightarrow \begin{pmatrix} 1 & 6 & 5 \\ 6 & 2 & 4 \\ 5 & 4 & 3 \end{pmatrix} \quad (2.16)$$

In the literature the susceptibility tensor $\chi_{ij}^{(2)}$ is usually replaced by the tensor \mathbf{d}_{ij} , which is half of $\chi^{(2)}$. Therefore, the second-order nonlinear polarization (2.15) can be written as

$$\begin{bmatrix} P_x \\ P_y \\ P_z \end{bmatrix} = \epsilon_o \begin{bmatrix} d_{11} & d_{12} & d_{13} & d_{14} & d_{15} & d_{16} \\ d_{21} & d_{22} & d_{23} & d_{24} & d_{25} & d_{26} \\ d_{31} & d_{32} & d_{33} & d_{34} & d_{35} & d_{36} \end{bmatrix} \begin{bmatrix} E_x^2 \\ E_y^2 \\ E_z^2 \\ 2E_y E_z \\ 2E_x E_z \\ 2E_x E_y \end{bmatrix} \quad (2.17)$$

As mentioned earlier, crystal symmetry can further reduce the number of independent elements and causes many to be identically zero. For example crystals in the 3m point-group such as lithium niobate (LiNbO_3) have eight nonvanishing elements, only three of which are independent (d_{33} , $d_{16}=-d_{21}=d_{22}$, $d_{15}=d_{24}=d_{31}=d_{32}$) coefficients of the $\chi_{ijk}^{(2)}$ -tensor as can be found in any standard nonlinear optics text [18].

Once the desired propagation direction and polarization of the incident electric fields, which seldom coincide with the crystallographic axes have been selected, an effective d-element (d_{eff}) can be calculated for the nonlinear polarization. Once again, details can be found in the literature [23].

To investigate SHG further, a set of coupled nonlinear equations needs to be derived which describe the evolution of the fields involved [24]. The analysis starts by using the proper nonlinear polarization from (2.17) for type I SHG given by

$$\begin{aligned}
P_{NL} &= P^{(2)}(\omega) + P^{(2)}(2\omega) \\
P^{(2)}(\omega) &= \epsilon_o d_{eff}(\omega:2\omega, -\omega) E(2\omega) E(\omega)^* \\
P^{(2)}(2\omega) &= \epsilon_o d_{eff}(2\omega:\omega, \omega) E(\omega) E(\omega)
\end{aligned} \tag{2.18}$$

where $(^*)$ denotes complex conjugate. We then include them in (2.1) using the proper spatial and temporal considerations to obtain the evolution equations for the fundamental and SH fields. In this analysis we will allow the possibility that the waves do not propagate along the principal axes of the $\chi^{(2)}$ crystal, in which case the energy propagation directions are different from the phase propagation direction and different from each other. This is included by introducing the angles ρ_ω and $\rho_{2\omega}$ between the z-axis and the Poynting vectors of the fundamental and SH respectively. Without loss of generality, this deviation will be confined to the y-z plane. Temporal aspects of the propagation are included by frequency dispersion in the refractive index, so that the wavevector-frequency dependence is expressed in a Taylor series expansion to the second order as

$$k_\Omega(\Omega + \Delta\omega) = k_{\Omega,0} + k'_\Omega \Delta\omega + k''_\Omega \Delta\omega^2/2 \tag{2.19}$$

where $\Omega = \{\omega, 2\omega\}$, and

$$k'_\Omega = \left. \frac{\partial}{\partial \omega} k_\Omega(\omega) \right|_\Omega \quad \text{and} \quad k''_\Omega = \left. \frac{\partial^2}{\partial \omega^2} k_\Omega(\omega) \right|_\Omega \tag{2.20}$$

The group velocity is $v_\Omega = 1/k'_\Omega$ and the group velocity dispersion (GVD) coefficient is k''_Ω . Pulse spreading and any acquired frequency chirp are effects which are related to these

coefficients. The relation between the electric field and the linear displacement electric density current is now dependent on frequency. The Fourier transform pair

$$\begin{aligned}\vec{\mathcal{E}}_j(\vec{r}, \Delta\omega) &= e^{-i\{k_j(\omega_j + \Delta\omega) - k_{j,0}\}z} \int_{-\infty}^{\infty} \vec{E}_{j,o}(\vec{r}, t) e^{-i\Delta\omega t} dt \\ \vec{E}_j(\vec{r}, t) &= \frac{1}{2\pi} \int_{-\infty}^{\infty} \vec{\mathcal{E}}_j(\vec{r}, \Delta\omega) e^{i\{k_j(\omega_j + \Delta\omega) - k_{j,0}\}z + i\Delta\omega t} d\Delta\omega\end{aligned}\tag{2.21}$$

is used to express this dependence. Decomposing the electric field, we assume that the fundamental and second-harmonic fields have the forms

$$\begin{aligned}\vec{E}_\omega(\vec{r}, t) &= \vec{E}_{o,\omega}(x, y - \rho_\omega z, z, t) e^{i(k_{\omega,z} z + k_{\omega,y} y - \omega t)} \\ \vec{E}_{2\omega}(\vec{r}, t) &= \vec{E}_{o,2\omega}(x, y - \rho_{2\omega} z, z, t) e^{i(k_{2\omega,z} z + k_{2\omega,y} y - 2\omega t)}\end{aligned}\tag{2.22}$$

where the wavenumber dispersion (2.19) is associated with the magnitude of the wavevector $|\mathbf{k}_\Omega|$. Including these relations in the wave equation (2.1), transforming the nonlinear polarization into its spectral representation using (2.21) and following the SVEA given by

$$\begin{aligned}\left| k_{\Omega,o}^2 E_\Omega \right| &\gg \left| k_{\Omega,o} \frac{\partial E_\Omega}{\partial z} \right| \gg \left| \frac{\partial^2 E_\Omega}{\partial z^2} \right| \\ \left| \Omega^2 E_\Omega \right| &\gg \left| \Omega \frac{\partial E_\Omega}{\partial t} \right| \gg \left| \frac{\partial^2 E_\Omega}{\partial t^2} \right| \\ \left| \Omega^2 P_\Omega^{NL} \right| &\gg \left| \Omega \frac{\partial P_\Omega^{NL}}{\partial t} \right| \gg \left| \frac{\partial^2 P_\Omega^{NL}}{\partial t^2} \right|\end{aligned}\tag{2.23}$$

where $\Omega = \{\omega, 2\omega\}$, we obtain the complete evolution of the field envelopes. We exclude here intermediate algebraical steps to obtain the final form of the coupled mode equations because they do not contribute any insight into the problem, except for one intermediate step which does have physical meaning in the SHG problem: the definition of the wavevector-mismatch (Δk_o)

$$\Delta k_o = 2k_{\omega,0} - k_{2\omega,0} = \frac{4\pi}{\lambda}(n_{\omega} - n_{2\omega}) \quad (2.24)$$

This term was introduced to simplify the exponential terms on both sides of the equations, but overall it has a more fundamental physical meaning. As we will see in the next section, this quantity governs the evolution of the fields along the propagation direction as a function of the difference in phase velocity between the fundamental and the second harmonic. Later in the chapter different phasematching techniques will be discussed and, as will be evident in chapters 4 and 5, the wavevector mismatch controls some generalized SHG effects such as nonreciprocity and nonuniform propagation.

This quantity is also responsible for much confusion in the field of SHG. Depending on the definition of the wavevector mismatch and the definition of the field envelopes (2.22), the coupled mode equations appear in the literature with all possible permutations of i , $-i$, Δk_o or $-\Delta k_o$. Care has to be taken to be consistent with the definitions (2.22) and (2.24). With the convention used here, we obtain for propagation in the $+z$ direction a negative cascaded nonlinearity for $\Delta k_o < 0$ and vice versa.

Including a linear loss term phenomenologically or through inclusion of conductivity in Maxwell's equations, the field envelope, coupled mode equations for type-I SHG are given by

$$\begin{aligned} \frac{\partial E_{\omega}}{\partial z} - \frac{1}{2}(k'_{\omega} - k'_{2\omega}) \frac{\partial E_{\omega}}{\partial t} + ik''_{\omega} \frac{\partial^2 E_{\omega}}{\partial t^2} \\ + \frac{i}{2k_{\omega}} \left\{ \frac{\partial^2 E_{\omega}}{\partial x^2} + \frac{\partial^2 E_{\omega}}{\partial y^2} \right\} + \rho_{\omega} \frac{\partial E_{\omega}}{\partial y} = -i \frac{\omega d_{eff}}{n_{\omega} c} E_{2\omega} E_{\omega}^* e^{i\Delta k_o z} - \frac{\alpha_{\omega}}{2} z \end{aligned} \quad (2.25)$$

$$\begin{aligned} \frac{\partial E_{2\omega}}{\partial z} - \frac{1}{2}(k'_{2\omega} - k'_{\omega}) \frac{\partial E_{2\omega}}{\partial t} + ik''_{2\omega} \frac{\partial^2 E_{2\omega}}{\partial t^2} \\ + \frac{i}{2k_{2\omega}} \left\{ \frac{\partial^2 E_{2\omega}}{\partial x^2} + \frac{\partial^2 E_{2\omega}}{\partial y^2} \right\} + \rho_{2\omega} \frac{\partial E_{2\omega}}{\partial y} = -i \frac{\omega d_{eff}}{n_{2\omega} c} E_{\omega} E_{\omega} e^{-i\Delta k_o z} - \frac{\alpha_{2\omega}}{2} z \end{aligned} \quad (2.26)$$

These equations describe all the physics of SHG propagation as long as the SVEA is valid. In section 2.4 each of these terms will be independently analyzed, highlighting the associated characteristic length and the related novel effects.

2.3 Physics of Cascading

The process of cascaded second-order nonlinearities is rooted in the SHG process. Cascading is not an independent concept but just another manifestation of SHG. We start with the coupled mode equations (2.25) and (2.26) which describe the spatial and temporal evolution of the fundamental and SH fields. These fields are, in general, complex quantities. Therefore, they have an associated amplitude and phase. Traditionally SHG deals with the generation of the second harmonic intensity, i.e., the second harmonic amplitude generated from an input fundamental and the phase is usually neglected.

We can examine conceptually the evolution of the phases that lead to the process of cascaded nonlinearities. Focusing on the nonlinear term of equations (2.25) and (2.26) we observe that the SH is generated by mixing two fundamental photons, while the fundamental is recovered by combining one fundamental photon and a harmonic photon. In the non-zero wavevector mismatch case ($\Delta k_o \neq 0$) there is a periodic exchange of energy with distance between the fundamental and the second harmonic. Because of the wavevector mismatch, both fields travel at different phase velocities. Thus the regenerated fundamental wave has a different phase from the fundamental that was not converted to SHG. These two coherent fields interfere and influence the evolution of the overall fundamental wave, altering the phase of the fundamental wave, or in other words, imposing a phase-shift onto the fundamental. This is schematically represented for the fundamental wave in Figure 2.1. A similar description is applicable to the harmonic field.

The generation of phase shifts relies on successive up-conversion and down-conversion processes, both of which are second-order, $\chi^{(2)}$, nonlinear processes. Therefore

the name “ $\chi^{(2)}:\chi^{(2)}$ cascaded process” or simply “*cascading process*” comes from the consecutive $\chi^{(2)}$ processes involved in the creation of the phase-shift imposed onto the fundamental wave.

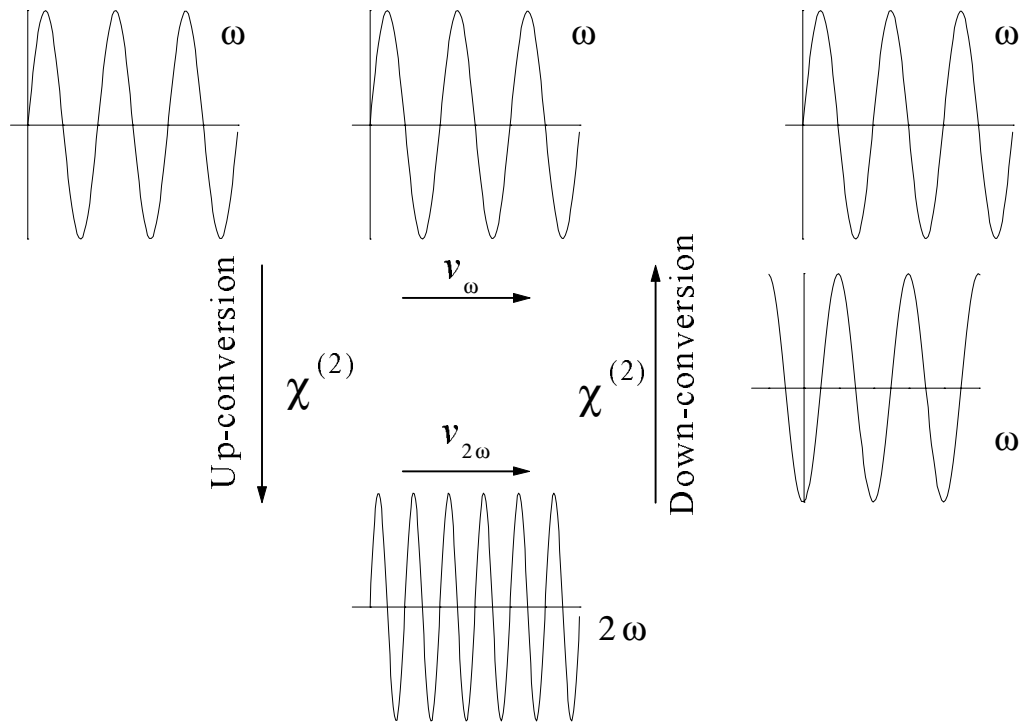


Figure 2.1 Schematic representation of the physical origin of the nonlinear phase shift on the fundamental wave due to cascading. v_1 and v_2 are the phase velocities of the fundamental and SH respectively.

Because the net phase shift of the fundamental depends on the intensity of the second harmonic and hence on the fundamental input intensity, the resulting phase shift is also nonlinear. Because SHG is a coherent process, the relative phase between the fundamental and harmonic plays a key role.

The SHG generated from a small element along the propagation path depends on the local wavevector mismatch, the amplitude and phase of the fundamental beam transmitted to that point and the SHG amplitude and phase generated up to that point. In SHG, and in particular for the cascaded nonlinearity which generates the nonlinear phase shift, the fundamental and second harmonic fields require some joint propagation to occur (i.e., a "non-local" process).

Before attempting a general description of SHG from the complete coupled mode equations (2.25) and (2.26), an understanding of the basic ideas behind them is required. To appreciate the fundamental concepts involved, we can simplify the problem for clarity. Assume that a continuous plane wave in a lossless media causes the time derivatives, transverse coordinate derivatives and loss coefficients in (2.25) and (2.26) to vanish. With these assumptions, the coupled mode equations are reduced to the standard CW coupled mode equations found in the literature for type I SHG

$$\begin{aligned}\frac{dE_{\omega}}{dz} &= -i \frac{\omega d_{eff}}{n_{\omega} c} E_{2\omega} E_{\omega}^* e^{i\Delta k_o z} \\ \frac{dE_{2\omega}}{dz} &= -i \frac{\omega d_{eff}}{n_{2\omega} c} E_{\omega} E_{\omega} e^{-i\Delta k_o z}\end{aligned}\tag{2.27}$$

All the basic phenomenological aspects of second harmonic generation are included in these equations. Their solution has been known since the early stages of nonlinear optics in terms of Jacobi elliptical integrals [1]. The result for the non-seeded (zero initial harmonic field) condition is [25]

$$I_{2\omega}(z) = I_{\omega}(0) B_b \operatorname{sn}^2 \left(\frac{\Gamma z}{B_b} \middle| B_b^4 \right) \quad I_{\omega}(z) = I_{\omega}(0) - I_{2\omega}(z)$$

$$\frac{1}{B_b} = \frac{\Delta k_o}{4\Gamma} + \sqrt{1 + \left(\frac{\Delta k_o}{4\Gamma} \right)^2} \quad (2.28)$$

$$\Gamma = \frac{\omega d_{eff}}{n_{\omega} c} |E_{\omega}(0)|^2$$

where sn is a Jacobian elliptic function. Due to the mathematical complexity of this solution, extracting the physical meaning is not easy. Only one result from the exact analysis has a direct repercussion on the content of this dissertation. For the phasematched condition ($\Delta k_o = 0$) the solution reduces to the well-known result

$$\begin{aligned} I_{2\omega}(L) &= I_{\omega}(0) \tanh^2(\Gamma L) \\ I_{\omega}(L) &= I_{\omega}(0) \operatorname{sech}^2(\Gamma L) \end{aligned} \quad (2.29)$$

When the depletion of the fundamental wave is small, we have $\Delta k_o / \Gamma \gg 1$ except near $\Delta k_o = 0$.

In this region, $B_b \approx \Gamma / \Delta k_o \approx 0$. Using $\operatorname{sn}(u|0) = \sin(u)$, (2.29) becomes

$$I_{2\omega}(L) = I_{\omega}^2(0) (\Gamma L)^2 \operatorname{sinc}^2(\Delta k L / 2) \quad (2.30)$$

The relation between (2.29) and (2.30) has a fundamental meaning in SHG theory. These equations show that the SH intensity does not grow quadratically with input intensity and

length except in the low depletion regime and that the conversion saturates as the fundamental is depleted. This subject will be analyzed in section 2.3.

Following Stegeman *et al* [2], to simplify the numerical analysis (2.27) is rewritten using field amplitudes $A_{\omega,2\omega}$ such that $|A_{\omega,2\omega}|^2$ is the intensity of each field.

$$A_{\omega}(z) = E_{\omega}(z) \left(\frac{2I_o}{n_{\omega} c \epsilon_o} \right)^{-\frac{1}{2}} \quad A_{2\omega}(z) = E_{2\omega}(z) \left(\frac{2I_o}{n_{2\omega} c \epsilon_o} \right)^{-\frac{1}{2}} \quad (2.31)$$

where I_o is the total intensity inside the material defined as,

$$I_o = \frac{1}{2} n_{\omega} c \epsilon_o |E_{\omega}(0)|^2 + \frac{1}{2} n_{2\omega} c \epsilon_o |E_{2\omega}(0)|^2 \quad (2.32)$$

This allows the use of a single nonlinear coupling constant for both equations given by

$$\kappa = \frac{2\omega d_{eff}}{\sqrt{2n_{\omega}^2 n_{2\omega} \epsilon_o c^2}} \quad (2.33)$$

and (2.27) can be rewritten as

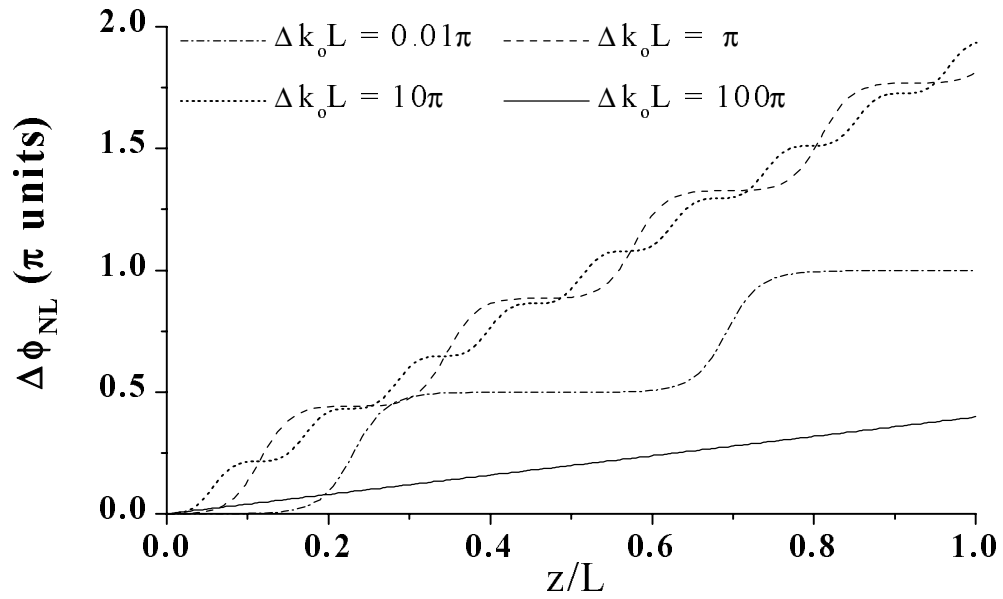
$$\begin{aligned} \frac{dA_{\omega}}{dz} &= -i\kappa A_{2\omega} A_{\omega}^* e^{i\Delta k_o z} \\ \frac{dA_{2\omega}}{dz} &= -i\kappa A_{\omega}^2 e^{-i\Delta k_o z} \end{aligned} \quad (2.34)$$

Under these definitions, κ has units of $[W^{-1/2}]$ and $A_{\omega,2\omega}$ units of $[W^{1/2} m^{-1}]$ such that $\kappa A_{\omega,2\omega} L$ is a dimensionless quantity, where L is the propagation length (units of $[m]$). The

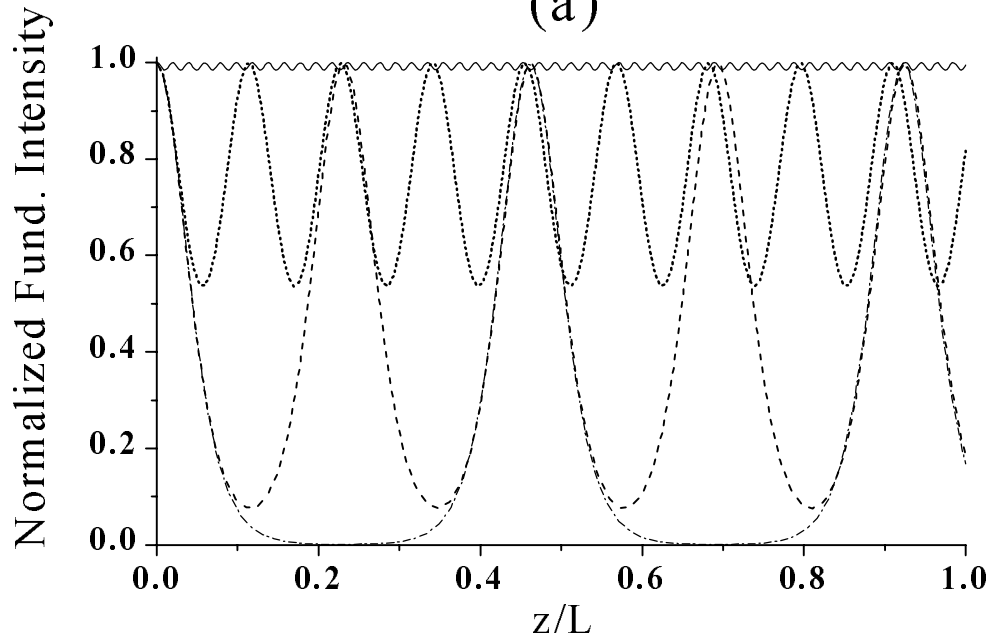
selection of these normalized variables allows the use of reasonable quantities for numerical calculations. As an example, for a 1 cm length of LiNbO₃ with $d_{\text{eff}} = 31.8$ pm/V, a typical intensity of 3.71 MW/cm² corresponds to $\kappa|A_{\omega}(0)|L=4$ at 1.55 μm . As will be shown later, the product $\kappa A_{\omega,2\omega}L$ plays a crucial role in SHG.

These equations were solved with a fourth-order Runge-Kutta routine implemented in the Matlab programming library. The output of these calculations gives a set of complex field amplitudes for both the fundamental and the SH. These quantities are then as the amplitude and phase of both the fundamental and the SH. Examples of the results obtained for nonseeded propagation ($|A_{2\omega}(0)|=0$) as a function of the normalized propagation distance (z/L) for a given wavevector mismatch (Δk_0L) is shown in Figure 2.2.

Some key characteristics of cascaded nonlinearities are evident in this figure. The nonlinear phase shift imposed onto the fundamental grows in a step-like fashion, as seen in Figure 2.2(a). The position of the jump corresponds to the down-conversion from the SH to the fundamental depicted in Figure 2.2(b), and has a maximum value close to $\pi/2$ near phasematching. The step size and period decrease as the detuning becomes larger, corresponding to lower conversion to the second harmonic. Although this is an oversimplified picture of the problem, in general SHG behaves this way. There is a strong exchange of energy near phasematching manifested as a large depletion of the fundamental, and at the same time the size of the phase jumps is large. It becomes progressively weaker as the phase mismatch increases with a smaller period.



(a)



(b)

Figure 2.2 (a) Nonlinear phase shift $\Delta\phi_{\text{NL}}$ and (b) normalized fundamental intensity as a function of the normalized propagation z/L for various wavevector detunings. In both cases $\kappa A_\omega(0)L = 20$.

Another feature to highlight from Figure 2.2 is that the amount of nonlinear phase shift depends on the phase mismatch. It grows from zero phase mismatch to a maximum value for a phase mismatch between π and 10π and then becomes progressively smaller. This shows the existence of an optimum detuning in which the nonlinear phase shift is maximum. Also from these calculations the nonlinear nature of the phase shift that is imposed onto the fundamental is evident. In Figure 2.3, results obtained for nonseeded propagation ($|A_{2\omega}(0)|=0$) as a function of the input fundamental intensity ($|A_{\omega}(0)|$) at fixed length and nonlinear strength for different wavevector mismatches are shown. The growth in the phase shift also exhibits a step-wise behavior (Figure 2.3(a)) corresponding to a down conversion process (Figure 2.3(b)). It exhibits again the existence of an optimum phase mismatch in which the phase shift is maximum.

One characteristic dominates this figure. The amount of nonlinear phase shift seems to saturate at high intensities. This is evident as a decrease in the average slope on the curves in Figure 2.3(a). This characteristic corresponds in Figure 2.3(b) to a decrease in the period of energy exchange between successive down conversion processes as the intensity is incremented. While the increase in phase shift with intensity is a fundamental signature of cascading, the increase in energy exchange is a consequence of the phase shift which detunes the system further from phasematching. This will be clarified by next studying the collective behavior.

A behavior common to Figure 2.2 and Figure 2.3 is that, at large detunings, the growth in phase shift is linear with distance and intensity. This is a characteristic of Kerr type nonlinearities as mentioned earlier in (2.13). This will be discussed in the next subsection.

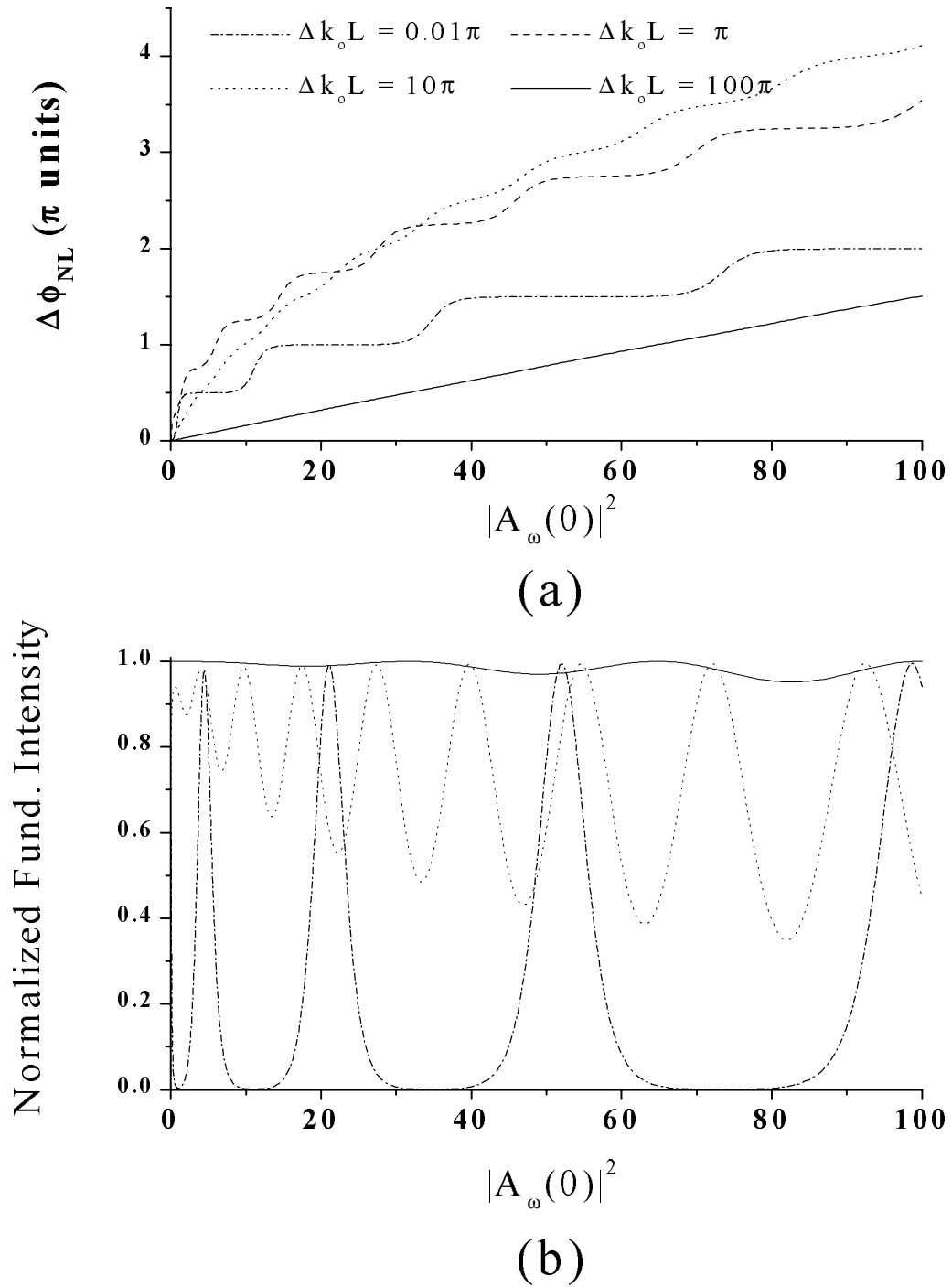
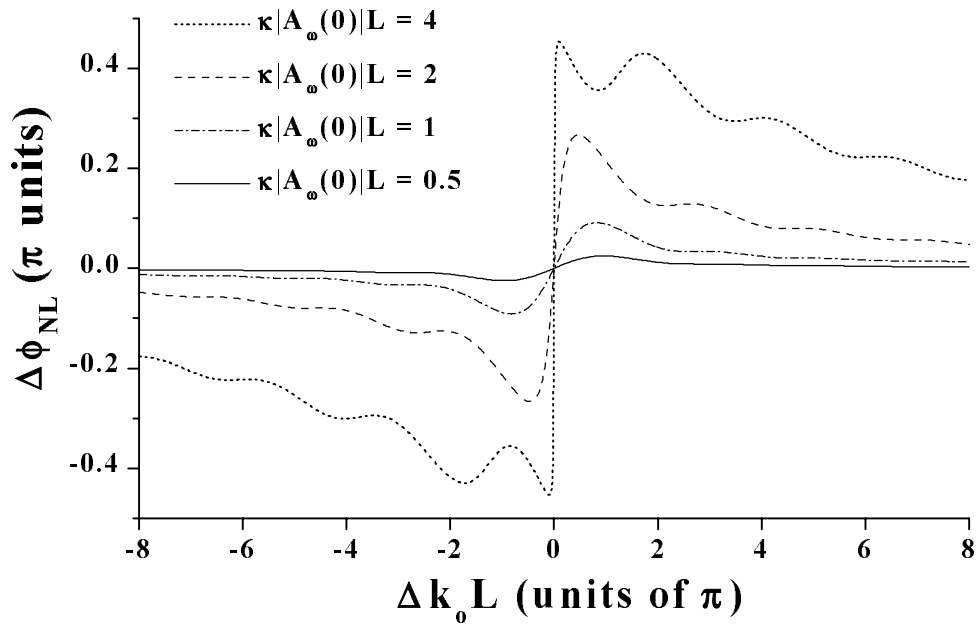


Figure 2.3 Intensity dependence of (a) nonlinear phase shift $\Delta\phi_{\text{NL}}$ and (b) normalized fundamental intensity as a function of the input fundamental intensity $|A_{\omega}(0)|^2$ for different wavevector detunings. In each cases $\kappa L = 4$.

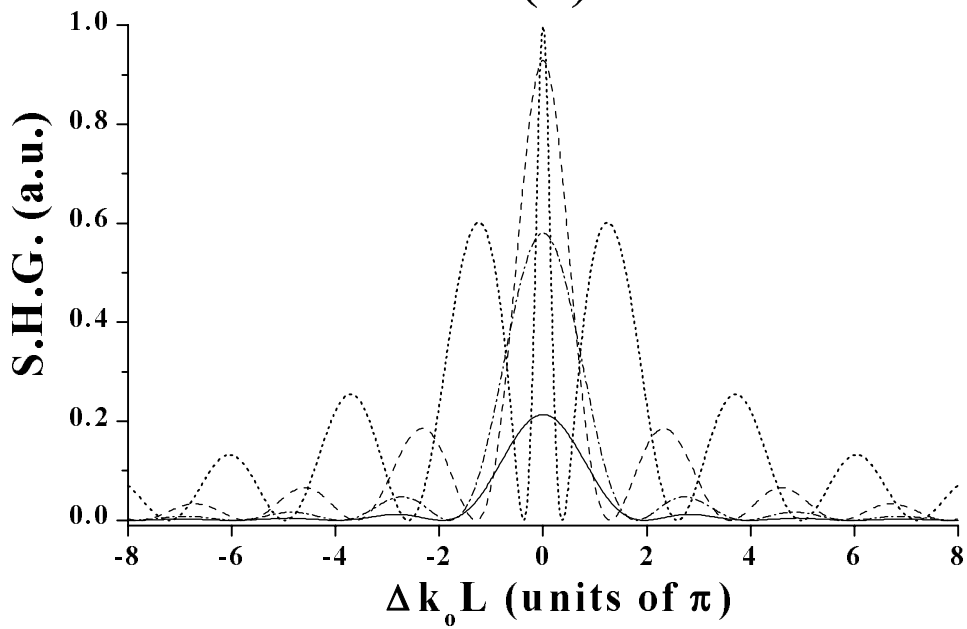
Understanding the origin of cascading as a nonlinear phase shift imposed onto the fundamental is essential. However, if we want to describe and use the concepts involved in cascading it is not enough. To have a complete picture we need to study the collective behavior of the system described by the dispersion implied in Figure 2.2 and Figure 2.3. This is normally referred to as the SHG detuning curve. Examples of this collective dispersion for the nonseeded case are shown in Figure 2.4. Nevertheless, we need to keep in mind that cascading is a non-local process as a result of propagation in a nonlinear medium, and only one single point in the dispersion curve can be obtained at a given time.

Figure 2.4(a) exhibits characteristic signatures of standard cascaded nonlinearities, including a change in the sign of the nonlinear phase shift, the existence of a foreseen maximum and a minimum value on opposite sides of the phasematching for an optimal detuning and a zero cascaded phase shift on phasematching ($\Delta k_0 L = 0$).

Amongst these properties only the change of the sign of the nonlinearity is a general feature of all cascaded scenarios. The other two properties are particular to the case of SHG with CW plane waves in lossless media for uniform wavevector distribution and zero initial second harmonic. Usually there can be more than one local maximum and more than value at which the nonlinear phase shift is zero. For example, under the present conditions with nonzero initial SH, achieving a phase shift at $\Delta k_0 L = 0$ is possible. Furthermore, the study of seeded second harmonic generation has led to the development of an all-optical transistor [14]. Seeded cascaded nonlinearities were not investigated in this work, but they certainly provide a rich variety of additional effects worthy of investigation.



(a)



(b)

Figure 2.4 Typical variation in (a) the nonlinear phase shift $\Delta\phi_{NL}(L)$ and (b) SHG versus detuning from phasematch $\Delta k_0 L$ for different input parameters.

The change of the sign through the phasematching condition is potentially a useful way to control the nonlinearity at any wavelength by proper adjustment of the wavevector mismatch conditions. Such experimental flexibility of the nonlinearity is a unique and powerful characteristic of cascaded nonlinearities that will be discussed later.

Also from Figure 2.4(a) we observe a decrease in the position of optimal detuning $|\Delta k_o L|$ with an increase in the product $\kappa|A_\omega(0)|L$ as a consequence of the quasi-saturation in the nonlinear phase shift depicted in Figure 2.3(a). Because of the detuning, $\Delta k_o L$, which is related to the wavelength through the refractive index dispersion, the dispersive behavior of the nonlinear phase shift suggests that the process has an associated bandwidth which is directly related to the SHG bandwidth. This bandwidth is more evident on Figure 2.4(b) where we observe the classical detuning SHG curve, which resembles the $\text{sinc}^2(\Delta k_o L/2)$ behavior predicted in (2.30) and which will be reconsidered in section 2.3. In Figure 2.4(b) the central peak becomes narrower, the position of the first zero collapses towards the phase matching condition and the side lobes become much more prominent as $\kappa|A_\omega(0)|L$ is increased. At the same time the maximum conversion increases as $\kappa|A_\omega(0)|L$ increases. All these effects are manifestations of cascading. It is interesting to note that there is always a narrowing of the detuning curve, because the nonlinear phase shift always decreases the amount of the phase mismatch, regardless of the detuning, thus collapsing the phasematching curve. This comes as a consequence of the definition of the phase mismatch, where the “cascaded index” associated with the nonlinear phase shift always adds with the same sign to the phase mismatch defined in (2.24).

As a final comment on Figure 2.4, we observe an interesting and non-intuitive numerical property from the calculations of the coupled mode equations (2.34). If the product $\kappa|A_\omega(0)|L$ remains constant, the complex fields of the fundamental and SH are the same for all possible combinations. In other words, if we double any of these three variables and reduce by two either of the other two, to within the accuracy of the numerical computation, the curves depicted in the Figure 2.4 remain the same. The only difference arises when the change is done in the propagation length L . Here, to obtain the same curve, a rescaling of the horizontal axis ($\Delta k_0 L$) by the correspondent factor is required. This is remarkable because it tells us that, in the first approximation, if we cut a device in two and use four times the intensity, we obtain the same detuning curve with twice the bandwidth and vice versa.

Notice that the dimensionless product $\kappa|A_\omega(0)|L$ is also customarily written as $\{(\omega d_{\text{eff}}/n_\omega c)E_\omega(0)L\}$ or ΓL among others. This invariant numerical property can be extended to any representation.

From a practical point of view, the processes associated with a cascading phase shift confront serious limitations. To achieve a large phase shift we must operate near phasematching. Hence we can say that SHG is a coherent resonant process. This means that some SH is selectively generated imposing an effective loss on the fundamental. This loss is not dissipated into other types of energy, but is converted to another frequency. As will be seen later, there are ways to manipulate the wavevector mismatch condition along the propagation path, departing from the simple model described here, that overcome this “loss”.

Low depletion SHG

As already mentioned, the CW plane wave coupled mode equations (2.27) describing SHG have an exact but complicated analytical solution. One approach for obtaining a physical insight was presented as numerical solutions to describe cascading nonlinearities. Another approach commonly used is to do first order analysis under the low depletion approximation. The analysis relies on the assumption that, along the propagation path, the depletion of the fundamental beam is negligible to first order. We talk about a “low depletion regime” when, at any position along the propagation, and for every point in the detuning curve there is not significant depletion. This allows the assumption that $|E_\omega(z)|$ is a constant to first order, linearizing the system and losing all the information about the nonlinear dynamics of the problem. It has the property of describing most of the phenomenological aspects of SHG. Unfortunately it is also commonly generalized to high depletion, carrying with it some misconceptions about cascading effects.

Using the low depletion approximation we can solve (2.27) for the SH field assuming $|E_\omega(z)|=E_\omega(0)=E_\omega$. From direct integration after a propagation length L and zero initial SH we obtain

$$E_{2\omega}(L) = -\frac{\omega d_{eff}}{n_{2\omega} c} E_\omega E_\omega \left(\frac{1}{\Delta k_o} - \frac{e^{-i\Delta k_o L}}{\Delta k_o} \right) \quad (2.35)$$

which is the combination of a free running wave and a wave driven by the nonlinear term (first and second terms respectively), consistent with the cascading description. Multiplying this equation by its complex conjugate and using the relation between the electric field and

intensity ($I = \frac{1}{2} \epsilon_0 c |E|^2$) we obtain the same relation as (2.30) for the low depletion approximation.

$$I_{2\omega}(L) = \frac{2\omega^2}{n_\omega^2 n_{2\omega} \epsilon_0 c} d_{eff}^2 L^2 I_\omega^2(0) \text{sinc}^2 \left(\frac{\Delta k_o L}{2} \right) \quad (2.36)$$

This expression has the elements commonly associated with SHG. The SHG intensity grows quadratically with distance and fundamental intensity. It is proportional to the square of the nonlinearity and has a sinc^2 dependence with respect to detuning. This detuning shape has an associated Full-Width-at-Half-Maximum (FWHM) bandwidth of $(\Delta k_o L)_{BW} = 0.866\pi$. This result is again consistent with the notion presented in the previous section on narrowing of the central peak with increase interaction length.

It is also customary to represent the performance of an SHG device by means of its figure of merit η in the low depletion regime, calculated as

$$\eta = \frac{P_{2\omega}(L)}{P_\omega^2(0) L^2} = \frac{2\omega^2}{n_\omega^2 n_{2\omega} \epsilon_0 c^3} \left[\frac{d_{eff}^2}{A_{eff,\omega}} \right] \text{sinc}^2 \left(\frac{\Delta k_o L}{2} \right) \quad (2.37)$$

where $A_{eff,\omega}$ is the effective cross-sectional area of the fundamental field, either beam size or waveguide area, as will be discussed in the next chapter, and $P = I / A_{eff}$ is the power associated with the CW wave.

This quantity given in units of [% /W-cm²] is independent of the particular testing parameters and relies only on material and geometry properties. It gives a comprehensive way to compare different devices. Most of the work in the SHG community is focused on

maximizing this quantity by a larger nonlinearity or stronger confinement. But as mentioned before, it is only valid in the low depletion regime.

At high depletion, the conversion efficiency saturates, with the SH growing slower than the square of the input power and giving smaller values for η . At the output, the maximum total conversion possible is for all of the input fundamental power to be converted to SHG. If a device is tested at high depletion and extrapolated to low power, it will give a higher value than the real low depletion value. This gives a device performance quantity and not a comparative result, therefore a false interpretation.

Returning to the cascaded nonlinearities, a study is performed to the second order of the coupled mode equations (2.27) in the low depletion regime where the amplitude remains unchanged while small changes in phase are allowed. Including the low depletion result (2.36) in the evolution of the fundamental we obtain the following equation

$$\frac{dE_{\omega}}{dz} = i \frac{\omega^2 d_{eff}^2}{n_{\omega} n_{2\omega} c^2} \left[\frac{-1 + e^{i\Delta k_o z}}{\Delta k_o} \right] |E_{\omega}|^2 E_{\omega} \quad (2.38)$$

Comparing this result to the third order nonlinear case [3] reveals a direct similarity to a third-order induced self-phase modulation type of equation using a complex nonlinear refractive index n_2 :

$$\frac{dE_{\omega}(z)}{dz} = i k_{\omega,o} n_2 I_{\omega}(0) E_{\omega}(z) \quad (2.39)$$

which has a solution of the form

$$E_{\omega}(L)=E_{\omega}(0)e^{ik_{\omega,o}n_2I_{\omega}L} \quad (2.40)$$

From this similarity, an effective nonlinear phase shift due to the cascaded second-order nonlinearity after a propagation L can be deduced as

$$\Delta\phi_{NL}=\frac{\omega^2d_{eff}^2L^2}{n_{\omega}n_{2\omega}c^2}\Re\left[\frac{-1+e^{i\Delta k_oL}}{\Delta k_oL}\right]|E_{\omega}(0)|^2 \quad (2.41)$$

which, when compared to the real third-order nonlinear refractive index n_2 given in (2.13), yields an equivalent nonlinear refractive index

$$n_2^{eff}=-\frac{4\pi}{\epsilon_o c} \frac{d_{eff}^2}{n_{\omega}n_{2\omega}} \frac{L}{\lambda} \left(\frac{1-\cos(\Delta k_oL)}{\Delta k_oL} \right) \quad (2.42)$$

The imaginary part of the kernel in (2.40) leads to an effective two-photon absorption which corresponds to a second order correction of SHG. This correction adds to the previous SHG calculated in (2.36).

The concept of an effective nonlinear refractive index has to be taken with extreme caution. Normally the nonlinear refractive index is associated with a real change in the material properties that leads, for example, to all-optical devices [2] through a third-order nonlinear phase shift. As mentioned before, more important from a device standpoint is the total nonlinear phase change.

In second-order nonlinearities there is a real nonlinear phase shift that does not create a real change in the refractive index. It has a larger potential indeed, but it is also accompanied

by a loss to the second harmonic. The concept of an effective nonlinear refractive index is therefore a valid liason between the old $\chi^{(3)}$ school and the cascading nonlinearity, but with the potential of creating a syntax confusion.

All the analytical results obtained under the low depletion approximation grant this approximation a unique status. It is a powerful tool with which to perform material characterization and, at the same time, provides a simple and comprehensive picture of SHG. Therefore it is hard to eliminate the misinterpretation that sometimes arises. Equally hard is to define the point up to which extending the approximation is valid.

Mathematically the low depletion approximation is only valid for a small range of parameters. In practice the conditions are more relaxed. Numerically we can find an agreement with the exact solution to better than 5% if the product $\kappa|A_\omega(0)|L$ is smaller than one. For example, in Figure 2.4(b) the curve with $\kappa|A_\omega(0)|L=0.5$ resembles the sinc^2 behavior with the zeros in the correct position. As a rule of thumb, if $\kappa|A_\omega(0)|L$ is less than 0.05 we are in the low depletion regime and if it is larger than one it is clearly in the high depletion regime. Using real values as an example, in a 1 cm long sample of LiNbO_3 with $d_{\text{eff}} = 31.8 \text{ pm/V}$ at $1.55 \text{ }\mu\text{m}$, the upper limit for the intensity in the low depletion regime is around 46.5 kW/cm^2 and the lower limit for the high depletion regime is 0.93 MW/cm^2 . Experimentally, the low depletion approximation has proven to be accurate up to 30% effective conversion efficiency. At higher conversion it breaks down significantly.

2.4 Characteristic Lengths

We have seen that second harmonic generation requires some joint propagation of the fundamental and harmonic to occur, i.e., a non-local process. In the idealized SHG system described in (2.34), the interaction length could be infinite. In reality additional mechanisms shorten the effective interaction length, identified by an associated finite characteristic length. Some of these are inherent to the SHG process, and others depend on the particular scenario. As we will see next, some of these lengths could be perceived as limiting effects, because they constrain the length of the interaction between the fundamental and second harmonic fields in space. However, at the same time, these lengths are associated with fundamental effects in second harmonic generation, some of which give rise to the novel effects presented in this work. Therefore, these characteristic lengths have to be understood and compared to identify their relevance.

The nonlinear interaction will always be dominated by the shortest of these characteristic lengths. This means that the outcome of the collective system will have predominantly the features of the phenomena that have the associated characteristic length. Even though we can diminish or neglect the contribution from other effects, however, all of the effects are intermixed and always present. We can expect deviation from an ideal model all the time and, as mentioned previously, be aware of possible differences. Identifying which are the relevant deviations from the model becomes a real challenge. We turn our attention back to the full description of SHG described in equations (2.25) and (2.26). Each of the terms involved has an associated characteristic length in which the phenomena evolve. Next, eight different characteristic lengths will be identified.

Device Length

The first length and most trivial length is the “device length” (L). Identifying this length as a characteristic length is not obvious. It is defined as the distance over which the coupled mode equations have to be integrated in which the nonlinearity (κ) exists. This is the ultimate limitation of all nonlinear processes, because there are no infinite lengths in real materials. On the other hand, its finite dimension encourages us to search for different ideas to maximize the usefulness of the nonlinear processes with the technologically available device lengths. For example, optimization can lead to solutions such as two different bulk second order crystals mounted at different angles with some air space in the middle, where diffraction can still occur. More complex geometries could be conceived. We can include the analysis of the interaction “device length” as a part of a more complex nonlinear system, as is done in SHG seeded experiments. Ultimately all other characteristic lengths are compared with the device length. It does not carry any particular new effects associated with it, but if this is the shortest length of all, no efficient SHG or cascading effects can be observed.

Coherence Length

When there is a finite amount of wavevector mismatch between the fundamental and the second harmonic, the second harmonic which is generated earlier along the sample, will be out of phase with that generated at a later position. Due to this interference, the second harmonic will convert back and forth to the fundamental. Observing the evolution of the fundamental in Figure 2.2(b), we can see a periodic exchange of energy. In the low depletion regime, a sinusoidal evolution of the fields, as a consequence of this exchange of energy

between the fundamental and the second harmonic, is observed. The typical distance in which the relative phase between the fundamental and second harmonic fields changes by π is defined as the coherence length (L_c), and is given by

$$L_c = \frac{\pi}{\Delta k_o} = \frac{\lambda}{4(n_\omega - n_{2\omega})} \quad (2.43)$$

After propagation of two coherence lengths, the fundamental is fully restored with a net cascade second order phase shift. Notice that the definition of the coherence length given in (2.43) is only valid in the low depletion regime. For large depletion the cascade phase shift further dephases the waves leading to an intensity dependent coherence length. This characteristic length is intrinsic to SHG, and is a measure of the power exchange between fundamental and second harmonic. For example, if the coherence length is exactly half of the device length we will have full recovery of the fundamental which corresponds to the case $\Delta k_o L = 2\pi$ which is the first zero in the low depletion SHG detuning curve in (2.36). We can also associate this coherence length with the filtering properties of the collective SHG process. If we consider a white light source, with an ideal uniform spectrum, the SHG process will “filter” the spectrum exactly to the shape of the detuning curve. The width of the filter and all the characteristics are dominated by the ratio between the coherence length to the device length ($L / L_c = \Delta k_o L / \pi$). This coherence length will be used again when we talk about phasematching techniques in the next section.

Due to the possibility of spatially varying the wave vector mismatch along the propagation path, the coherence length can also be spatially varied along the propagation axis.

This is in addition to the power dependent coherence length previously mentioned. These properties give rise to one of the novel effects studied in this work, namely spatial nonuniformity and spatial nonreciprocity. It will be detailed in chapters 4 and 5.

Nonlinear Length

Second harmonic generation is an intrinsic nonlinear process. But as we outlined in section 2.3 we can linearize the problem in the low depletion limit, and therefore lose information on the full nonlinear dynamics of the system. In particular the details of how the nonlinear phase shift is imposed onto the fundamental is lost. The third intrinsic length associated with SHG, the nonlinear length (L_{NL}), is a measure of the transition distance between the high and low depletion regimes as it provides the length scales over which cascaded nonlinear effects become important.

The nonlinear length, also known as the *parametric gain length*, is related to the first term in the right hand side of equations (2.25) and (2.26), and it is defined as

$$L_{NL} = \frac{1}{\kappa |A_{\omega}(0)|} \quad (2.44)$$

If this length is one of the shortest of the characteristic lengths, we can expect to observe cascading effects, such as an intensity dependence of the detuning curve. It also provides a clear explanation of two of the topics discussed earlier. First, it sets a well-defined boundary between the low and high depletion regimes. It was empirically set at $\kappa |A_{\omega}(0)|L \approx 1$, where L is the device length. From (2.44), we observe that it corresponds to a device length

shorter or longer than the nonlinear length, respectively. Second, it justifies the invariance property of the detuning curve for a constant $\kappa|A_\omega(0)|L$ product. If this product remains constant, the nonlinear length also remains constant, and therefore the nonlinear dynamics stays invariant. This length is also responsible for a novel effect studied in this work, namely the intensity dependent multimode competition to be analyzed in the next chapter.

Loss Length

So far we have analyzed a conservative system, where the loss of the fundamental is only possible through conversion to the second harmonic. This property defines a Hamiltonian system, where all the energy is conserved. But in the real world energy can escape the system due to absorption losses, scattering losses, or waveguide losses amongst others.

These losses limit the interaction between the two fields and change the results away from those discussed in the previous sections. We identify the losses with the last term in equations (2.25) and (2.26). Using an exponential decay law, we define the loss length (L_α) as the point where the intensity has decreased by $1/e$, given by

$$L_\alpha = \frac{1}{\alpha_\Omega} \tag{2.45}$$

where $\Omega = \{\omega, 2\omega\}$, and α_Ω is the loss coefficient introduced in the complete coupled mode equations. This length is the only one among the characteristic lengths that is intrinsically a limiting process. There is no possible positive effect that can be extracted from this, and the

only solution is to overcome the losses by using a device length as well as other characteristic lengths shorter than this one.

A solution to the SHG problem can be obtained in the low depletion regime in the presence of loss [26]. The second harmonic power then becomes

$$P_{2\omega} = 2\eta_o P_{\omega}^2 e^{-(\alpha_{\omega} + \frac{\alpha_{2\omega}}{2})L} \frac{\cosh(\Delta\alpha L) - \cos(\Delta k_0 L)}{(\Delta\alpha)^2 + (\Delta k_0)^2} \quad (2.46)$$

where η_o is the low depletion figure of merit (2.37), $\Delta\alpha = (\alpha_{2\omega}/2 - 2\alpha_{\omega})$, and L is the device length. It is interesting to note that if the condition $\Delta\alpha = 0$ is satisfied, we obtain the same $\text{sinc}^2(\Delta k_0 L/2)$ detuning curve, with the peak conversion efficiency reduced by a linear factor $\exp\{-(\alpha_{\omega} - \alpha_{2\omega}/2)L\}$. So that even in the presence of losses we can obtain an “ideal” detuning curve.

Diffraction Length

In nonlinear optics, large intensities are usually required to observe nonlinear effects. In bulk materials the intensity is increased locally by focusing a laser beam. However, the tighter the beam is focused, the faster it will diverge due to diffraction. We identify diffraction with the transverse Laplacian in the left-hand side in equations (2.25) and (2.26). For a Gaussian beam we define the diffraction length as the length in which the beam diameter increases by a factor of $\sqrt{2}$. This distance is given by

$$L_{D,z}^{\Omega} = \frac{\pi n_{\Omega} a^2}{\lambda} \quad (2.47)$$

where $\Omega=\{\omega,2\omega\}$, and \mathbf{a} is the waist of the beam. As the beams propagate, the area of both the fundamental and second harmonic beams is increased, therefore reducing the intensity and limiting the interaction distance over which efficient SHG process occur. This limiting process can be overcome only if the nonlinear length is shorter than the diffraction length. This trade-off between the diffraction and the nonlinear length leads to one of the most exciting manifestations of a cascaded nonlinearity, the existence of one-dimensional [15] and two-dimensional [16] spatial solitons. These effects were not studied as part of this work, but they are part of the new and exciting effects present in cascading nonlinearities. The work done in this dissertation involves propagation in channel waveguides, in which the beam is confined in both transverse dimensions and diffraction is overcome.

Spatial Walk Off Length

In a general SHG geometry, the fundamental and SH beams may not propagate along the principal axes of a $\chi^{(2)}$ crystal. For example, the propagation direction of the phase front can deviate from the energy flow propagation direction by an angle $\rho_\omega - \rho_{2\omega}$, causing the beams to walk away from each other, thus limiting the interaction length. This is included as the spatial derivative which includes the walk-off angles in equations (2.25) and (2.26). We define the “walk-off length” as the distance required for two beams of radius \mathbf{a} to separate one full beam width from another and is given by

$$L_{w,z} = \frac{2a}{\tan(\rho_\omega - \rho_{2\omega})} \quad (2.48)$$

Note that walk-off is absent along the principal axes of a crystal, as it occurs for noncritical phasematching. Walk-off can be overcome if the nonlinear length is shorter than the walk-off length within the device, bonding the two beams together. These are known as ‘walking’ solitons [27]. Once again, these effects were not studied as part of this work, but they are part of the full description of SHG and cascading nonlinearities.

Temporal Walk Off Length

In the temporal case, we can increase the field intensity by using short pulses instead of a CW beam. This will redistribute the energy in time, and if we are in the presence of fast nonlinearities, as occurs in most $\chi^{(2)}$ materials, it will increase the peak intensity available to observe larger nonlinear effects. At the same time any material exhibits a certain amount of dispersion with frequency. That means that two optical waves of different frequency and with the same polarization in general can never travel at the same velocity. Consequently, the fundamental and second harmonic pulses will travel at different velocities, ‘walking’ away from each other. These effects are included as the first order temporal derivatives in equations (2.25) and (2.26). The temporal “walk-off length” is defined as the distance over which two pulses will move apart by one intensity FWHM. For a pulse of width T_o this distance is given by

$$L_{w,t} = \frac{T_o}{k'_{2\omega} - k'_{\omega}} \quad (2.49)$$

were k'_{ω} and $k'_{2\omega}$ are the group velocities at the centers of the pulses. This walk-off length represents the group velocity mismatch. If the pulses walk away from each other, the interaction between them is then reduced. Notice that, depending on the refractive index dispersion and the wavelength region, this quantity can be either positive or negative. There is no known application to date for this limiting effect, although some large cascaded phase shifts due to this effect have been predicted [28]. This is also the cause of “self-phase-modulation” effects in pulse propagation in SHG [12]. After a detailed analysis we can conclude that propagation over distances shorter than the temporal walk-off length allows us to use the CW approximation, or in other words, ignore the pulse nature of a pulse.

Dispersion Length

Most materials, exhibit group velocity dispersion (GVD) in addition to refractive index dispersion. This effect causes the different frequencies which make up a pulse to travel at different speeds, which in turn causes a spectral broadening of the pulse. The redistribution of frequencies in a dispersive medium causes a broadening of the temporal shape of the pulse and, as a consequence, a reduction in peak pulse intensity. We identify this effect with the second order temporal derivatives in equations (2.25) and (2.26). Assuming a gaussian envelope, the distance in which the intensity pulse envelope doubles its width is defined as the “dispersion length”, given by

$$L_{D,t}^{\Omega} = \frac{T_0^2}{|k''_{\Omega}|} \quad (2.50)$$

where $\Omega = \{\omega, 2\omega\}$. The effect of the broadening of the spectrum, combined with the filtering effects of the SHG detuning curve, creates a direct self-phase-modulation of the pulse spectrum, in addition to the reshaping due to the walk-off length. Fortunately in most materials the GVD is relatively small, and therefore this is usually by far the longest characteristic distance involved, except when dealing with femtosecond pulses.

To illustrate the relative magnitude of the characteristic lengths, we will calculate here the characteristic lengths using real parameters for two different configurations. Assuming nonseeded propagation of 100 mW average power at a fundamental wavelength of 1.55 μm in a 1 cm sample of LiNbO_3 , and using the d_{33} ($=31.8 \text{ pm/V}$) coefficient and loss coefficients of 0.35 dB/cm at the fundamental and 0.68 dB/cm at the SH, consider:

(a) a CW beam focused to a 500 μm diameter spot (low power)

(b) a 6 picosecond pulse at 76 MHz focused to a 10 μm diameter spot (high power).

We will assume that the crystal is perfectly phasematched along the optical axis so that the walk-off length is infinite.

The product $\kappa|A_o(0)|L$ is 0.013 for (a) and 32.5 for (b). Comparing the numbers, we can see that case (a) is clearly operating in the low depletion regime, and the device length is the dominant length. For case (b) the dominant characteristic length is the nonlinear length, and without going into detail, we can expect to observe strong cascaded effects in this case, with some influence from diffraction and temporal walk-off contributions.

Table 2.1 Comparison between characteristic lengths for low and high power beams

| Characteristic | length | (a): low power | (b): hi power |
|----------------------|----------------------|----------------|-------------------|
| Device | L | 1 cm | 1 cm |
| Nonlinear | L_{NL} | 68.1 cm | 318 μm |
| Loss ω | $L_{\alpha,\omega}$ | 12.8 cm | 12.8 cm |
| Loss 2ω | $L_{\alpha,2\omega}$ | 6.4 cm | 6.4 cm |
| Diffraction | $L_{D,z}$ | 3.9 cm | 590 μm |
| Spatial Walk-off | $L_{w,z}$ | ∞ | ∞ |
| Dispersion ω | $L_{D\omega,t}$ | ∞ | > 300 m |
| Dispersion 2ω | $L_{D2\omega,t}$ | ∞ | > 1 km |
| Temporal Walk-off | $L_{w,t}$ | ∞ | 2.1 cm |

2.5 Phase-Matching Techniques

In second order nonlinear process, the interaction which occurs between beams with different frequencies is coherent. Therefore, as discussed earlier, efficient SHG requires that the phasematching condition be satisfied. Also mentioned was the importance of the phasematching parameter on the cascaded nonlinearities. Even though the cascaded second order nonlinearity requires a finite phase mismatch, to obtain a nonlinear phase shift a reasonable amount of SHG is a prerequisite. As a result, operating near phasematching is also important for cascading. The two most common methods to achieve phasematching in bulk media are birefringent phasematching and quasi-phase-matching (QPM).

Birefringent Phasematching

All materials exhibit a certain amount of dispersion with frequency. That means that two optical waves of different frequency and with the same polarization can never travel at the same velocity. For anisotropic media the refractive index changes according to the polarization direction of the incident beam. Also, due to the tensor nature of the second order susceptibility, the generated beam due to the second order process can have a different polarization direction from that of the input beam. Therefore, with the proper choice of the polarization of the input beam, phasematching can be possible between two beams with different frequencies.

In general, an optical beam which propagates inside a birefringent material can be labeled as an ordinary ray (o-ray) or an extraordinary ray (e-ray). If the polarization of the beam is parallel to a principal axis of the crystal, it is called an o-ray. The refractive index for an o-ray is independent of the propagation direction. If the polarization of the beam lies in a plane which contains two principal axes with different refractive indices, it is called an e-ray. For an e-ray, the refractive index is a function of the propagation direction.

Birefringent phasematching can be divided into two classes: type I and type II [17]. If we mix two fundamental beams with the same polarization to obtain a second harmonic beam with a different polarization, it is called type I phasematching. In a type II interaction, the fundamental is a combination of both polarizations, one e-ray and one o-ray, to create either an e-ray or an o-ray second harmonic beam. Uniaxial crystals such as LiNbO_3 have one optic axis. They can exhibit either positive or negative birefringence, depending on the relation between the refractive indexes ($n_o > n_e$ for negative uniaxial crystals and vice versa).

Biaxial crystals, such as KTP, have two optic axes, which means that the principal axis system is fixed in relation to the crystal axes such that $n_z > n_y > n_x$. There is a whole field in nonlinear crystallography dedicated to the study of the phasematching possibilities. Details are beyond the scope of this dissertation and can be found in the literature [17].

To achieve the phasematching condition, it is necessary to change parameters such as temperature, wavelength or propagation angle which vary the refractive index of the material. Angle tuning is widely used in practice to roughly find the phasematching conditions, and temperature tuning or wavelength tuning to fine tune the phasematching. One important aspect of birefringent phasematching is that only off-diagonal elements of the d -tensor can be used since the fundamental and second harmonic fields are orthogonally polarized. These elements are typically smaller than the diagonal elements. Also, since the fields are generally not polarized along the crystal axes, we need to use the d_{eff} coefficient mentioned earlier. Cutting a crystal to a certain phasematching angle for SHG at a given wavelength and then using angle tuning to optimize the phasematching is the preferred method for bulk SHG.

Quasi-Phase-Matching (QPM)

Another technique for achieving phasematching was initially proposed by Armstrong *et al* in 1962 [1] but has only recently come into widespread use [29]. This is called quasi-phase matching, where the sign of the d_{eff} is periodically changed. QPM can also be achieved through a periodic variation of the linear refractive index, but it is not as efficient as a nonlinear coefficient variation [30]. It has been demonstrated in ferroelectric crystals [29], as well as in polymer materials [30]. The big advantage of this technique is that the diagonal

elements, which are not normally phasematchable via birefringent phasematching, can be used. Another advantage of QPM is the possibility of tailoring the wavevector mismatch condition along the sample by chirping the grating. This property will be used in chapter 4 to obtain a controlled detuning curve.

As previously mentioned, when there is a finite amount of wavevector mismatch between the fundamental and the second harmonic. The second harmonic, which is generated earlier along the sample, will be out of phase with that generated at a later position. Due to this interference the second harmonic will convert back and forth to and from the fundamental. This exchange of energy is periodic. The period of this energy exchange is given by the coherence length (2.43), where the Δk_0 is the material wavevector mismatch. If the sign of the effective nonlinearity, d_{eff} , is flipped or destroyed every coherence length, there will be no destructive interference and an effective growth of the second harmonic occurs, therefore achieving phasematching. This is a convenient way to obtain phasematching when the material is nonphasematchable, or when propagation along an optical axis is desired.

This spatial domain picture has an analogy in the Fourier domain, where the momentum vector associated with the grating acts to compensate for the wavevector mismatch of the material, thereby achieving momentum conservation, which is equivalent to phasematching (Figure 2.5). Thus, the phasematching condition is written as

$$\Delta k_0 = 2k_\omega - k_{2\omega} - K = 0 \quad (2.51)$$

where $K = 2\pi m/\Lambda$ is the wavevector associated with of the m^{th} Fourier component of the grating, and Λ is the period of the grating.

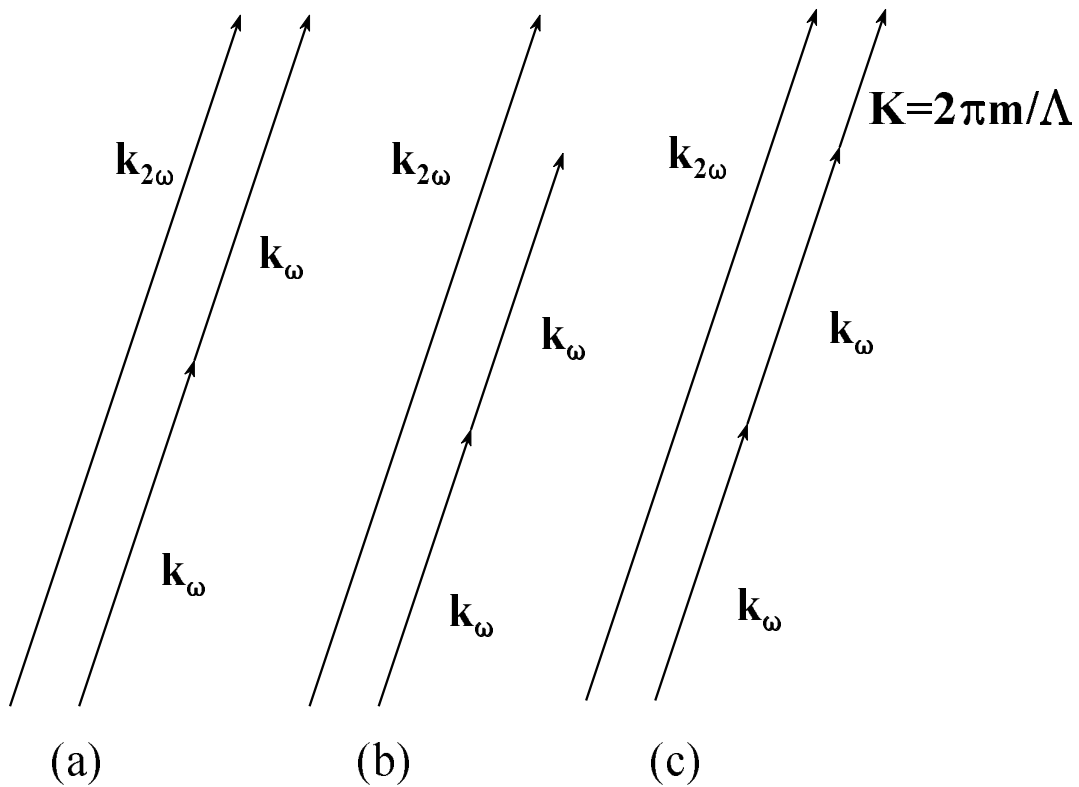


Figure 2.5 Phase matching vector diagram for (a) birefringent phasematching, (b) non-phasematched case and (c) quasi-phasematching.

This implies that a sinusoidal grating which has only a single Fourier component would be ideal for perfect phasematching, while gratings with other shapes are not as effective due to the spread of spatial frequency components. The integer \mathbf{m} is called the QPM order, and first-order QPM yields the most efficient interaction. The wavevector picture doesn't reveal any information about the effect the grating on the effective nonlinearity. However, a detailed analysis [31] shows that the effective nonlinearity is weaker due to a nonlinear grating. A detailed Fourier analysis of QPM reveals that the value of d_{eff} is reduced by a factor

$(2/m\pi)\sin(\pi mD)$, where D is the duty cycle of the grating [29]. This analysis includes a Fourier analysis of nonuniform, or chirped, gratings.

Using a spatial representation, we obtain phasematching by the m^{th} order of the grating. But all other grating periods (Fourier components) also are involved in SHG processes which are not phase-matched. For example, this includes the zero-order, or the original material phase mismatch. All are present “simultaneously,” and will lead to a periodic exchange of energy defined by their respective coherence lengths, although only one will create an efficient SHG. Only the superposition of all the processes can be observed. We can even obtain simultaneously more than one second order process, as will be discussed in the next chapter. Therefore the SH growth will not be uniform. There will be a slow oscillation (the phasematched order) with some fast oscillations imposed due to the other processes.

CHAPTER 3

WAVEGUIDE SHG MULTIMODE COMPETITION

Science is always wrong. It never solves a problem without creating ten more.

G.B. Shaw

Nonlinear optical processes require high intensity light beams to make their effects observable and useful. As we have seen, the efficiency of processes like SHG typically increases with the interaction length and with the intensity of the optical fields involved. In bulk materials the intensity is increased by focusing a laser beam into them. However, the tighter the beam is focused, the faster it diverges due to diffraction, thus limiting the interaction length. Other effects are also present as discussed earlier, such as spatial walk-off. This situation is greatly simplified by using optical waveguides. The ability of waveguides to maintain high intensities over relatively long lengths has made them ideal structures for the study of nonlinear optics.

The reasons for using waveguides for second harmonic generation (SHG) are well documented [29,32]. The spatial confinement to beam cross-sectional areas of the order of the wavelength squared for centimeter distances results in high conversion efficiencies at

relatively low input power levels. Furthermore, because waveguides can support multiple modes at the same frequency but with different wavevectors, there is much more flexibility in wavevector-matching than is available with plane wave interactions in bulk media. The invention of quasi-phase-matching (QPM) and segmented phase-matching techniques have allowed the large diagonal second order coefficients of LiNbO_3 and KTP to be effectively used for waveguide SHG [31,33]. There is a price for this additional flexibility, namely the field overlap with higher order modes, which can reduce the overall conversion efficiency. An additional penalty is also present as a novel effect unique to waveguides. There can be crosstalk between the different waveguide modes through the nonlinear process. This is contrary to the common belief of independence of waveguide modes. This crosstalk additionally happens to be intensity dependent.

A fundamental guided mode simultaneously couples to all the SH guided modes of the structure and phase-matching chooses which SH modes will preferentially grow. Due to the small refractive index differences produced by waveguide fabrication techniques the harmonic guided modes can be very closely spaced in wavevector and can be simultaneously generated. The nonlinear phase shift induced by one harmonic can affect the phase-matching condition for another harmonic mode detuned from it by many SHG bandwidths. That is, power exchange between one of these SH modes and the fundamental can lead to a nonlinear phase shift for the other SH modes. For large conversion efficiencies and closely spaced modes the second harmonic generation process can be severely distorted by this nonlinear phase change [34]. In the following sections these effects will be analyzed and some experimental results presented.

3.1 Review of Waveguides

A waveguide is a structure which confines light in one or two dimensions while allowing propagation in the third. Their use to propagate microwaves predates the invention of the laser [35]. In the optical region, there is an extensive bibliography which details the theoretical analysis of dielectric waveguides [37, 38, 39]. Only basic concepts and results relevant to this dissertation will be presented here.

Waveguides can be classified into two major categories: one or two dimensional confinement. The most popular type of waveguide is an optical fiber which belongs to the two dimensional confinement category. The fundamental requirement for confinement in a dielectric waveguide is that the index of refraction of the guiding layer must be larger than that of the surrounding regions. Guiding can be thought of geometrically as total internal reflection at the interfaces between the high index core region and the surrounding media, or as the electromagnetic normal modes of the structure which satisfy Maxwell's equations and the pertinent boundary conditions.

Slab or planar waveguides confine the light in one dimension while diffraction can still occur in the plane of the slab. Due to ease of fabrication and analysis, slab waveguides are one of the favorite waveguide formats for material characterization. In isotropic media or for field orientations along crystal axes with a high degree of symmetry, the waveguide eigenmodes are relatively simple in form, maintain their transverse profile as they propagate, have a definite and unique propagation vector, and are orthogonal to each other. This is always true! Channel waveguides can provide additional confinement in the transverse direction with the same basic characteristics. Typical geometries are depicted in Figure 3.1.

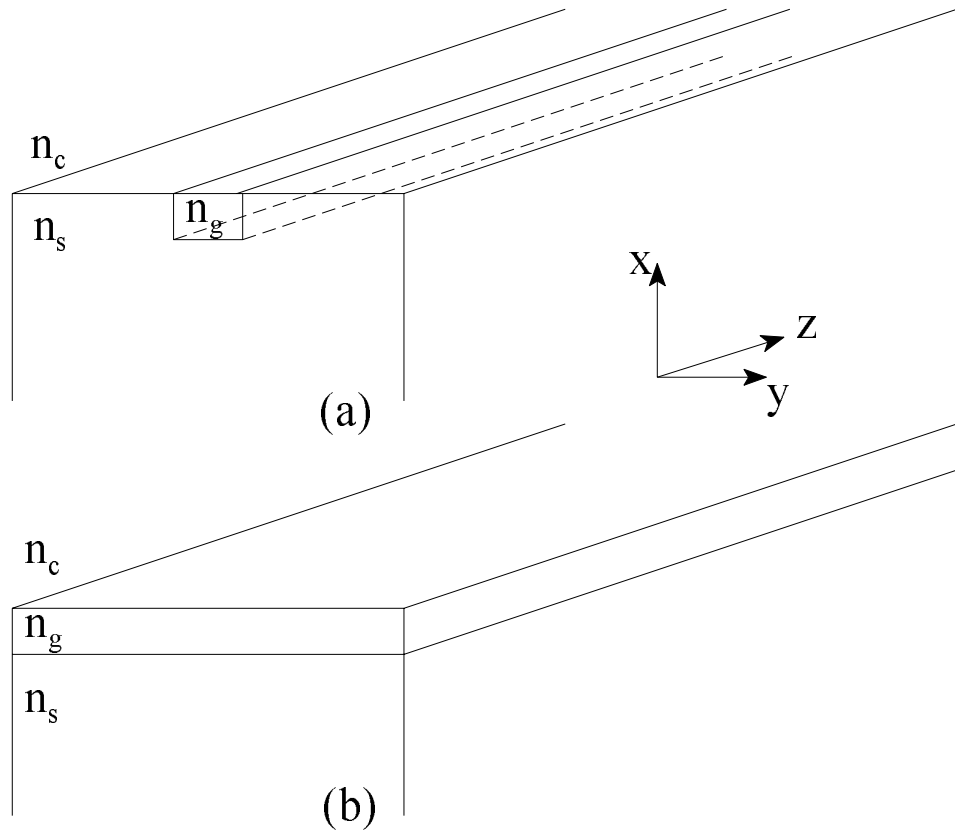


Figure 3.1(a) Channel and (b) planar waveguide typical geometries. In both cases: $n_g > n_s, n_c$

Because light is confined in the waveguide by an index discontinuity, guided waves are a summation of the discrete eigenmodes which are solutions for the boundary problem [39]. The interaction between guided modes in linear as well as nonlinear optics is usually treated with coupled mode theory, which is a very powerful technique. For slab waveguides the modes are linearly polarized transverse electric (TE_m) and transverse magnetic (TM_m), meaning that there is no longitudinal component of the electric or magnetic field along the propagation direction, respectively. In TE modes the electric field polarization lies in the y -direction, parallel to the plane of the film and orthogonal to the propagation direction z . For

TM modes, the magnetic field is polarized in the y -direction, hence the electric field is polarized in the x - z plane. For TM modes, there is a component of the electric field along the propagation direction, but usually $E_y \gg E_z$. The mode number m represents the number of zero point crossings of the electric field across the confinement dimension. Figure 3.2 shows the geometry of the planar waveguide modes and the typical electric field profiles for the lowest order modes. The modal field distribution can be found exactly by solving Maxwell's equations subject to the boundary conditions. Most of the work done in this dissertation involved channel waveguide geometries, therefore a detailed analysis of the more complicated channel waveguides is required.

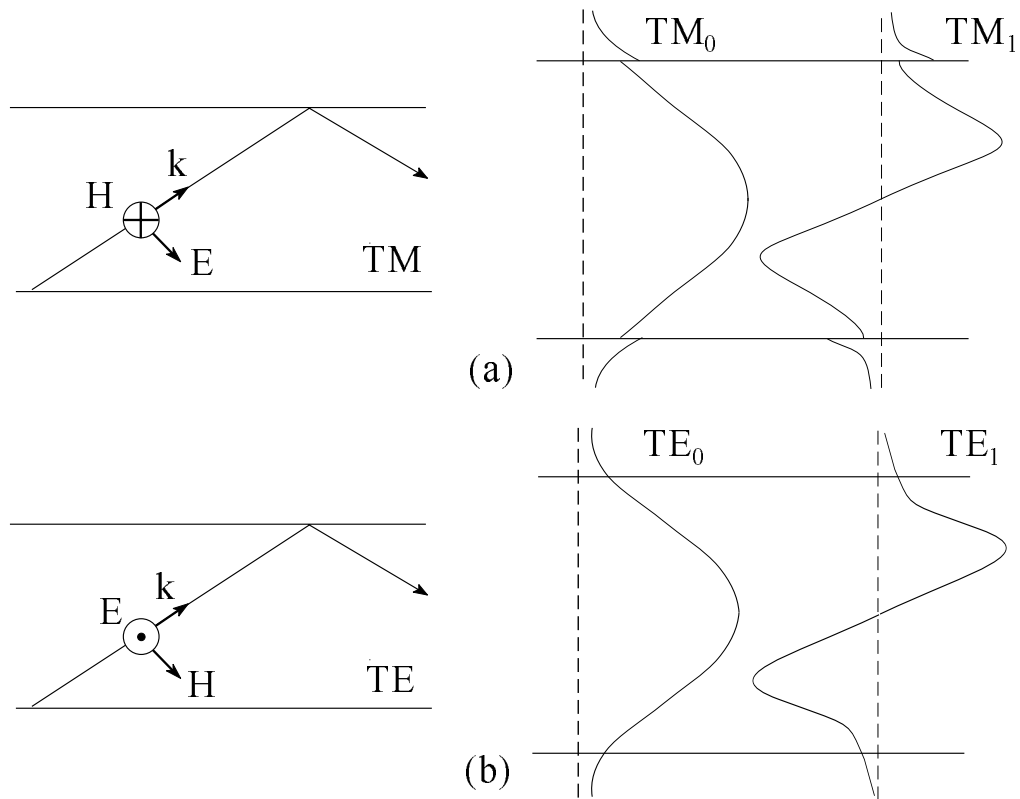


Figure 3.2 Slab waveguide (a) TM and (b) TE vectors (left) and typical electric field mode profiles (right).

Channel waveguides impose confinement in a second dimension. Their eigenmodes also consist of a series of discrete modes. In this case the field polarization includes components along all three axes. Although not purely linearly polarized, these modes can still be labeled TE_{mn} and TM_{mn} in analogy to the planar case. Here TE means that the electric field is predominantly transverse to the propagation direction, and similarly for TM the magnetic field is predominantly transverse. Therefore for TE_{mn} modes $E_y \gg E_x, E_z$ and for TM_{mn} modes $E_x \gg E_y, E_z$. Two indices are needed for channel waveguides because there are two independent confinement directions.

Considering only forward propagating modes, the electric field can be written as [40]

$$E(x,y,z,t) = \frac{1}{2} \sum_{m,n} E^{(mn)}(x,y) C_{mn} a_{mn}(z) e^{i(\beta_{mn}z - \omega t)} + c.c. \quad (3.1)$$

where $E^{(mn)}(x,y)$ is the transverse field profile, and m and n refer to the mode numbers corresponding to confinement in the y - and x -direction, respectively. C_{mn} is a normalization constant such that $|a_{mn}(z)|^2$ is the slow-varying guided wave power, and β_{mn} is the mode propagation constant defined by

$$\beta_{mn} = k_0 N_{mn}^{eff} \quad (3.2)$$

where N_{mn}^{eff} is the effective refractive index of the mode and $k_0 = 2\pi/\lambda$. The refractive index of the mode is constrained to values lying between the index of refraction of the core guiding region and the largest index of the bounding media. Solutions with propagation constant outside this range are either radiation modes in the bounding media, or exponentially decaying

fields along the propagation direction. The values of N_{mn}^{eff} are found from the dispersion relations for the allowed modes for a given geometry and optical frequency. For example, typical guided mode effective refractive indexes for a slab waveguide are shown in Figure 3.3.

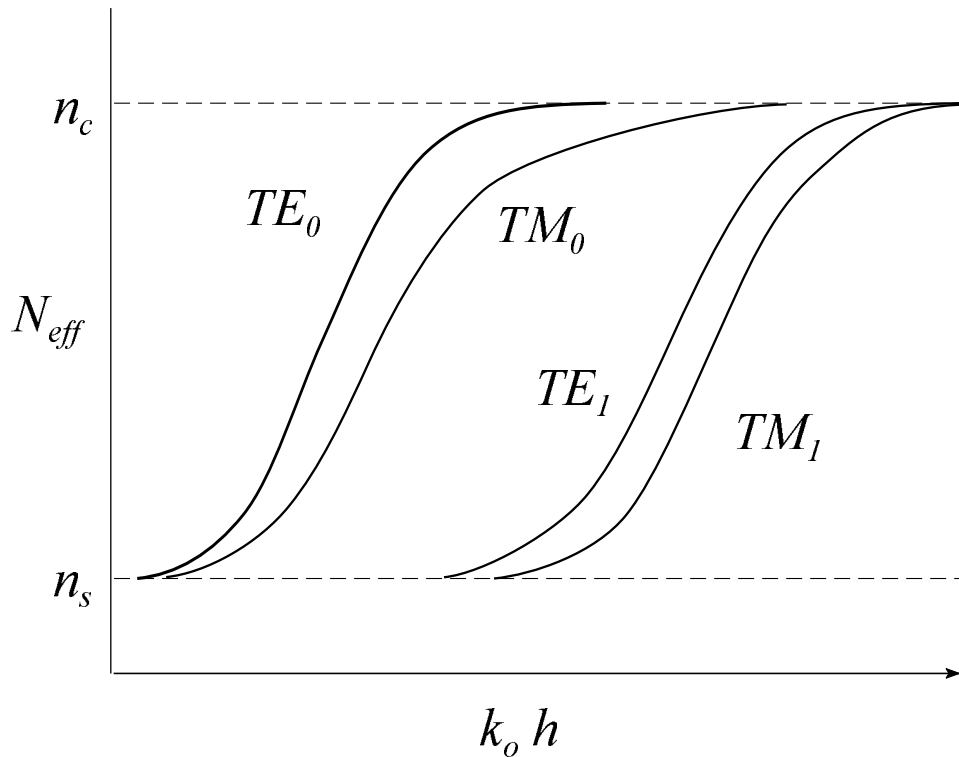


Figure 3.3 Variation in the effective refractive index N_{eff} with normalized film thickness for the first two TE and TM modes for a slab waveguide with substrate index n_s , film index n_c , and film thickness h .

These linear TE and TM modes are always orthogonal, and modes of the same polarization but with different indexes m and n are also orthogonal. This orthogonality is expressed as

$$\frac{1}{2} \int_{-\infty}^{\infty} \int_{-\infty}^{\infty} C_{mn} E^{(mn)}(x,y) C_{m'n'}^* E^{*(m'n')}(x,y) dx dy = \frac{k_o c \omega}{\beta_{mn}} \delta_{mm'} \delta_{nn'} \quad (3.3)$$

For slab waveguides there is no index \mathbf{n} (or \mathbf{n}') and the integration is only over the x coordinate. In nonlinear optics, the nonlinear medium can be either the guiding region or one or more of the surrounding media, or any combination of media. We will only concentrate on the case that the nonlinear interaction occurs in the guiding region.

3.2 Waveguide SHG

As mentioned previously, waveguides provide a suitable geometry for efficient SHG. The spatial confinement to beam cross-sectional areas of the order of the wavelength squared for centimeter distances results in high conversion efficiencies at relatively low input power levels. Because there is a spatial confinement, no spatial walk-off or diffraction reduces the SHG interaction.

To study the second harmonic generation interaction in waveguides we proceed to introduce a set of coupled mode equations similar to those in chapter two. Doing the analysis in the frequency domain and expanding the wave equation (2.1) inside the waveguide under the SVEA, using the electric field definition (3.1), the orthogonality of the modes (3.3), and the coupled mode theory, we obtain a set of coupled mode equations for the waveguide fields [41] given by

$$\begin{aligned} \frac{d}{dz}a_{m'n'}(z,\omega) - i\beta_{m'n'}(\omega)a_{m'n'}(z,\omega) &= -\frac{i\omega}{4} \int_{-\infty}^{\infty} \int_{-\infty}^{\infty} P^{(2)}(\vec{r},\omega) E^{*(m'n')}(x,y,\omega) dx dy \\ \frac{d}{dz}a_{mn}(z,2\omega) - i\beta_{mn}(2\omega)a_{mn}(z,2\omega) &= -\frac{i\omega}{2} \int_{-\infty}^{\infty} \int_{-\infty}^{\infty} P^{(2)}(\vec{r},2\omega) E^{*(mn)}(x,y,2\omega) dx dy \end{aligned} \quad (3.4)$$

These equations describe, within the validity of the coupled mode theory, the evolution of the fields inside the waveguide. Up to this point, the analysis is completely general and only standard assumptions have been done. Because the analysis is in the frequency domain, a short pulse in the time domain can be resolved into a sum of its frequencies using the Fourier transforms (2.21) and (3.4) without loss of generality. This allows us to study the field evolution along the propagation direction and further simplify the problem by neglecting temporal effects. We use now the definition of the nonlinear polarization for $P(\mathbf{r},\omega)$ and $P(\mathbf{r},2\omega)$ in equation (2.18). Notice that the definition of the nonlinear polarization includes the complete electric field at both frequencies described in (3.1), and not a particular mode. At this point, it is frequently assumed that efficient nonlinear coupling occurs only between one fundamental and one SH guided mode. *A priori* there is no reason to assume that there cannot be an interaction with more than one mode. Due to the small refractive index differences produced by waveguide fabrication techniques in these materials, the harmonic guided modes can be very closely spaced in wavevector, can be simultaneously generated, and as we will see, the nonlinear phase shift induced by one harmonic can affect the phase-matching condition for another harmonic mode. The overlap integral and the wavevector mismatch, defined next, will determine which modes interact.

Assuming Kleinman's symmetry and based on the discussion of d_{eff} presented in chapter two, the coupled mode equations describing the evolution of the fundamental and SH fields are

$$\begin{aligned} \frac{d}{dz}a_{m'n'}(\omega) - i\beta_{m'n'}(\omega)a_{m'n'}(\omega) &= -\frac{i\omega\varepsilon_0 d_{\text{eff}}}{2} \sum_{m,n} K_{m'n'mn}^{(2)} a_{m'n'}^*(\omega) a_{mn}(2\omega) \\ \frac{d}{dz}a_{mn}(2\omega) - i\beta_{mn}(2\omega)a_{mn}(2\omega) &= -\frac{i\omega\varepsilon_0 d_{\text{eff}}}{2} \sum_{m',n'} K_{m'n'mn}^{(2)} a_{m'n'}(\omega) a_{m'n'}(\omega) \end{aligned} \quad (3.5)$$

where $K_{m'n'mn}^{(2)}$ is the overlap integral defined as

$$\begin{aligned} K_{m'n'mn}^{(2)} &= \int_{-\infty}^{\infty} \int_{-\infty}^{\infty} \frac{d_{ijk}}{d_{\text{eff}}} E_i^{(mn)}(x,y,2\omega) E_j^{*(m'n')}(\omega) E_k^{*(m'n')}(\omega) dx dy \\ &= \int_{-\infty}^{\infty} \int_{-\infty}^{\infty} \frac{d_{ijk}}{d_{\text{eff}}} E_i^{*(mn)}(x,y,2\omega) E_j^{(m'n')}(\omega) E_k^{(m'n')}(\omega) dx dy \end{aligned} \quad (3.6)$$

The overlap integral quantifies the possible interaction strengths between the SH and fundamental modes and is crucial to obtaining good conversion efficiencies. This integral means that the fundamental and SH fields must share the same physical space in order for efficient SHG to occur. A similar overlap integral can be formulated for planar waveguide modes integrating over only one spatial variable, leaving the coupled mode equations (3.5) functionally identical for slab and channel waveguides. Without loss of generality we can contract the indexes $\{m,m'\}$ into one, and define a generalized nonlinear coupling strength

κ_{mn} as

$$\kappa_{mn} = -\frac{\omega\varepsilon_0 d_{\text{eff}}}{2} K_{mn}^{(2)} \quad (3.7)$$

and, if an optical field of the form $a(z)=A(z)e^{i\beta z}$ is assumed, we recover the definition of the wavevector mismatch (2.24), except that here we consider effective indices

$$\Delta\beta_{mn}=2\beta_{m,\omega}-\beta_{n,2\omega}=\frac{4\pi}{\lambda}(N_{m,\omega}^{eff}-N_{n,2\omega}^{eff}) \quad (3.8)$$

Once again, the wavevector mismatch appears as a consequence of a mathematical simplification, although it clearly has a fundamental physical meaning. In waveguide SHG, it governs the evolution of the fields along the propagation coordinate but it does not entirely define phase matching in multimode waveguides, even in the case of uniform wavevector mismatch. As we will see, the nonlinear phase shift induced by neighboring modes through cascading effect the phase-matching condition and efficient SHG conversion. With these definitions we can then rewrite the waveguide coupled mode equations (3.5) as

$$\begin{aligned} \frac{dA_{\omega,m}}{dz} &= i \sum_n \kappa_{mn} A_{2\omega,n} A_{\omega,m}^* e^{i\Delta\beta_{mn}z} \\ \frac{dA_{2\omega,n}}{dz} &= i \sum_m \kappa_{mn} A_{\omega,m} A_{\omega,m} e^{i\Delta\beta_{mn}z} \\ &= i \sum_m \kappa_{mn} A_{\omega,m} A_{\omega,m} e^{-i\Delta\beta_{mn}z} \end{aligned} \quad (3.9)$$

These equations represent a finite set of coupled mode equations. They describe the SHG evolution in any structure that sustains modes, namely planar or channel waveguides. It tells us that, in principle, each fundamental field interacts with all the SH fields and vice

versa. The overlap integral eliminates some of the possible interactions, but nothing can be eliminated *a priori* from wavevector mismatch considerations.

The extent to which the summation effectively affects the evolution of the fields cannot be analytically predicted and a numerical analysis needs to be done for each particular case. Furthermore, we will find that a fundamental or SH mode, assumed orthogonal to every other fundamental or SH mode, respectively, can “talk” to an orthogonal mode through the nonlinear interaction.

3.3 Numerical Simulations in the Multimode Domain

Solving the coupled mode equations (3.9) can be a hard task. Instead of finding a general solution, it is better to simplify the problem first to a few interactions and understand the basics of the multimode interaction. For simplicity, first assume that for a given geometry and wavelength the waveguide supports only one fundamental mode. When this fundamental guided mode interacts with two or more harmonic modes, the nonlinear phase shift induced by one harmonic can affect the phase-matching condition for the other harmonic mode detuned from it by many SHG bandwidths. That is, power exchange between one of these SH modes and the fundamental can lead to a nonlinear phase shift for other SH modes.

Beginning with the interaction of one fundamental mode with two second harmonic modes, their interaction is modeled using a simplified version of equation (3.9). These equations are:

$$\begin{aligned}
\frac{dA_\omega}{dz} &= i\kappa_1 A_{2\omega,1} A_\omega^* e^{i\Delta k_1 z} + i\kappa_2 A_{2\omega,2} A_\omega^* e^{i\Delta k_2 z} \\
\frac{dA_{2\omega,1}}{dz} &= i\kappa_1 A_\omega A_\omega^* e^{-i\Delta k_1 z} \\
\frac{dA_{2\omega,2}}{dz} &= i\kappa_2 A_\omega A_\omega^* e^{-i\Delta k_2 z}
\end{aligned} \tag{3.10}$$

where the complex amplitudes of the interacting waves are A_ω for the fundamental and $A_{2\omega,i}$ ($i=1,2$) for the harmonics. This required introducing two more variables than are found in the usual SHG problem that involves a single second harmonic, namely an effective nonlinear coefficient κ_2 describing the "strength" of the interaction of the second mode with the fundamental, (κ_1 is for the first mode), and Δk_2 , the wavevector detuning for the second low power harmonic. Notice the change of variable from β_Ω to \mathbf{k}_Ω . In fact detailed analysis of the equations shows that the difference between the detunings, $\Delta K_0 L = \Delta k_2 L - \Delta k_1 L$, along with $\Delta k_1 L$ (or $\Delta k_2 L$), are the relevant detuning parameters. As will be discussed later, the two SH are eigenmodes of the waveguide, which by definition are orthogonal, and for large depletion they can only interact with each other via the fundamental mode.

This set of equations was evaluated numerically in the nonseeded situation, varying the input fundamental intensity ($I_0 = |A_\omega(z=0)|^2$), the ratio of the interaction strengths (κ_2/κ_1), and the detuning between the harmonic modes, $\Delta K_0 L$. In this calculation, coherent interactions between the SH modes are ignored.

Calculations based on experimental parameters are shown in Figure 3.4. Specifically, a QPM, PE (proton exchange), LiNbO₃ channel waveguide was assumed, 4 μm wide and 3

μm deep. It supports only the TM_{00} fundamental mode around $1.6 \mu\text{m}$. It was designed to optimize the overlap between the fundamental and the TM_{01} SH field using the first order of the grating. This also resulted in a small effective index difference between the TM_{01} and TM_{20} modes, with a larger overlap integral for the SHG of $\text{TM}_{01}(2\omega)$ than for $\text{TM}_{20}(2\omega)$. A reasonable approximation for our waveguide is $\Delta K_0 L \sim 2\pi$ and $\kappa_1 L = 4$ and $\kappa_2 L = 1.5$, based on a calculated effective index difference of 0.0001 and on overlap integrals with triangular domain inversion regions [42].

A series of SHG detuning curves is shown in the left side of Figure 3.4 for different input fundamental powers. In Figure 3.4(a), the SHG output is essentially a linear superposition of the response curves for the two second harmonic modes acting independently. As the normalized input power is increased, the response becomes much more complicated. There is no single well-defined peak for zero detuning of the TM_{01} mode and the largest conversion efficiency shifts to a non-zero detuning. In fact, if the fundamental wavelength is fixed, increasing the input power would lead to oscillations in the second harmonic. This implies that optimizing the peak conversion efficiency requires power-dependent retuning of the input laser wavelength.

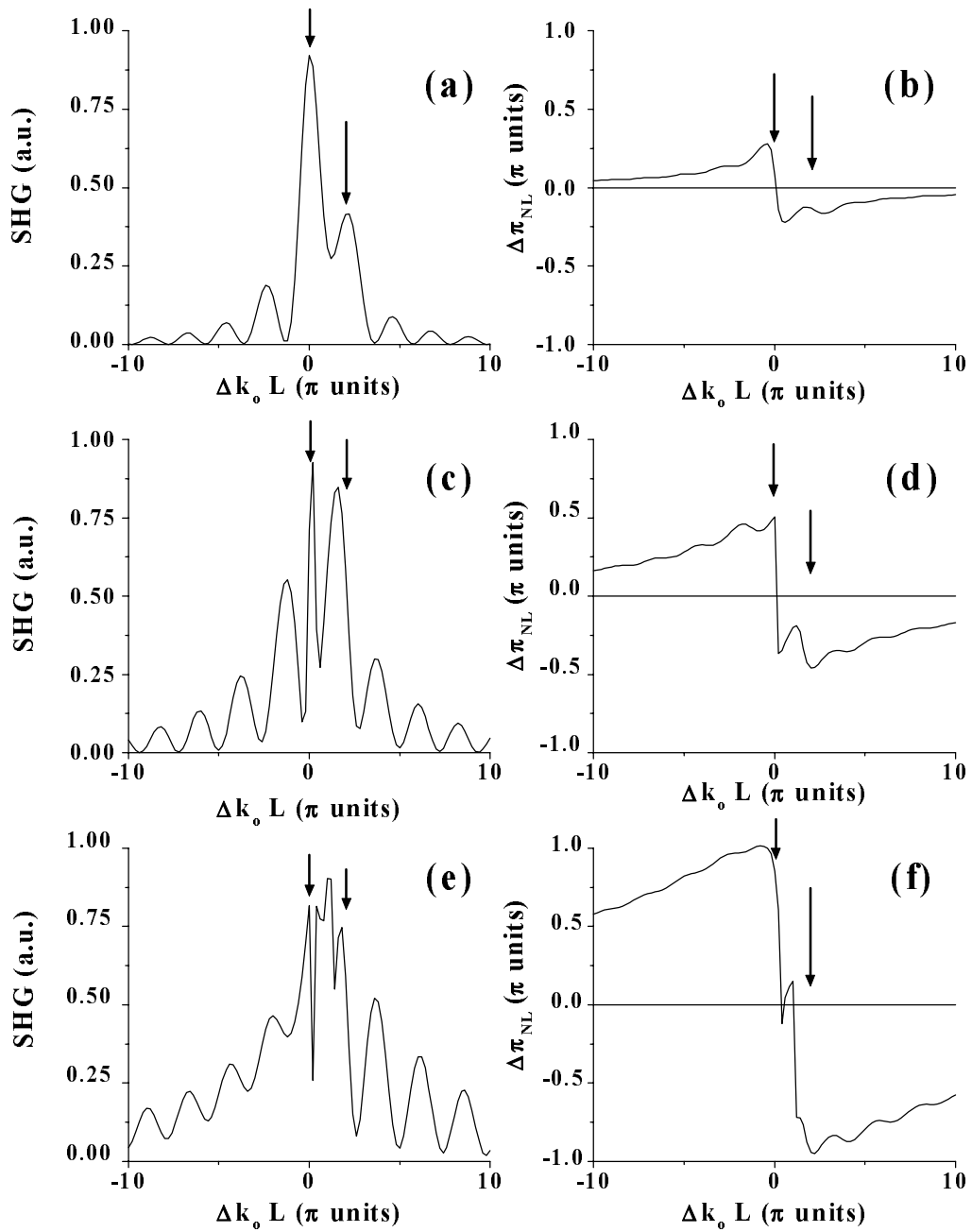


Figure 3.4 (a,c,e) SHG detuning curve and (b,d,f) total nonlinear phase shift for different input powers. (a,b) $I_0 = 0.25$, (c,d) $I_0 = 1.0$, and (e,f) $I_0 = 2.25$. In all cases $\kappa_1 L = 4$, $\kappa_2 L = 4$, and $\Delta K_0 L = 2\pi$. The arrows show phasematching position for each independent mode interaction.

The total nonlinear phase shift imparted onto the fundamental is shown on the right side of Figure 3.4. The shift in the zero nonlinear phase shift point clearly moves toward positive detuning. Furthermore, note that for large input powers, Figure 3.4(f), zero net nonlinear phase-shift occurs for multiple detunings implying a series of peaks in the conversion efficiency corresponding to different wavelengths.

This behavior can be understood in terms of the cascaded nonlinearity which produces nonlinear phase shifts in the fundamental due to the different harmonics. Maximum SHG occurs for a harmonic beam when the photons returning from the harmonic via down-conversion back to the fundamental are π out of phase with the fundamental. This ensures maximum depletion of the fundamental. However, when another second harmonic mode interacts with the same fundamental, it produces a cascaded nonlinear phase shift on the fundamental, for example $+\phi_{2,NL}$. As a result the phase-match down-shifted photons are now out of the π -phase shift condition with the fundamental.

The individual nonlinear phase shifts imposed onto the fundamental, ignoring the presence of the neighboring mode, are shown in Figure 3.5. For low conversion efficiencies, the nonlinear phase shift due to a second mode is negligible, as seen in Figure 3.5a. In the high conversion picture, the phase shift imposed by the interaction with neighboring modes is no longer small and imposes a sizable phase shift $+\phi_{2,NL}$ (Figure 3.5(b)). By detuning from the low-power wavevector matching condition, represented by the arrows in Figure 3.5, maximum conversion of the harmonic can again be obtained. As a result, the wavelength for maximum conversion changes. Actually, the interaction forces the phasematched positions

to get closer to each other, as pictured in Figure 3.5(d). This basic explanation can be extended to more complicated interactions.

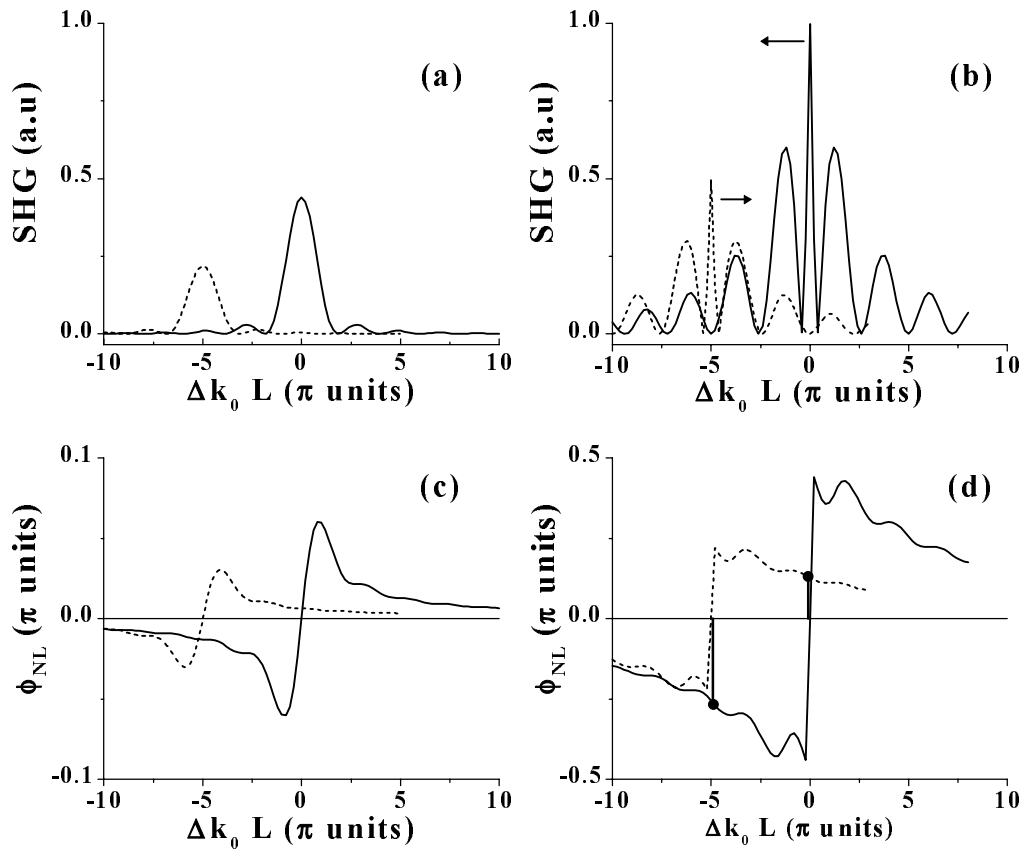


Figure 3.5 (a,b) SHG detuning curve and (c,d) nonlinear phase shift for two independent mode interactions. Low power interaction are shown on the left hand side, and high power interaction are shown on the right hand side. Notice the nonzero phase shift from one interaction in the phasematching condition for the other.

Using the previous discussion, we can redefine the phasematching condition for waveguide SHG as the position for maximum conversion, in terms of the nonlinear phase shift

imposed by additional interactions. Consider the wavevector mismatch for a particular interaction between a fundamental and a second harmonic mode given by $\Delta k_o L$. Including the nonlinear phase shift imposed by neighboring modes, the nonlinear phase shift of the photons coming back from the second harmonic is

$$\Delta\phi_{total} = \pi - \Delta k_o L - \Delta\phi_{NL, othermodes}$$

Maximum conversion, i.e., phasematching, is obtained when the photons coming back into the fundamental are π out of phase with the fundamental. Therefore the condition for phase matching is no longer when $\Delta k_o = 0$, but is now given by

$$\Delta k_o = - \left[\frac{\Delta\phi_{NL, othermodes}}{L} \right]$$

The nonlinear phase shift imposed by neighboring modes is intensity dependent. Therefore the position for phasematching is also intensity dependent. For large conversion efficiencies and closely spaced modes, experimentally and theoretically it has been found that the second harmonic generation process can be severely distorted by these nonlinear phase changes [34]. A direct consequence of this intensity dependent mode competition is that the conditions for phase matching are different in the low and high depletion regimes. Normally a waveguide device is aligned at low power to avoid possible damage, therefore it is optimized in the low depletion regime. When subsequently the power is increased to obtain efficient SHG, the displacement of the phasematching condition may lead to SHG growth

different from the ‘typical’ SHG behavior. To achieve the most efficient SHG, a small adjustment in some of the tuning parameters (wavelength, temperature, ...) is required.

3.4 Experimental Setup

The same basic experimental setup was used for all of the experiments performed as part of this thesis work. The laser source used was a NaCl:OH⁻ (F²⁺:O²⁻) color center laser (Burleigh FC-120) synchronously pumped by a Nd:YAG laser (Coherent Antares). By varying the cavity length, this laser operates either in a mode-lock configuration, producing 6 to 9 picosecond pulses at 76 MHz (assuming a sech² pulse shape) tunable from 1480 to 1665 nm, or by destroying the mode-lock conditions in a Quasi-CW (QCW) configuration tunable over the same range. Both the laser and the components described below, were mounted on the same pneumatically isolated optical table to assure stable performance. The color center (CCL) performance was monitored in real time using a scanning Fabry-Perot etalon (Burleigh TL series).

In the pulsed regime, the pulse duration was monitored with a SHG autocorrelator (Femtochrome FR-103). A 3 meter computer controlled spectrometer was used (Instrument System, SPECTRO 320) as a wavemeter and to assure correct operation of the laser. To prevent feedback into the CCL and to eliminate the residual pump from the Nd:YAG laser, a combination of a Faraday isolator and a high pass filter (LP 1200) were used at the output of the color center laser. A combination of a half-wave plate at 1550 nm and a polarizing cube beam splitter (PBS) was used both to select the desired polarization and as a variable beam splitter.

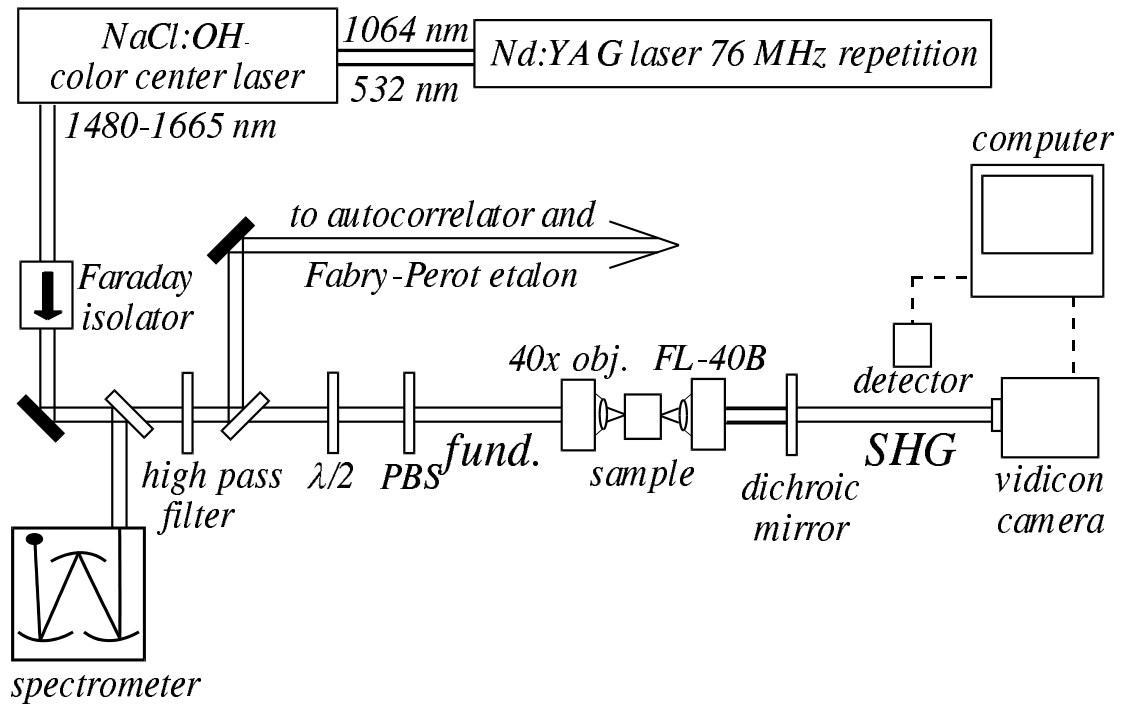


Figure 3.6 Experimental setup used to characterize $\chi^{(2)}$ waveguides.

The light was coupled into and out of the waveguides by end fire coupling. The coupling setup used consisted of a pair of solid micropositioners with three degrees of freedom, to accommodate at the input a 40X microscope objective with individual surfaces AR coated at 1550 nm, and at the output an aspheric 40X microscope lens (Newport FL-40B). The combination of these lenses had a throughput of 96% at the fundamental wavelengths and 85% at the second harmonic wavelengths. The samples were placed on a piezoelectric controlled fiber positioner (Physic Instrument F-103) with 5 degrees of freedom,

three of which can be piezoelectric controlled at a time with a 50 nm precision. The fundamental power was monitored with a thermal detector (Coherent 210) or a point calibrated germanium detector (UDT 371 with integration sphere). The second harmonic power was monitored with silicon detectors (Silicon detector Coherent 212 for small signal readings or a calibrated Coherent Field Master silicon head).

The second harmonic output collected at the end of the waveguides as a function of wavelength, or detuning curve, constitutes the basic tool used to study the evolution of the SHG. These scans are done using lock-in detection with the small signal silicon detector, with appropriate filters to block higher order harmonics generated in the waveguide [43]. The wavelength was evaluated with a computer controlled spectrum analyzer with 0.1 nm accuracy, and a resolution of 0.28 nm. Everything was controlled using standard GPIB protocols and stored in a PC computer. To evaluate the mode profile at the output of the waveguides, the near field of the end facet of the waveguide was imaged into a camera (Hamamatsu, extended germanium Ge-PbS vidicon). The images captured were stored in a computer using a frame grabber (Image Translation). Gamma correction was taken into account to correct for geometrical distortion.

3.5 Experimental Measurements

Experiments to confirm the intensity dependent multimode competition have been performed in a QPM-PE LiNbO₃ channel waveguide made using standard proton exchange techniques [44], supplied by the University of Nice, France. This waveguide is 1 cm long. It

has 13 groups of 7 waveguides each, 4 of which have a 20 μm domain reversal period suitable for phase-matching around 1600 nm. The waveguides used had an effective depth of 3 μm and channel widths varying from 1 to 7 μm . They were designed to optimize the overlap between the TM_{00} fundamental mode and the TM_{01} SH mode fields around 1600 nm. Linear losses at 1600 nm are ≈ 0.4 dB/cm and at 800 nm less than 0.9 dB/cm. The total throughput, including coupling efficiency, was typically around $\approx 50\%$. Calculations using material parameters (GVD and refractive indices) and the pulse width from the laser gave a temporal walk-off length, L_w , of 2.4 cm. Therefore the long pulse approximation, as discussed previously, can be used.

The change in refractive index due to the proton exchange technique increases the extraordinary refractive index, and decreases the ordinary refractive index. Therefore only TM modes can be guided by these waveguides. Normally titanium in-diffusion is the technique used to create the waveguides in ferroelectric materials, allowing both TE and TM modes to propagate. This can further complicate the situation, i.e. when cross talk between polarizations can occur.

Wavelength scans around the ($\text{TM}_{00}(\omega) \rightarrow \text{TM}_{01}(2\omega) + \text{TM}_{20}(2\omega)$) interaction are shown in Figure 3.7 for a 4 μm wide channel waveguide. The generation of both SH modes was confirmed by observing the spatial power distribution at the output under different input conditions, as shown in Figure 3.8. Using the color center laser in its QCW (quasi-CW) configuration, at low conversion efficiencies (less than 1%) the wavelength detuning curves are similar to the calculated ones (Figure 3.4(a)).

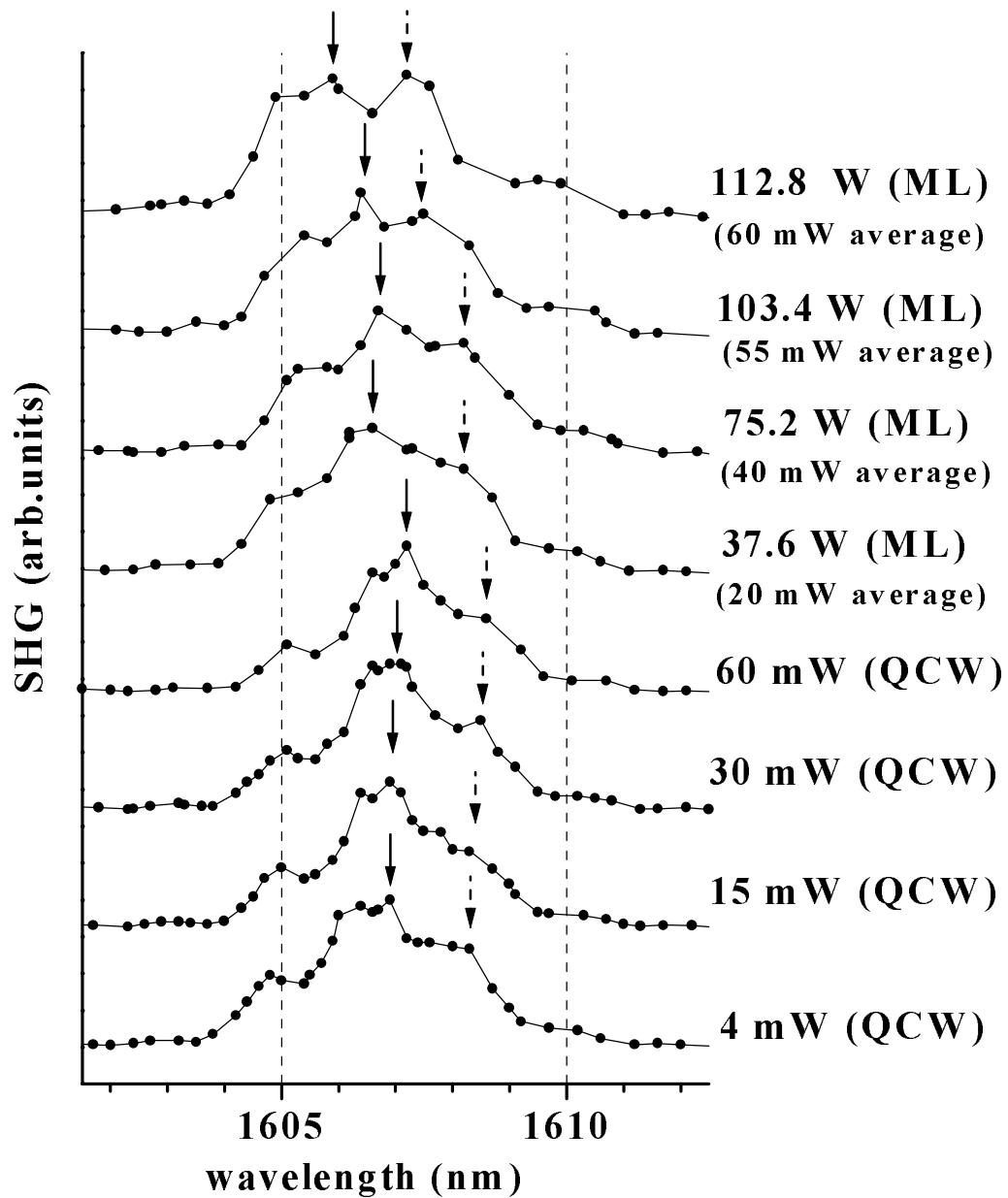


Figure 3.7 Wavelength scans in a LiNbO₃ QPM 4 μm width waveguide at different peak power in the vicinity of the $TM_{00}(\omega) \rightarrow TM_{01}(2\omega) + TM_{20}(2\omega)$. Solid (dotted) arrows track the position of the peak conversion to the $TM_{01}(2\omega)$ ($TM_{20}(2\omega)$) mode.

Note that for comparable average powers in both QCW and mode-locked operation, the detuning curves are very different, indicating that thermal effects are not responsible for the observed changes. As expected, increasing the peak input power increases the SHG efficiency. The effective conversion efficiencies at the solid arrows for the cases shown in Figure 3.7 are (bottom to top): 0.005%, 0.69%, 0.33%, 0.63%, 17%, 21%, 23%, and 27%, respectively. The solid and dotted arrows track the positions of the maximum conversion and the clearest mode profiles are observed for the $TM_{01}(2\omega)$ and $TM_{20}(2\omega)$ modes (Figure 3.8), respectively. At large conversion efficiencies (more than 10%: ML) the maxima shift position, come closer to each other and compete for the maximum SHG efficiency. This type of behavior is quite general and was observed for different waveguides at different wavelengths, independent of the coupling strength ratio κ_2/κ_1 . These results are all in qualitative agreement with the theory and numerical results discussed above.

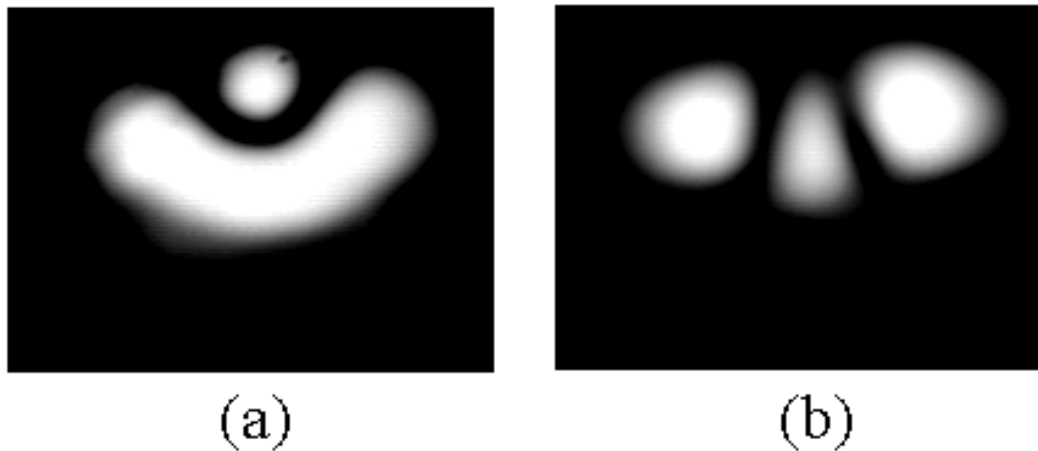


Figure 3.8 (a) $TM_{01}(2\omega)$ and (b) $TM_{20}(2\omega)$ mode profiles correspondent to Figure 3.7.

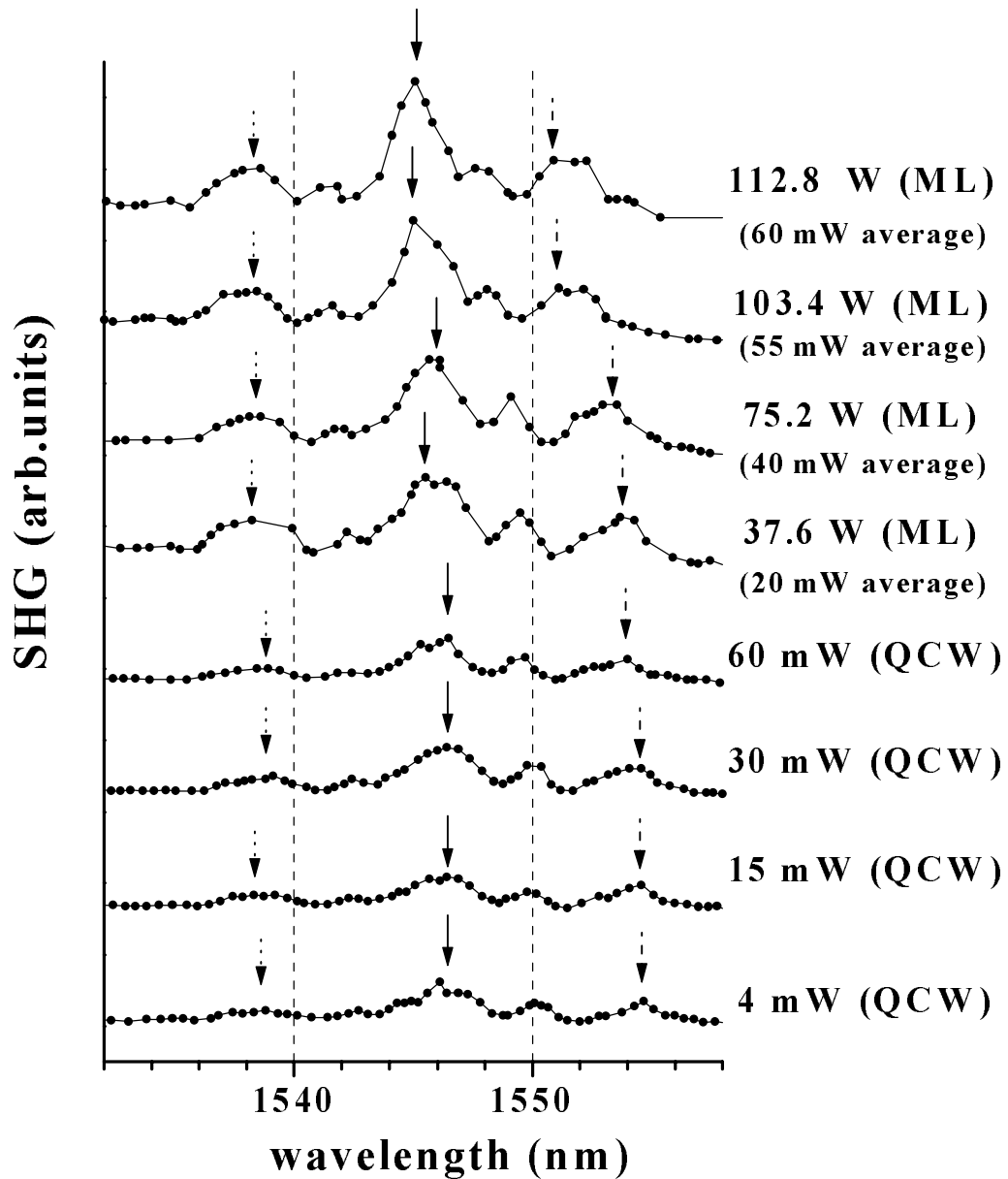


Figure 3.9 Wavelength scans in a LiNbO₃ QPM 4 μm width waveguide at different peak power in the vicinity of the interaction $TM_{00}(\omega) - TM_{02}(2\omega) + TM_{40}(2\omega) + TM_{21}(2\omega)$. These curves were normalized to the solid arrow points in Figure 3.8. Solid (dotted and dashed) arrows track the position of the peak conversion to the $TM_{02}(2\omega)$ ($TM_{40}(2\omega)$ and $TM_{21}(2\omega)$) mode.

In the same 4 μm wide channel waveguide, the second harmonic modes are all closely spaced for the interaction $\text{TM}_{00}(\omega) \rightarrow \text{TM}_{02}(2\omega) + \text{TM}_{40}(2\omega) + \text{TM}_{21}(2\omega)$. The observed spatial mode profile distribution of the SHG verified the presence of all of these modes. The evolution of the SHG with increasing input power is very complicated, as shown in Figure 3.9. The corresponding modes are shown in Figure 3.10. The behavior shown in this figure indicates a complex SHG evolution. It requires 4 coupled mode equations in the theoretical analysis, describing 3 independent second harmonic modes and one fundamental mode. This system is complicated, but could be solved for specific cases numerically.

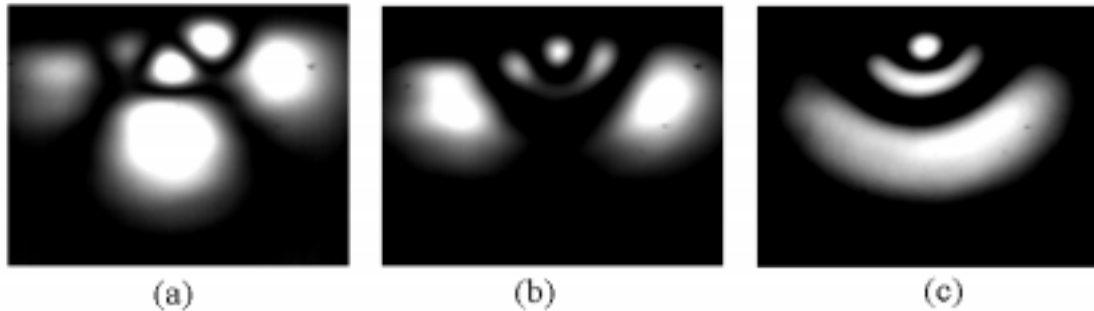


Figure 3.10(a) $\text{TM}_{21}(2\omega)$, (b) $\text{TM}_{40}(2\omega)$, and (c) $\text{TM}_{02}(2\omega)$ mode profiles for Figure 3.9.

Experimentally there were even more complex situations. In the same LiNbO_3 device, on the 7 μm wide waveguide we encountered the interaction between $\text{TM}_{00}(\omega) + \text{TM}_{10}(\omega) \rightarrow \text{TM}_{22}(2\omega) + \text{TM}_{11}(2\omega) + \text{TM}_{01}(2\omega) + \text{TM}_{30}(2\omega) + \text{TM}_{40}(2\omega)$. This system requires a set of 10 coupled mode equations to be solved. The low depletion detuning curve with a binary representation of the modes involved is shown in Figure 3.11. Here a shift of 4.5 nm in the position of maximum conversion efficiency was observed between low and high powers. It corresponds to twice the FWHM bandwidth of the most prominent peak in the figure.

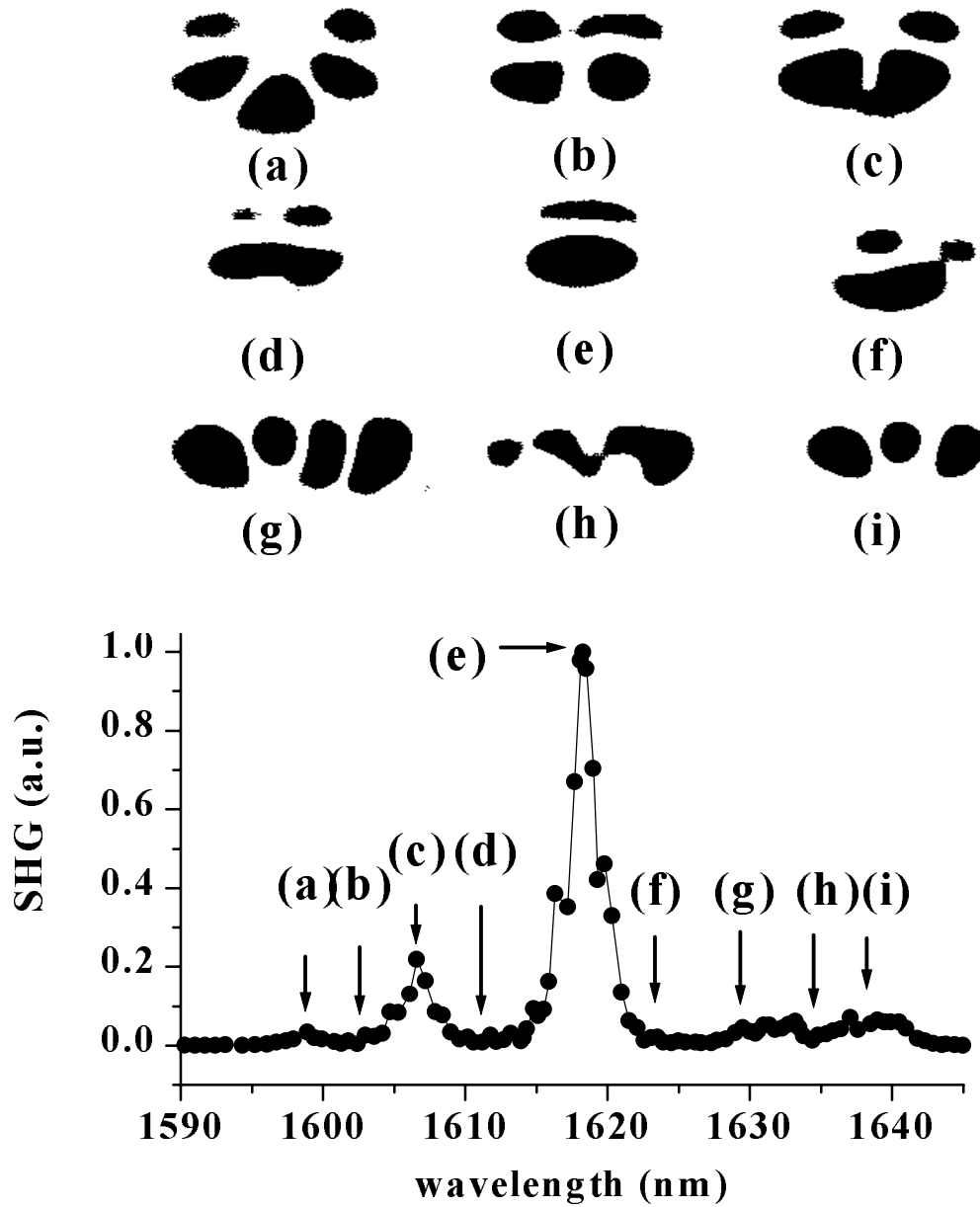


Figure 3.11 Low depletion detuning SHG curve in the vicinity of the interaction between TM_{00} and TM_{10} fundamental modes and (a) TM_{22} , (c) TM_{11} , (e) TM_{01} , (g) TM_{30} , and (i) TM_{40} second harmonic modes. Modes in (b), (d), (f) and (h) represent mixed modes. The inset show a binary representation of the mode profiles at the position shown by the arrows.

In the low depletion regime the intensity dependent multimode competition is negligible. But at high depletion, the effect of neighboring modes can be very complex. The complexity increases dramatically with the inclusion of only a few modes. Due to the small refractive index differences produced by this waveguide fabrication technique, we may find in general that harmonic guided modes can be very closed spaced in the wavevector space. Numerical simulations are required to predict the performance at high depletion.

Although the analysis and the experimental observation were done for second harmonic generation, it can be generalized to other second order processes wherever coherent interactions take place. And as we will see next, in some cases these processes are intermixed.

3.6 Higher Harmonic Generation

Second order processes are used for many applications other than SHG. Optical parametric oscillation was observed not longer after the first observation of SHG [45], and later, difference frequency generation for applications in the mid-infrared [46]. Ferroelectric QPM devices are used due to their flexibility for achieving QPM in either bulk or waveguide geometries. All these devices are optimized for a given combination of the three-wave parametric interaction involved in second order processes. Yet in these QPM devices additional phasematching processes are happening simultaneously. These other processes are not efficient, but they are present and sometimes they disturb the expected performance.

In the QPM-PE LiNbO₃ sample studied to observe the multimode competition, some of these additional processes were observed. The device was designed to optimize the overlap between the TM₀₀ fundamental mode and the TM₀₁ SH mode field around 1.6 μm, using the first order of the QPM grating. However, additional simultaneous phasematching processes were observed using higher orders of the grating [43]. This kind of effect has been also reported in KTP segmented waveguides [47].

The observations discussed now were performed under conditions that showed the best fourth-harmonic conversion efficiency. It was achieved in a 6 μm wide waveguide in the QPM-PE LiNbO₃ described earlier, at a fundamental wavelength of 1619.4 nm, with the color center laser operating mode-locked. The average output in the fundamental, second, third and fourth harmonics was 71 mW, 29 mW, 55 μW and 66 μW, respectively, for a 220 mW average fundamental power incident on the input coupling objective, i.e., we were operating well within the high depletion regime. In this experiment, although the power of the third and fourth harmonics was much lower than the second harmonic, the guided output appeared distinctly white because of the low response of the eye at 809.7 nm. Figure 3.12 shows the output spectrum taken with the computer controlled spectrum analyzer, clearly showing the generated harmonics. Appropriate filters were used to verify that the measured spectral lines were not diffraction orders of the fundamental. Since the third and fourth-harmonics are directly dependent on the second harmonic power, these occur at similar pump wavelengths for the three interactions. The maximum of the fourth harmonic is not obtained at the maximum of the second-harmonic generation efficiency owing to different overlap between different modes.

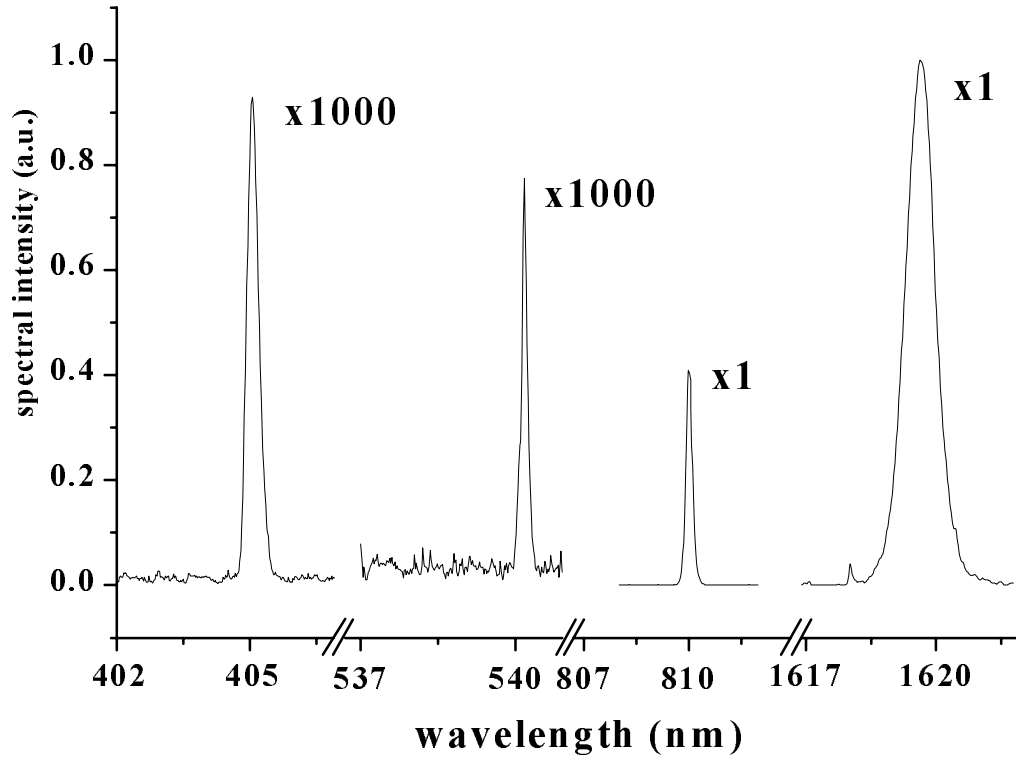


Figure 3.12 Spectral scan of generated harmonics of 1619.4 nm color center laser source in a 6 μm mask width QPM PE LiNbO₃ channel waveguide with 20 μm domain inversion period.

Using the vidicon camera, the different modes involved in the interaction were identified. These modes were $\text{TM}_{00}(\omega)$, $\text{TM}_{20}(2\omega)$, $\text{TM}_{20}(3\omega)$ and $\text{TM}_{01}(3\omega)$, and $\text{TM}_{41}(4\omega)$. The phasematching wavelengths for various interactions were obtained with the aid of a numerical simulation used to calculate the effective indices [48]. This identifies phase-matching with different grating orders as follows: for the second harmonic $m = 1$ from 1619.4 nm to 809.7 nm; for the third harmonic $m = 3$ through difference frequency generation between 1619.4 nm and 809.7 nm; and for the fourth harmonic as $m = 7$ from 809.7 nm to

404.9 nm. Even in the low depletion regime, where just a fraction of a percentage of the light is converted to the SH, some traces of green light were observed with the naked eye in all the waveguides in this device. The generation of green light was possible to see because of the advantageous response of the eye at wavelengths around 500 nm, but not large enough to be measured using some recording device.

During the evolution of the work reported here, some other devices were tested using the same experimental setup. In all the QPM waveguides tested, some traces of sum frequency generation was observed, both in inorganic and organic materials. These observations are not reported here in detail due to the photoinduced damage caused by the higher harmonics. For ferroelectric materials, operating in the mode-locked regime of the laser, where large conversion is expected, in some cases there was a large amount of photorefractive damage due to the higher harmonic generation because of some impurities. This changed in a short time the phasematching conditions. In the QPM-PE LiNbO₃ sample described earlier, no photorefractive damage was observed at any time. For polymer devices these high harmonic process should be present, and therefore contributed to the photobleaching degradation of the waveguides. Unfortunately, to the best of my knowledge, no report has been done concerning higher harmonic generation in QPM structures in polymers.

The existence of these effects in QPM SHG devices is another manifestation of the intricate combination of processes present in waveguide SHG. These were only highlighted in this work, but they certainly warrant further study.

3.7 Limits of Influence of the Multimode Competition

For one fundamental mode interacting with two second harmonic modes, the numerical calculations predict that for different ratios of the interaction strengths, κ_2/κ_1 , the effective SHG detuning curves for low fundamental depletion (less than 10% conversion efficiency) or large separation ($\Delta K_0 L$ larger than 25π) always behaved independently for the two second harmonic modes. In the case of larger depletion and/or closer separation, the two second harmonic modes "talk" to each other via the fundamental mode. Some general features that we found are that the wavelength and peak conversion efficiency for the two different harmonic modes change with input fundamental intensity and that power-dependent competition occurs between them at high powers. Additional study is required for mode interaction involving more than three modes. The phase-space of the interaction becomes complicated fast. Overall the system of coupled mode equations (3.9) needs to be considered. The dynamics of this system is likely to exhibit a chaotic behavior. Although the analysis and the experimental observation were done for SHG, it can be generalized to other second order processes.

In summary, second harmonic generation can be a very complex process when multiple, closely spaced harmonic mode interactions are possible. Competition for power occurs due to the common coupling to the fundamental beam and the peak efficiency wavelength shifts due to the nonlinear phase shifts introduced by the neighboring mode. This effect has been predicted numerically and verified experimentally in QPM LiNbO₃ waveguides.

CHAPTER 4

SECOND HARMONIC GENERATION SPATIAL NONRECIPROCITY

“ Just look along the road, and tell me if you can see either of them ” said the King.

“ I see nobody on the road ” said Alice.

“ I only wish I had such eyes, ” the King remarked in a fretful tone. “ To be able to see Nobody! And at that distance too! Why, it’s as much as I can do to see real people, by this light! ”

Through the looking Glass
Lewis Carroll

It is widely accepted that optical interactions in dielectric optics are reversible in space. This means that the result of an interaction is independent of the propagation direction, i.e., the interactions are spatially reciprocal. This is completely true in linear optics, and the idea can usually be generalized to nonlinear optics. Some work has been done to explore this statement carefully [49].

Both the conversion efficiency and the nonlinear phase shift are important in SHG which raises questions about the consequences of these properties. One of the most important signatures of SHG is that it depends on the spatial distribution of the wavevector (or phase) mismatch $\Delta k(z)$ ($\Delta k(z)L$). The evolution of the nonlinear process at a given point along the path depends on the incident (seeded) complex fundamental and complex second harmonic

fields generated by the interaction up to that point, the local wavevector mismatch, and the local nonlinear coupling strength. If there is a spatial variation in the wavevector mismatch, there is not a unique phase matching condition along the propagation path and the second harmonic undergoes a complicated evolution. For example, if there is a temperature gradient along propagation path, for example present in temperature tuned phasematching in channel waveguides, it can lead to a large phase-shift and small depletion of the fundamental [13]. A particular case of a nonuniform wavevector distribution is one which is spatially nonsymmetric, a case which has been shown to result in an output SHG that is spatially nonreciprocal [50].

This particular train of thought was motivated by the observation of break-up in the detuning curve when characterizing the sample discussed in the previous chapter. For a 2 μm deep by 3 μm wide waveguide, the interaction $\text{TM}_{00}(\omega) \rightarrow \text{TM}_{00}(2\omega)$ showed a break-up of the main SHG peak in the detuning curve (Figure 4.1). What was most amazing is that the response was different depending on which input facet was used to end fire couple the fundamental into the waveguide (labeled as input A or input B, arbitrarily). Furthermore, the break-up in the detuning curve only occurred for this particular interaction, and not for the other phase matched modes present in the waveguide (in Figure 4.1 the $\text{TM}_{00}(\omega) \rightarrow \text{TM}_{20}(2\omega)$ and $\text{TM}_{00}(\omega) \rightarrow \text{TM}_{01}(2\omega)$ are also present). The analysis of this discrepancy led to the identification of spatial nonreciprocity in SHG. After this detailed analysis which is presented next, it was concluded that the break up was due to some localized imperfection in the LiNbO_3 or in the waveguide fabrication which produced a variation in the effective indices, creating a nonuniform-nonsymmetrical wavevector distribution.

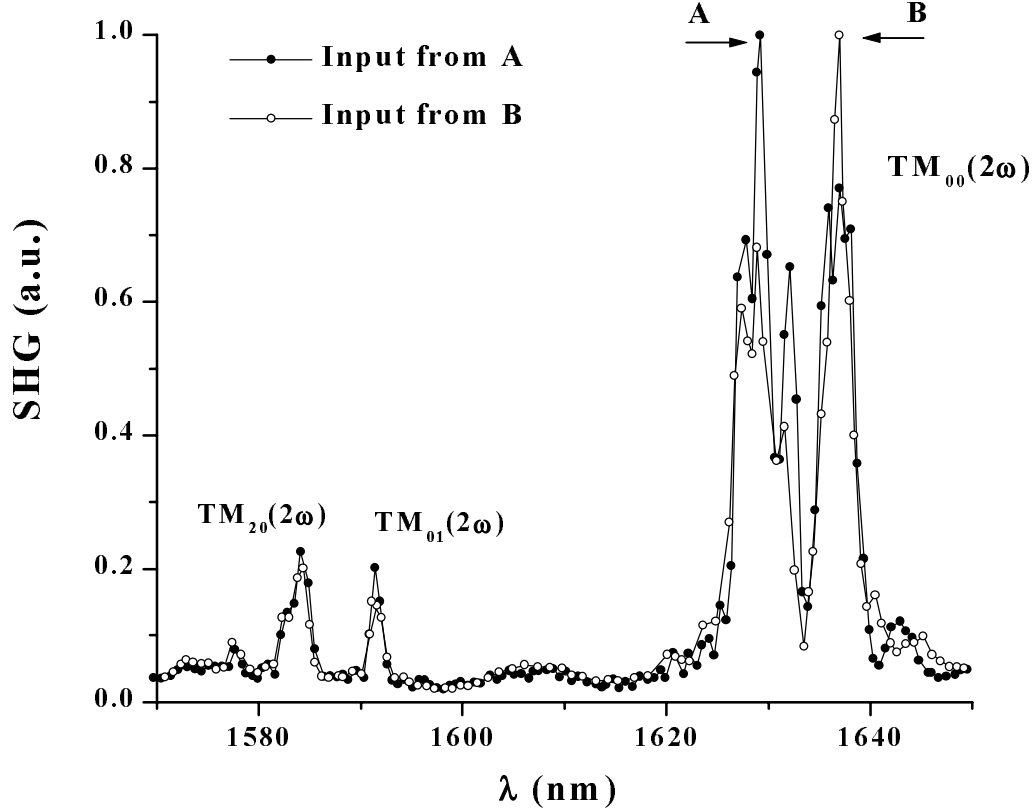


Figure 4.1 SHG detuning curve in a 3 μm by 2 μm waveguide PE-QPM LiNbO_3 . Notice the break up in the $\text{TM}_{00}(\omega) \rightarrow \text{TM}_{00}(2\omega)$ resonance. The magnitude of the maximum conversion depends in the propagation direction (in coupling at end A or end B).

In this chapter an intuitive explanation of spatial nonreciprocity will first be discussed. The equations governing second harmonic generation in the presence of a nonuniform distribution in the wavevector mismatch, or in the nonlinear coupling strength, will be discussed. Additionally a simple asymmetric profile consisting of a discontinuity along the propagation path will be analyzed in detail in order to understand the basic parameters involved in spatial nonreciprocity. Some controlled experiments to show this effect are presented.

4.1 Intuitive Explanation for Spatial Nonreciprocity in SHG

Second harmonic generation is a coherent process, and therefore the relative phase between the fundamental and the second harmonic plays a key role. In SHG, and in particular for the cascaded nonlinearity which generates the nonlinear phase shift, the fundamental and SH fields require some joint propagation to occur (i.e., it is a "non-local" process).

In the case of a spatially uniform wavevector distribution, at phase matching the fundamental and the second harmonic keep a constant phase difference and the outcome is a net transfer of energy. However, if there is a spatial variation in the wavevector mismatch there is not a unique phase matching condition along the propagation path and the second harmonic undergoes a more complicated evolution. The same complex behavior occurs if there is a variation in the nonlinear coupling strength of the fundamental to the harmonic.

As depicted in Figure 4.2, the second harmonic and fundamental amplitude and phase which are generated at every point ($\mathbf{e}'(\omega)$, $\mathbf{e}'(2\omega)$) depend on the local wavevector mismatch ($\Delta\mathbf{k}_{\text{loc}}$), the complex amplitude of the fundamental beam transmitted to that point ($\mathbf{e}(\omega)$), the complex SH amplitude generated up to that point ($\mathbf{e}(2\omega)$) and the local nonlinear coupling strength (κ_{loc}). The second harmonic and fundamental ($\mathbf{E}'(\omega)$, $\mathbf{E}'(2\omega)$) fields output from the device will depend not only on the input fundamental beam ($\mathbf{E}(\omega)$) and input wavevector mismatch, but also on the details of the spatial distribution of the wavevector mismatch and the nonlinear coupling strength. Furthermore, if the spatial distribution over which SHG takes place is symmetric with respect to the middle of the propagation length, the fields propagating in opposite directions in a spatially nonuniform structure will undergo similar changes.

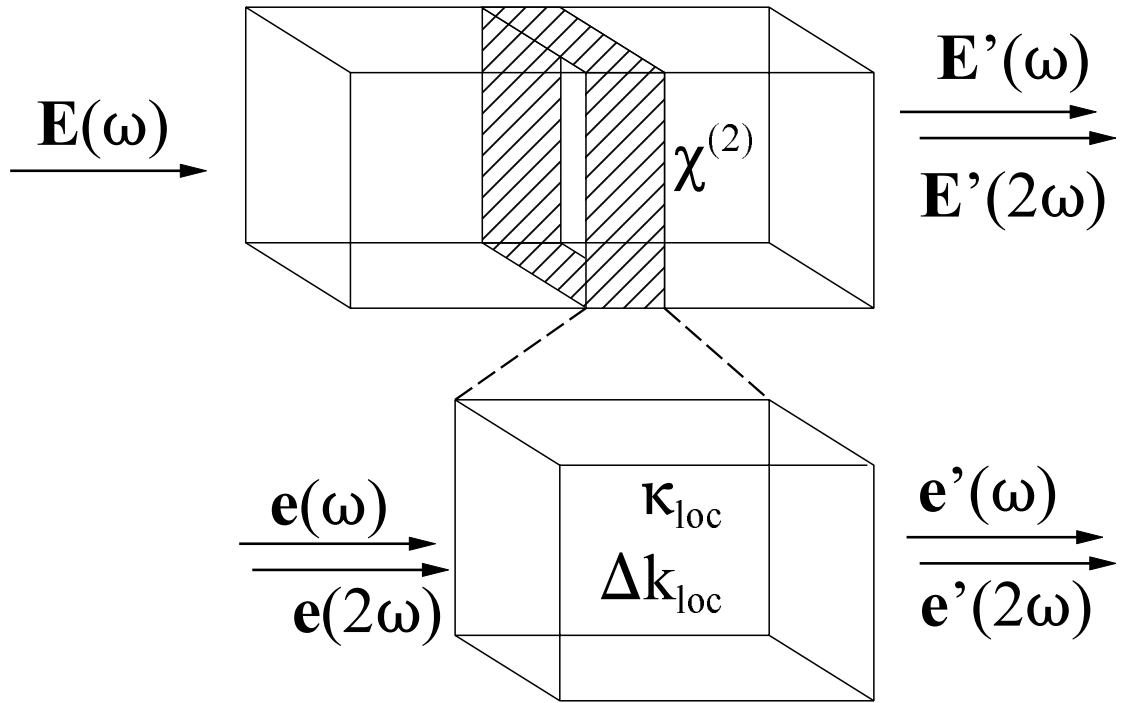


Figure 4.2 Local spatial second harmonic generation representation.

For the symmetric geometry shown in Figure 4.3 after propagating a distance \mathbf{X} , the fields' evolution has been the same. Therefore, the outcome will be the same independent of the propagation direction, thus spatially reciprocal. In contrast to this, if the propagation occurs in a nonsymmetric structure, in general the fields launched from either direction may not be the same at the output due to differences in the evolution of the process after propagating the same distance \mathbf{X} . Therefore, in general, for a nonsymmetrical structure the SHG output depends on the direction into which the fundamental is launched and therefore is spatially nonreciprocal.

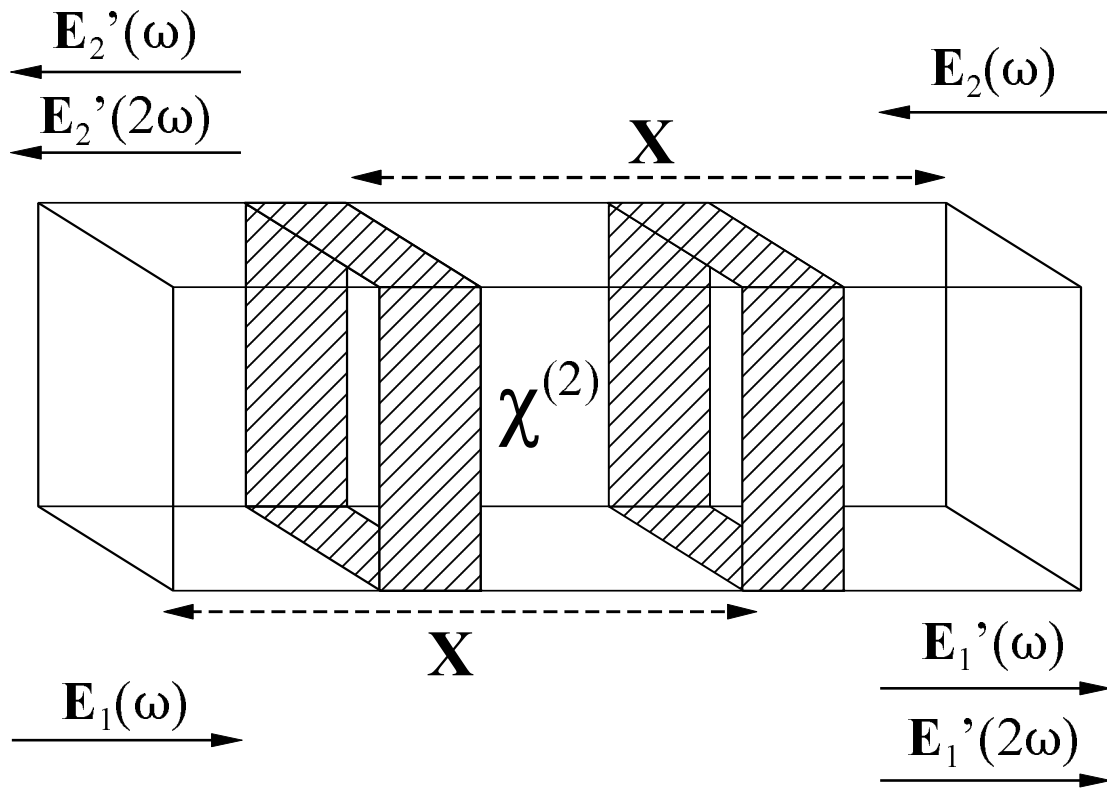


Figure 4.3 Directional response in symmetric and asymmetric structures. For symmetric structures the outcome will be the same ($E_1'(\omega, 2\omega) = E_2'(\omega, 2\omega)$) in both directions. For nonsymmetrical structures, in general, it may not be the same ($E_1'(\omega, 2\omega) \neq E_2'(\omega, 2\omega)$).

Notice that we can have a nonuniform distribution of the wavevector mismatch and the nonlinear strength and still have a symmetric structure. In the same way, we can have a structure that is made of more than one nonlinear medium within what we define as the device length. Nonreciprocity is a particular case of a more general type of interaction, characteristic of nonuniform, asymmetric profiles. A general description of nonuniform profiles will be discussed in chapter five.

4.2 Coupled Mode Equations for Nonuniform profiles

In order to study the evolution of SHG in a nonuniform structure, a closer look into the coupled mode equations (2.27) is required. Nonuniform and nonsymmetrical structures for SHG have been studied before [7, 30, 51, 52]. These authors pointed out the advantages of having a nonuniform spatial distribution in producing larger SHG bandwidth, but their results only dealt with one way propagation. A closer look at these studies reveals a variety of theoretical approaches. All are based on coupled mode theory including a spatially varying nonuniform wavevector mismatch. The variations are often included in the coupled mode equation by replacing the wavevector mismatch, ΔkL , by a spatially varying wavevector mismatch, $\Delta k(z)L$. This approach is completely wrong under the SVEA.

A careful analysis of this particular case under the SVEA shows the existence of additional terms which have to be included in the SHG coupled mode equations. Taking into account that the wavevectors have a propagation coordinate dependance: $k_\omega(z) = k_{0,\omega} + \delta k_\omega(z)$ and $k_{2\omega}(z) = k_{0,2\omega} + \delta k_{2\omega}(z)$ where $k_{0,(2)\omega}$ is the average wavevector at the frequency $(2)\omega$ and the $\delta k_{(2)\omega}(z)$ describe the z -dependent variations around it [41]. Assuming that the electric field is related to the reduced field as in (2.31): $E_\Omega(z) = (2I_0/n_\Omega c \epsilon_0)^{1/2} A_\Omega^{(i)}(z)$ ($\Omega = \{\omega, 2\omega\}$), the lossless coupled mode equations for the electric fields, labeled as type I, are:

$$\begin{aligned} \frac{dA_\omega^{(i)}(z)}{dz} + i [k_{o,\omega} + \delta k_\omega(z)] A_\omega^{(i)}(z) &= -i\kappa(z) A_{2\omega}^{(i)}(z) \left(A_\omega^{(i)}(z) \right)^* \\ \frac{dA_{2\omega}^{(i)}(z)}{dz} + i [k_{o,2\omega} + \delta k_{2\omega}(z)] A_{2\omega}^{(i)}(z) &= -i\kappa(z) \left(A_\omega^{(i)}(z) \right)^2 \end{aligned} \quad (4.1)$$

The selection of the reduced fields will be evident in short. Notice that we also allow a spatially nonuniform nonlinear coupling strength ($\kappa(z) = \omega d_{\text{eff}}(z)/[2A_{\text{eff}}(z)n_{2\omega}n_{\omega}^2c^3\epsilon_0]^{-1/2}$) through changes in the effective area ($A_{\text{eff}}(z)$) in the case of a waveguide geometry (or by using different crystals in a bulk medium geometry [$d_{\text{eff}}(z)$]). To solve these coupled mode equations we need to specify the spatial dependence of the wavevector mismatch as well as the input electric fundamental and second harmonic fields. In general the solution may not be analytical and numerical methods, as discussed in the previous chapters, need to be used. Using this representation, the phase of the electric field oscillates on a wavelength scale, and therefore its rotation is extremely fast. With this approach the numerical calculation is either inaccurate or requires extended computational time. To simplify the numerical analysis one can assume the form of the electric field. Using different assumptions for the form of the electric field, depending on a partial or full knowledge of the material parameters, three additional sets of coupled mode equations can be cast. The selection of the particular set is determined by the selection of the parameters that are specific to a given problem. As will be shown see next, all three sets of coupled mode equations give the same result for the intensity of the electric field of both the fundamental and the second harmonic, but the solutions have different phases. The most common assumption, or anzats, consists of eliminating the fast rotation of the electric field by using a slow varying term with respect to the average wavevector at the frequency $(2)\omega$ of the form:

$$E_{\Omega}(z) = \left(\frac{2I_0}{n_{\Omega}c\epsilon_0} \right)^{\frac{1}{2}} A_{\Omega}^{(ii)}(z) e^{-ik_{\Omega}z} \quad (4.2)$$

where $\Omega = \{\omega, 2\omega\}$. This assumption can be interpreted as a representation based in the frame of reference of the average wavevector $k_{0,(2)\omega}$, instead of in the frame of reference of the electric field as in (4.1). Using this anzats, we obtain the following coupled mode equations, which we will call the type II coupled mode equations:

$$\begin{aligned} \frac{dA_{\omega}^{(ii)}(z)}{dz} + i \delta k_{o,\omega}(z) A_{\omega}^{(ii)}(z) &= -i\kappa(z) A_{2\omega}^{(ii)}(z) \left(A_{\omega}^{(ii)}(z)\right)^* e^{+i\Delta k_o z} \\ \frac{dA_{2\omega}^{(ii)}(z)}{dz} + i \delta k_{o,2\omega}(z) A_{2\omega}^{(ii)}(z) &= -i\kappa(z) \left(A_{\omega}^{(ii)}(z)\right)^2 e^{-i\Delta k_o z} \end{aligned} \quad (4.3)$$

Once again the wavevector mismatch term, $\Delta k_0 = 2k_{0,\omega} - k_{0,2\omega}$, is included in the equations mathematically to simplify them. In this case Δk_0 refers to the ‘‘average’’ wavevector mismatch in the SHG process. In this representation, the complex field $A_{(2)\omega}^{(ii)}$ has a slower rotation than the fields in (4.1).

Instead of calculating the evolution of the fields for deviations from the average wavevector, the evolution of the complete wavevector $k_{(2)\omega}(z)$ is used as the frame of reference, given by the following anzats:

$$E_{\Omega}(z) = \left(\frac{2I_0}{n_{\Omega} c \epsilon_0} \right)^{\frac{1}{2}} A_{\Omega}^{(iii)}(z) e^{-i(k_{\Omega} + \delta k_{\Omega})z} \quad (4.4)$$

where $\Omega = \{\omega, 2\omega\}$. Using the definition of the spatial dependence of the wavevector mismatch: $K(z) = 2\delta k_{\omega}(z) - \delta k_{2\omega}(z)$, the coupled mode equations, labeled type III, are:

$$\begin{aligned}
\frac{dA_{\omega}^{(iii)}(z)}{dz} - iz \frac{d}{dz} [\delta k_{o,\omega}(z)] A_{\omega}^{(iii)}(z) &= -i\kappa(z) A_{2\omega}^{(iii)}(z) \left(A_{\omega}^{(iii)}(z) \right)^* e^{+i\Delta k_o z + iK(z)z} \\
\frac{dA_{2\omega}^{(iii)}(z)}{dz} - iz \frac{d}{dz} [\delta k_{o,2\omega}(z)] A_{2\omega}^{(iii)}(z) &= -i\kappa(z) \left(A_{\omega}^{(iii)}(z) \right)^2 e^{-i\Delta k_o z - iK(z)z}
\end{aligned} \tag{4.5}$$

Using this form of the coupled mode equations it is possible to track the evolution of the SHG armed with only partial knowledge of the material properties, and the kernel of the wavevector mismatch (exponent term) follows exactly the material properties.

A fourth assumption is useful with a less intuitive interpretation but more physical insight into the problem. Instead of following the evolution of the wavevector mismatch distribution, it proves useful to calculate its cumulative effect by using the following anzats on the electric fields

$$E_{\Omega}(z) = \left(\frac{2I_0}{n_{\Omega} c \mathcal{E}_0} \right)^{\frac{1}{2}} A_{\Omega}^{(iv)}(z) e^{-i \left(k_{\Omega} z + \int_0^z \delta k(z') dz' \right)} \tag{4.6}$$

Using this anzats the following set of coupled mode equations, labeled type IV, is obtained.

It resembles the functional form of the coupled mode equations for a uniform profile (2.27)

$$\begin{aligned}
\frac{dA_{\omega}^{(iv)}(z)}{dz} &= -i\kappa(z) A_{2\omega}^{(iv)}(z) \left(A_{\omega}^{(iv)}(z) \right)^* e^{+i\Delta k_o z + i \int_0^z K(z') dz'} \\
\frac{dA_{2\omega}^{(iv)}(z)}{dz} &= -i\kappa(z) \left(A_{\omega}^{(iv)}(z) \right)^2 e^{-i\Delta k_o z - i \int_0^z K(z') dz'}
\end{aligned} \tag{4.7}$$

This form of the coupled mode equations is the most useful representation of this problem. It relies on the cumulative effect of the distribution in the nonuniform wavevector mismatch, which is a characteristic of a nonlocal process as discussed earlier. Therefore it is not surprising that this representation provides the most useful tool to study the nonuniform SHG problem. It does not require detailed and accurate information on the material properties at both frequencies, only the relative difference between them. As we will see in the next chapter, it is also useful for analyzing the inverse problem in SHG.

The four different types of coupled mode equations represent different approaches to the same problem. Each one needs different information from the material parameters, ranging from a full description of the material characteristics at both frequencies, as is the case in the type I, up to just the relative difference among the wavevectors as is the case for the equations type IV.

The solution of the four sets of coupled mode equations gives the same amplitude. Therefore, the SHG detuning curve will be the same independent of the set of equations used. The difference between the solutions is in the phase, which is the important parameter for cascading phenomena. The real electric field is the solution for the type I set of coupled mode equations (4.1). The real electric field is trivially related to the solution for the type II equations (4.3) by a constant, phase, k_0L . If both solutions are plotted against the average wavevector mismatch, Δk_0L , the phase accumulated by the second harmonic and the cascaded nonlinear phase shift will be the same in these two cases with the exception that for the type II solutions the dispersion in the phase has a line with constant slope L added to it.

For the solutions of the equations labelled type III (4.5) and IV (4.7), their inter-relationship is not as straightforward. The relation between the real electric field (type I) and the solutions in these cases depends on the particular dependence of the nonuniform wavevector distribution. At the end, what is measured in an experiment is the phase of the electric field and the different equations are a representation of the same problem. A detailed analysis of the equations and the different ansatzes shows a constant relationship for the relative phase of the different reduced amplitudes. If we express the amplitudes for the different ansatzes in the form:

$$A_{\Omega}^I = |A_{\Omega}^I| e^{i\phi_{\Omega}^{I,NL}} \quad (4.8)$$

where $\Omega = \{\omega, 2\omega\}$, and $I = \{i, ii, iii, iv\}$ we obtain the following relationship between the accumulated phases for the reduced fields, constant for all four ansatzes:

$$\Phi = 2\phi_{\omega}^{I,NL} - \phi_{2\omega}^{I,NL} = \text{constant} \quad (4.9)$$

The form of this relation is not surprising, given the nature of the problem. Considering that the accumulated phase represents the physical cascaded phase shift at both frequencies for the type I coupled mode equations, this relationship allows reconstruction of the physical phase of the field from any one of the particular representations of the coupled mode equation solutions.

As a final remark on the different representations of the coupled mode equations, with the definitions given, a nonsymmetrical wavevector mismatch for a sample of length L means that for some z , $K(z) \neq K(L-z)$. Solving the different representations of the coupled mode

equations with a variety of non-symmetrical wavevector-matching distributions shows that the output SHG power and the cascaded phase shift of the fundamental depend, in general, on the end of the sample into which the incident light is input ($z=0$ or $z=L$), i.e., there is a difference between "forward" (input at $z=0$) and "backward" (input at $z=L$) propagation. We also found that the nonreciprocity in SHG is a consequence of a nonuniformity in the propagation path. Therefore, if the structure is symmetrical about the center (i.e., $K(z) = K(L-z)$), as is the case in most of the SHG experiments, the results for "forward" and "backward" propagation are the same. This response was numerically predicted for a phase jump, and later experimentally confirmed. This will be described in the next sections.

4.3 Numerical Calculations on a Step Profile

To demonstrate the empirically established spatial nonreciprocal nature of SHG, extensive simulations were done solving the coupled mode equations in the presence of a nonuniform wavevector distribution. The study was first done in the simplest nonuniform-nonsymmetrical wavevector distribution physically possibly, consisting of two regions with different phase mismatch along the propagation path as shown in Figure 4.4. This profile can be experimentally obtained using two bulk second order crystals with different phase matching on each, as done in most seeded SHG experiments, or in a waveguide geometry by altering the effective refractive indices as performed as part of this dissertation. More general profiles will be discussed in the next chapter.

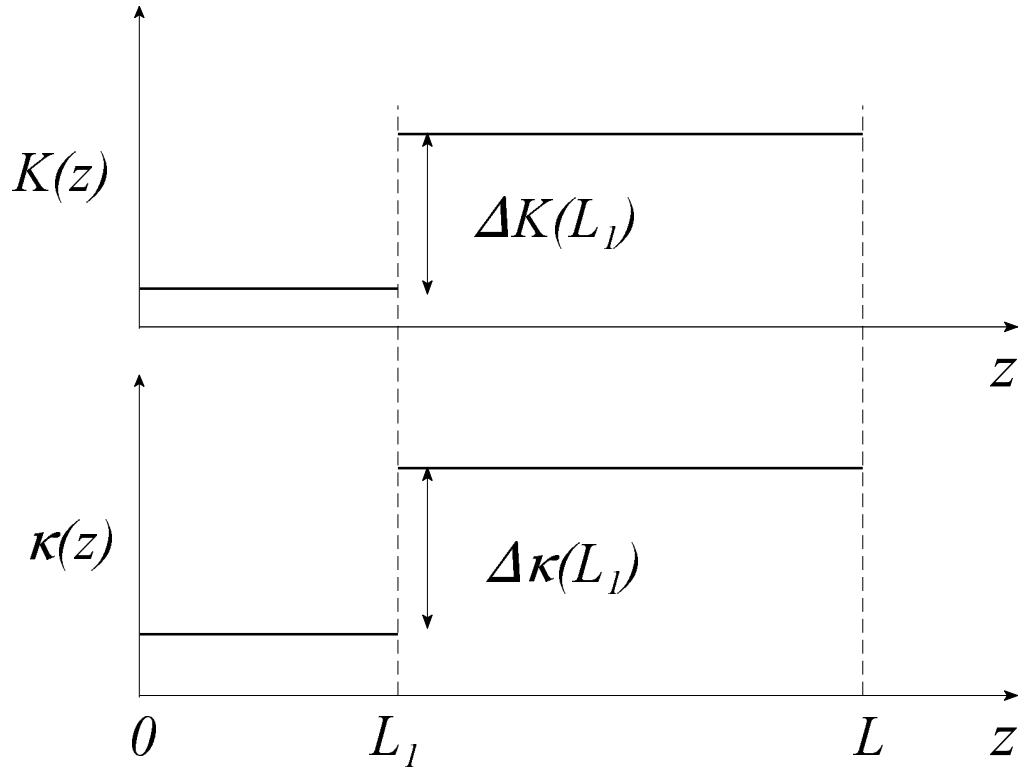


Figure 4.4 Spatial nonuniform and nonsymmetrical dependence of wavevector mismatch and nonlinear strength used to observe nonreciprocal SHG.

The analysis was done by solving the coupled mode equations (4.7) (type IV) using a fourth order Runge-Kutta method in the presence of a discontinuity along the propagation path given by

$$K(z)=\begin{cases} K_1 & 0 \leq z < L_1 \\ K_2 & L_1 \leq z \leq L \end{cases} ; \quad \kappa(z)=\begin{cases} \kappa_1 & 0 \leq z < L_1 \\ \kappa_2 & L_1 \leq z \leq L \end{cases} \quad (4.10)$$

The initial fundamental amplitude A_0 , sample length L , position of the discontinuity L_1 , the magnitude of the jump in the wavevector mismatch $\Delta K(L_1)$ and nonlinear coupling

strength $\Delta\kappa(L_1)$ were varied (Figure 4.4). A strong dependence of the SHG with detuning on the position and magnitude of the jump in wavevector mismatch and nonlinear coupling strength was found.

To illustrate the nonreciprocal nature of SHG in a nonsymmetrical structure, some second harmonic detuning curves are shown in Figure 4.5 for $A_0=1$, $\kappa_1=\kappa_2=1$, $L=1$, $\Delta K(L_1)=[K_1-K_2]=5.65$, and $L_1=0, 0.25, 0.50, 0.75$ and 1 . Here, the SHG maximum associated with the uniform case splits on forward (solid line) and backward (dashed line) propagation into two peaks (with additional side lobes). The positions of the maxima correspond closely to maxima that would be obtained from phase-matched SHG for each region separately. Note how the SHG maxima change with L_1 and depend on the propagation direction in the sample, i.e., forward versus backward. The limiting cases of uniform wavevector distribution are shown in Figure 4.5(a) and (e). The combination of parameters used ($\kappa A_0 L = 1$) correspond to the high depletion regime. Calculations show this effect is also present in the low depletion regime, with changes for the high depletion regime due to power dependent effects.

In some extreme cases the contrast between the forward and backward SHG in the calculations is large for some detuning parameters. This means that in one direction there is large second harmonic generated, and in the opposite direction there is almost none. Interpreting this directional dependence of the SHG as a directional dependent loss imposed on the fundamental can lead to an integrated optical diode based on second order processes. A potential application for this effect is an intracavity doubler in a ring laser so that the fundamental throughput in one direction is above laser threshold while the other is not, achieving a small bandwidth laser emission with no additional unidirectional elements.

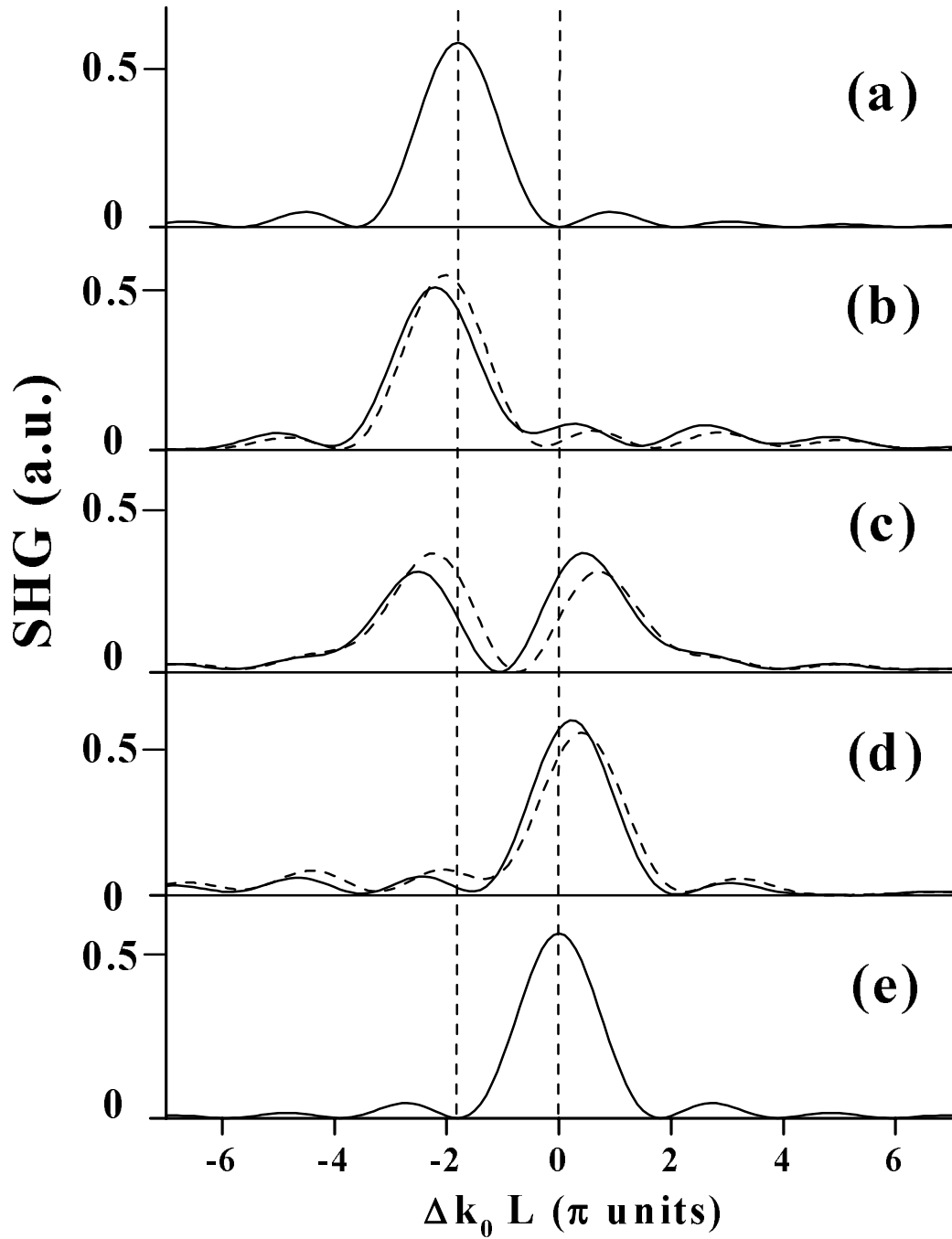


Figure 4.5 SHG intensity detuning curves in the presence of a discontinuity at the position L_1 along the propagation path. Parameters used are: $A_0=1$, $\kappa=1$, $L=1$, $\Delta K(L_1)=[K_1-K_2]=5.65$, where $K_1=K(z)$ for $0 < z < L_1$ and $K_2=K(z)$ for $L_1 < z < L$, and $L_1 =$ (a) 0, (b) $0.25L$, (c) $0.50L$, (d) $0.75L$ and (e) L .

4.4 Experimental Results on a Step Profile

The study of nonreciprocal behavior in waveguide SHG was predicted numerically by solving the coupled mode equations for a nonuniform wavevector mismatch and later confirmed experimentally. To observe and study the differences between a symmetrical and a non-symmetric structure and observe some nonreciprocal behavior, a known symmetrical structure was modified as discussed next.

Experiments were performed on a 7 μm wide by 3 μm deep, 1 cm long, PE-QPM LiNbO₃ channel waveguide, described elsewhere [44]. This waveguide was the same sample as was used in the previous chapter to observe multimode competition. The experimental waveguide and resonance were chosen to avoid large multimode competition effects. The waveguide was single mode at the fundamental wavelength and multimode at the SH. A non-symmetric wavevector distribution profile was generated by depositing a 300 μm layer of photoresist onto approximately one half of the waveguide. The change in the top layer from air ($n=1$) to photoresist ($n=1.9$) produced a change in the effective index calculated to be ≈ 0.0007 for the fundamental guided mode and ≈ 0.0006 for the SH guided mode, leading to a calculated $\Delta K \approx 8 \text{ cm}^{-1}$. Also, the effective area was increased in the over-coated region due to the weaker guided mode confinement, thus creating a calculated decrease of $\approx 20\%$ in the effective nonlinear strength.

Wavelength scans around the wavelength region where $\text{TM}_{00}(\omega) \rightarrow \text{TM}_{01}(2\omega)$ and $\text{TM}_{00}(\omega) \rightarrow \text{TM}_{11}(2\omega)$ are phase-matched interactions were taken before and after the deposition of the photoresist layer for both QCW (low power) and ML (high power) fundamental beams. The results are shown in Figure 4.6.

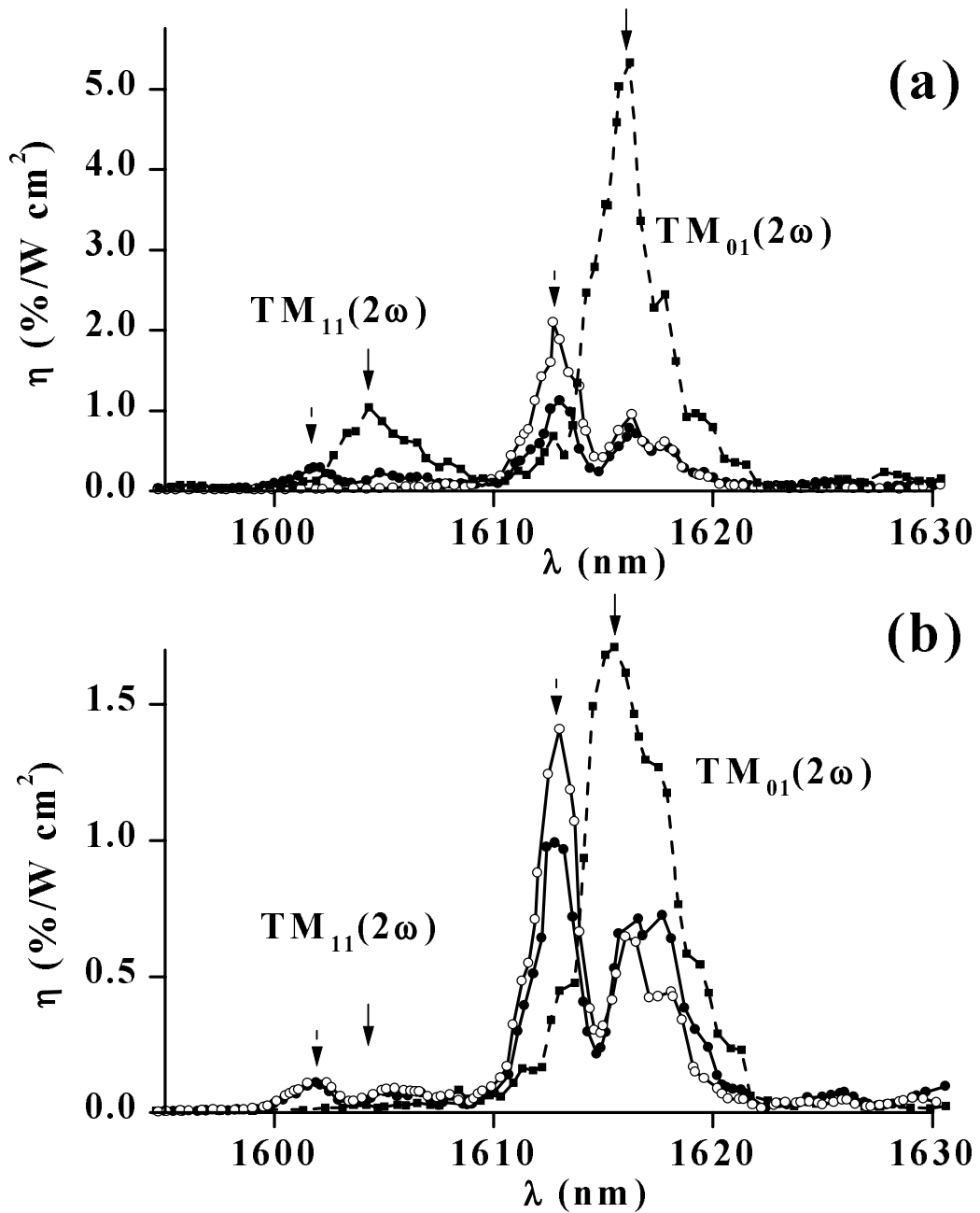
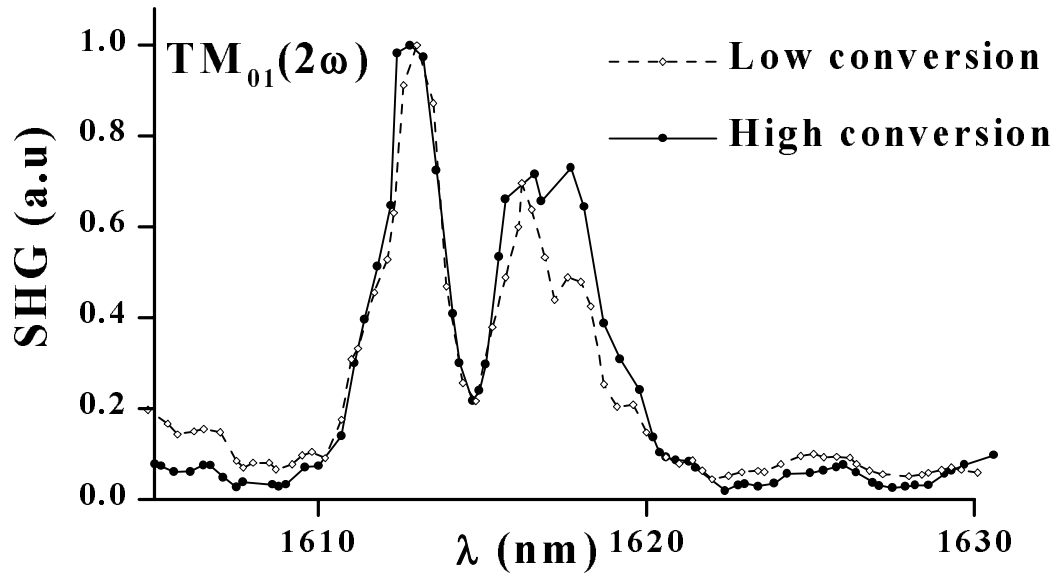


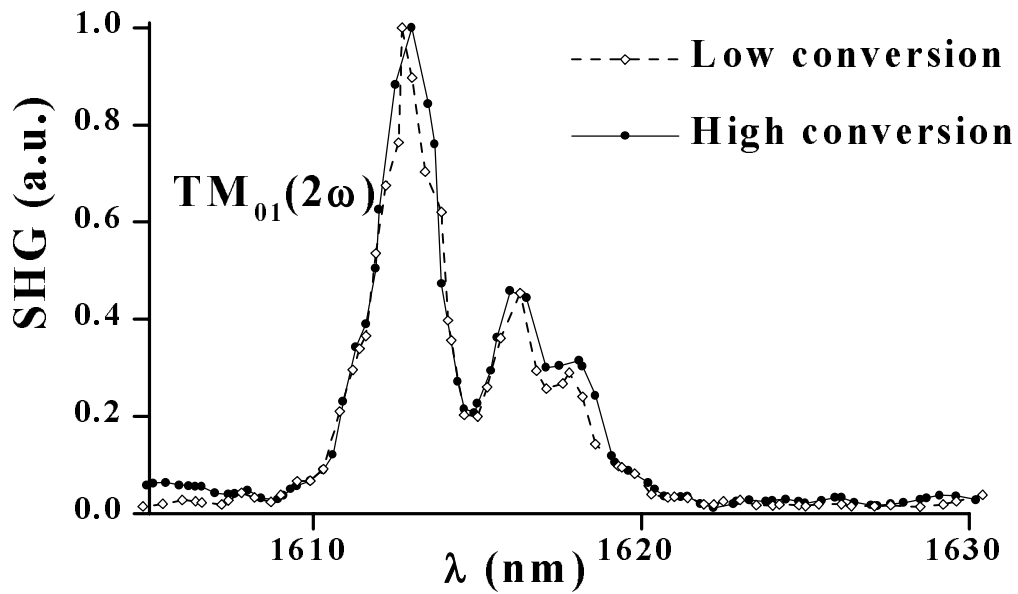
Figure 4.6 Wavelength scan of SHG in the LiNbO₃ QPM waveguide showing a nonreciprocal behavior in the (a) high and (b) low depletion regimes ($\eta_{\max} = 39\%$ and 0.8% respectively) without (dashed line) and with a layer of photoresist on half the waveguide for forward (open circles) and backward (solid circles) propagation. Solid arrows show phase matching in the region without photoresist. Dotted arrows show the phase-matching peak induced by the photoresist layer.

After correcting for Fresnel losses, the effective SH conversion efficiencies ($\eta = P(2\omega)/P(\omega)$) in the non-photoresist coated experiment was 39% for the high power case (Figure 4.6(a)) and 0.8% for the low power case (Figure 4.6(b)). The peak power of the laser was cautiously selected in order to avoid mode competition between modes. This corresponded to 10 mW average power in both cases.

For the scans without the photoresist layer, the same detuning curve by end fire coupling into either side of the waveguide was observed to within the experimental resolution of our detection system. For simplicity, only one of these curves is shown (dashed curves in Figure 4.6). In contrast to this, the detuning curves with the photoresist layer show a break-up of the original SHG maxima. One of the peaks corresponds to the original position of the resonance and the second emerges due to the effective index difference introduced by the photoresist layer. For the $TM_{00}(\omega) \rightarrow TM_{01}(2\omega)$ resonance, the relative strength of the SHG resonances depends on which side of the waveguide we couple into: on propagation from the photoresist area, labeled forward, the height of the new generated peak is twice the value of the peak near the original position (open circles), and for input into the clean area, labeled backward, the magnitude is one and a half times (closed circles). Also the wavelength at which maximum SHG occurred in the lower peak is shifted from the uniform case, in agreement with the numerical calculations. The ratios of the forward to backward peaks are essentially the same in both the high and low depletion regimes, showing that over this power range this is not a purely power dependent effect. The comparison between both regimes can be seen in Figure 4.7.



(a)



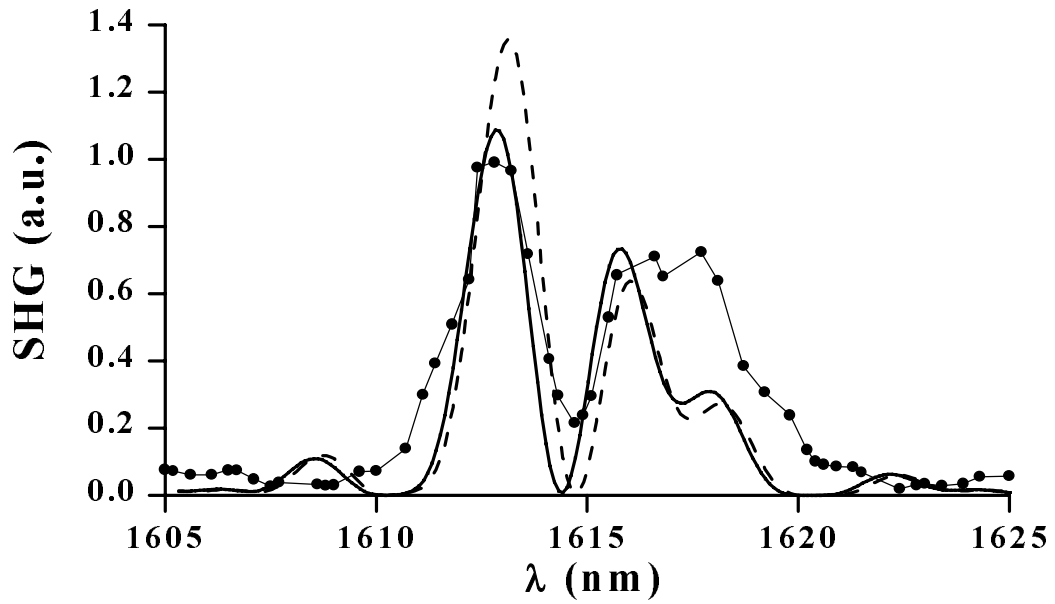
(b)

Figure 4.7 Comparison between (a) forward and (b) backward detuning curves in Figure 4.6. Effective conversion efficiencies are (a) 16.4% and 0.11%, and (b) 21% and 0.21% for high and low conversion efficiencies, respectively.

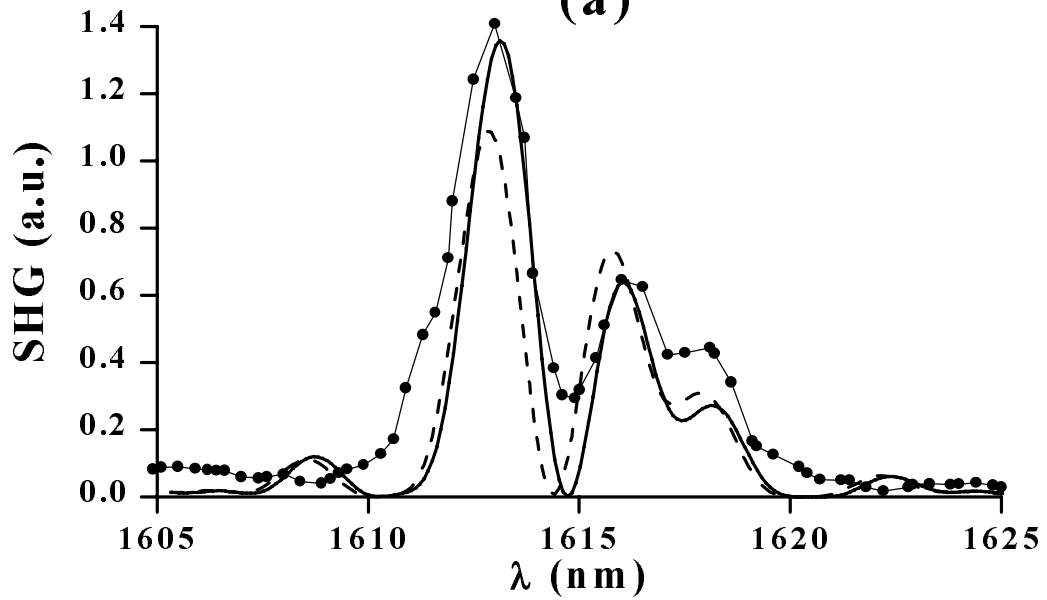
From Figure 4.7 we can observe the excellent reproducibility of the measurements in the low and high depletion regimes. As just mentioned, this result rules out nonreciprocity as a purely power dependent effect and proves that the effect is due to the characteristics of the structure. Absorptive losses induced by the photoresist layer as well as coupling losses were also modeled and discounted as responsible for this nonreciprocal effect.

The photoresist layer affected in different ways the different SHG resonances throughout the various waveguides. For example in the 2, 3 and 6 μm wide waveguides there was a definite break-up of the $\text{TM}_{00}(\omega) \rightarrow \text{TM}_{01}(2\omega)$ resonance studied before and after depositing the layer of photoresist. On the contrary, for the same interaction in the 1 and 4 μm wide waveguides the effect of the photoresist layer was not detected. This type of behavior was also seen in the numerical simulations, depending on the magnitude of the wavevector mismatch $K(z)$ and the difference in the nonlinear strength $\kappa(z)$. From these simulations, if $K(z)$ was a multiple of 2π , the effect was the same as if there was no jump at all. Comparing the effects of both parameters, it was evident that there was a stronger dependence in the details of the resulting detuning curve on the wavevector mismatch distribution than the nonlinear strength distribution.

Using the calculated differences in the 7 μm wide waveguide due to the photoresist layer, the high depletion regime (Figure 4.8) depicted in Figure 4.7 and Figure 4.6 was reproduced. However, small corrections from the predicted values in the parameters were needed to reproduce the experimental observations accurately. The parameters used are $A_0=1$, $L=1$, $\Delta K = 5.65$, with a change in nonlinear strength κ from 1 to 0.8 at $L_1=0.4L$.



(a)



(b)

Figure 4.8 Theoretical curves (solid line) fitted to the experimental high power detuning curve (closed circles) from figure Figure 4.6 for the case of (a) backward and (b) forward propagation. Complementary calculations (forward for (a) and backward for (b)) are shown as dashed lines for comparison. Parameters used are $A_0=1$, $L=1$, $\Delta K = 5.65$, with a change in nonlinear strength κ from 1 to 0.8 at $L_1=0.4L$.

The effect of the photoresist layer experimentally affected the different interactions in different ways. For example in the $TM_{00}(\omega) \rightarrow TM_{11}(2\omega)$ interaction in Figure 4.6, the ratio between the backward and forward responses is almost the same. Depending on the induced changes in the effective indices, the magnitude of the directional response is different. A detailed analysis needs to be done in each case. The response of the structure will depend on the particular conditions of the nonuniformity. For waveguide SHG these may be different for different interactions. This is the reason that the break-up on the 2 μm waveguide depicted in Figure 4.1 is only observed in the $TM_{00}(\omega) \rightarrow TM_{00}(2\omega)$ interaction, but not in the others.

In summary the existence of spatial nonreciprocity in SHG has been proved numerically and experimentally in spatially nonsymmetric structures, as a direct consequence of the perturbation in the coherent evolution between the fundamental and the second harmonic. It has been shown that in the case of SHG in a waveguide with an asymmetric wavevector mismatch, the outcome of the process depends on which side of the waveguide is the input end. Therefore in a nonsymmetric structure the SHG output depends on the direction into which the fundamental is launched and hence is spatially nonreciprocal. Although the effect was demonstrated by introducing a sharp discontinuity in the wavevector mismatch and nonlinear coupling constant in a waveguide geometry, it is expected to occur for other geometries and more general spatially nonsymmetrical profiles. This problem will be analyzed in the next chapter.

CHAPTER 5

SPATIAL NONUNIFORM PROFILES

“You’re thinking about something, my dear, and that makes you forget to talk. I can’t tell you just now what the moral of that is, but I shall remember it in a bit.”

“Perhaps it hasn’t one,” Alice ventured to remark.

“Tu, tut, child!” said the Duchess. “Everything’s got a moral, if you only can find it.”

Alice in Wonderland

Lewis Carroll

We have seen in the preceding chapters that SHG in spatially nonuniform structures presents collective characteristics that deviate from the traditional perception of the problem, namely the sinc-like detuning curve discussed in chapter two. We identify nonreciprocal behavior as one of these deviations. In a general context, the collective SHG characteristics can be changed dramatically, depending on the specific wavevector mismatch distribution that controls the local details of the energy exchange between the fundamental and second harmonic. Examples of these deviations are found in the literature [29, 30]. But, only in a few cases has the relevance of these deviations been perceived and exploited [13, 53].

As mentioned in chapter 2, with the development of quasi-phase matching (QPM) techniques it is now possible to achieve the required flexible, grating-assisted phase-matching

at almost any wavelength by spatial control of the grating period. Variations from uniform periodicity have been used towards a more efficient control on the second harmonic characteristics, either improving the tolerances or increasing the SHG bandwidth [51, 54]. Including in the analysis the concepts involved in cascaded nonlinearities a variety of new effects can be foreseen. Varying spatially (along the propagation path) the grating period now allows an additional tool for obtaining a spatially varying wavevector mismatch to tailor the SHG detuning curve. The study of the possible distribution can be used to enhance the second harmonic generation *per se*, or allow all-optical switching based on cascaded second order nonlinearities to be implemented with minimum loss to the harmonic at room temperature.

In this chapter simple mathematical tools are introduced to study general nonuniform profiles. Some numerical calculations are performed using this formalism. These calculations are confirmed by experiments showing the tailored properties of chirped grating assisted SHG. An important aspect of SHG is introduced in the form of the inverse problem in SHG.

5.1 Low Depletion SHG Detuning Curve from a Known Profile

As discussed in Chapter 2, for conventional SHG the low depletion regime gives insight into the complete SHG problem. For spatially nonuniform profiles this approximation also provides useful information on the collective SHG behavior. If the spatial variation of the wavevector mismatch ($K(z)$) and nonlinear strength ($\kappa(z)$) are known, some insights into the problem can be foreseen using the discussion from the previous chapter.

As discussed in the previous chapter, the CW coupled mode equations for nonuniform profiles can be cast into different forms. Amongst the different representations the one labeled

type IV provides the best tool for studying the low depletion characteristics of a nonuniform structure. Normalizing to the device length, we define the reduced propagation coordinate, $\tilde{z} = z/L$, and normalized wavevector mismatch, $\Omega = \Delta k_0 \cdot L$. Using these definitions, the type IV coupled mode equations (4.7) can be rewritten as:

$$\begin{aligned} \frac{dA_{\omega}^{(iv)}(\tilde{z})}{d\tilde{z}} &= -iL\kappa(\tilde{z}) A_{2\omega}^{(iv)}(\tilde{z}) A_{\omega}^{(iv)*}(\tilde{z}) e^{+i\Omega\tilde{z} + iL \int_0^{\tilde{z}} K(Lz') dz'} \\ \frac{dA_{2\omega}^{(iv)}(\tilde{z})}{d\tilde{z}} &= -iL\kappa(\tilde{z}) A_{\omega}^{(iv)2}(\tilde{z}) e^{-i\Omega\tilde{z} - iL \int_0^{\tilde{z}} K(Lz') dz'} \end{aligned} \quad (5.1)$$

Except for simple cases such as the step profile discussed in the previous chapter, no analytical solutions can be found. Therefore, if the spatial distribution of the parameters along the propagation axis is known, these equations need to be solved numerically. With the use of the normalized propagation coordinate (\tilde{z}) the integration is carried out between zero and one. Examples of these numerical solutions will be shown in the next section for simple spatial distribution profiles.

Now we turn our attention to the low depletion regime, where the amplitude of the fundamental wave can be assumed to be constant during the propagation ($A_{\omega}^{(iv)}(z) = |A_{\omega}(0)|$). Under this assumption, the first equation in (5.1) vanishes. We can directly integrate the second harmonic equation for the normalized propagation in the unseeded case ($A_{2\omega}(0) = 0$) and get:

$$\begin{aligned}
A_{2\omega}^{(iv)}(\Delta k_o L; z=L) &= -iL |A_\omega(0)|^2 \int_0^1 \kappa(\tilde{z}) e^{-i\Omega\tilde{z} - iL \int_0^{\tilde{z}} K(z') dz'} d\tilde{z} \\
&= -iL |A_\omega(0)|^2 \int_{-\infty}^{\infty} U(\tilde{z}) \kappa(\tilde{z}) e^{-iL \int_0^{\tilde{z}} K(z') dz'} e^{-i\Omega\tilde{z}} d\tilde{z}
\end{aligned} \tag{5.2}$$

where $U(\tilde{z})$ is the shifted *rectangular* function

$$U(\tilde{z}) = \begin{cases} 1 & 0 < \tilde{z} < 1 \\ 0 & \text{elsewhere} \end{cases} \tag{5.3}$$

From (5.2) a Fourier transform ($\mathcal{F}\{\}$) is identified, where the conjugate coordinates are the normalized wavevector mismatch Ω and the normalized propagation length \tilde{z} . Knowing the spatial distributions of the wavevector mismatch and the nonlinear strength we define the mismatch response function as

$$G(\tilde{z}) = U(\tilde{z}) \kappa(\tilde{z}) \exp\left(iL \int_0^{\tilde{z}} K(L\tilde{z}') d\tilde{z}' \right) \tag{5.4}$$

from which we obtain the low depletion, slow varying second harmonic field as

$$A_{2\omega}^{(iv)}(\Omega) = -iL |A_\omega(0)|^2 \mathcal{F}\{G(\tilde{z})\} \tag{5.5}$$

This is a simple and elegant result that provides the same amount of information in the linearized regime as the low depletion regime in the conventional SHG problem. Using Parseval's theorem [55] we can calculate the SHG collective behavior as a function of the normalized wavevector mismatch as

$$I_{2\omega}(\Omega) = I_{\omega}^2(0) L^2 \mathcal{F} \{ G(\tilde{z}) \star G(\tilde{z}) \} \quad (5.6)$$

where \star represents autocorrelation and $\mathcal{F}\{\}$ represents Fourier transform. This is a well-known result in communications theory: the filtering properties of a transmission line are approximately given by the Fourier transform of the autocorrelation function. This can be applied in nonlinear optics using the form of the detuning curve as the filtering function. Similar results are found in the literature [6, 56] but those authors only included discrete differences in the mismatch response function $G(\tilde{z})$. Consequently the conjugate transform coordinates \tilde{z}' and Ω' , now depend on the complete wavevector mismatch ($\Delta k_0 + K(\tilde{z}')$) and not only on the average wavevector mismatch (Δk_0). It also forces $G(\tilde{z})$ to be real so that the detuning curve is symmetric with respect to $\Omega=0$. However, in general $K(\tilde{z})$ can be a continuous function and therefore $G(\tilde{z})$ is a complex function and its corresponding Fourier transform can be asymmetric, as observed by some authors for chirped QPM gratings [57] or temperature tuned phase matching [13, 58].

This simple result (5.6) provides intrinsic information about the SHG properties of a particular spatial distribution characterized by the mismatch response function (5.4). Using this relation the analysis of the detuning curve can be done with a Fourier transform instead of the extended computational time required using the Runge-Kutta method described in the

previous chapters. As we will see later in the chapter, it also allows the synthesis of a spatial profile suitable for targeted purposes in a short time.

In obtaining (5.6) the SHG problem has been linearized, as was done in section 2.3. Therefore, all information regarding the nonlinear nature of the SHG process is lost. The outcome of this calculation is necessarily spatially reciprocal, although numerical calculations solving the complete set of equations (5.1) in the low depletion regime show a small amount of nonreciprocity as discussed in the previous chapter.

Note that for a bulk crystal, or a uniform waveguide, there are uniform wavevector and nonlinear distribution profiles: $K(\tilde{z})=0$ and $\kappa(\tilde{z})=\kappa$, and therefore $G(\tilde{z}) = U(\tilde{z})\kappa$. Using (5.6) we obtain the low depletion detuning curve

$$\begin{aligned} I_{2\omega}(\Omega) &= I_{\omega}^2(0)\kappa^2L^2\mathcal{F}\{U(\tilde{z})\star U(\tilde{z})\} \\ &= I_{\omega}^2(0)\kappa^2L^2\text{sinc}^2(\Omega/2) \end{aligned} \tag{5.7}$$

which is the same result as found in the low depletion calculation (2.30) made in chapter two.

5.2 Numerical Calculations for Arbitrary Nonuniform Profiles

Overall the solution for the coupled mode equations (5.1) in the presence of a nonuniform spatial wavevector, $K(\tilde{z})$, or a distribution in the nonlinear coupling strength, $\kappa(\tilde{z})$, may not be analytical. The only known analytical solution is for a uniform spatial distribution [1]. The SHG problem can be solved by studying the evolution of the complete coupled mode equations (5.1), or in the low depletion regime using (5.6). Notice that with the inclusion of the mismatch response function, $G(\tilde{z})$, the coupled mode equations (5.1) can be rewritten as:

$$\begin{aligned}\frac{dA_{\omega}^{(iv)}(\tilde{z})}{d\tilde{z}} &= -iLG(\tilde{z}) A_{2\omega}^{(iv)}(\tilde{z}) A_{\omega}^{(iv)*}(\tilde{z}) e^{+i\Omega\tilde{z}} \\ \frac{dA_{2\omega}^{(iv)}(\tilde{z})}{d\tilde{z}} &= -iLG^*(\tilde{z}) A_{\omega}^{(iv)2}(\tilde{z}) e^{-i\Omega\tilde{z}}\end{aligned}\tag{5.8}$$

By comparison with the CW coupled mode equations (2.34) we can identify the mismatch response function $G(\tilde{z})$ as an “effective” nonlocal-nonlinear coupling strength. The form of the mismatch response function (5.4) depends on the forms of $K(\tilde{z})$ and $\kappa(\tilde{z})$. These two functions are arbitrary. Therefore, the variety of possibilities is infinite.

Before attempting a full description of this problem, an insight into the variety of possibilities is useful. In this work a full theoretical description of the function-space is not done. Only a few experimentally feasible spatial nonuniform distributions are studied. At this point, foreseeing a set of functions that are the bases for the nonlinear problem to construct more complex behavior is impossible. Therefore, any set of functions studied provides some insight. The functions selected were simple wavevector polynomial distributions in the presence of an uniform nonlinear strength distribution. This choice obeys the experimentally engineered wavevector distributions used to demonstrate the tailorability of the SHG detuning curves shown in the next section. $G(\tilde{z})$ was calculated using a uniform nonlinear strength ($\kappa(\tilde{z}) = \kappa$) and a polynomial wavevector distribution along the axis of the form: $K(\tilde{z}) = \beta(\tilde{z} - 0.5)^n$. The results of low depletion numerical calculations for the lowest order polynomials ($n=0,1,2,3$) are shown in Figure 5.1.

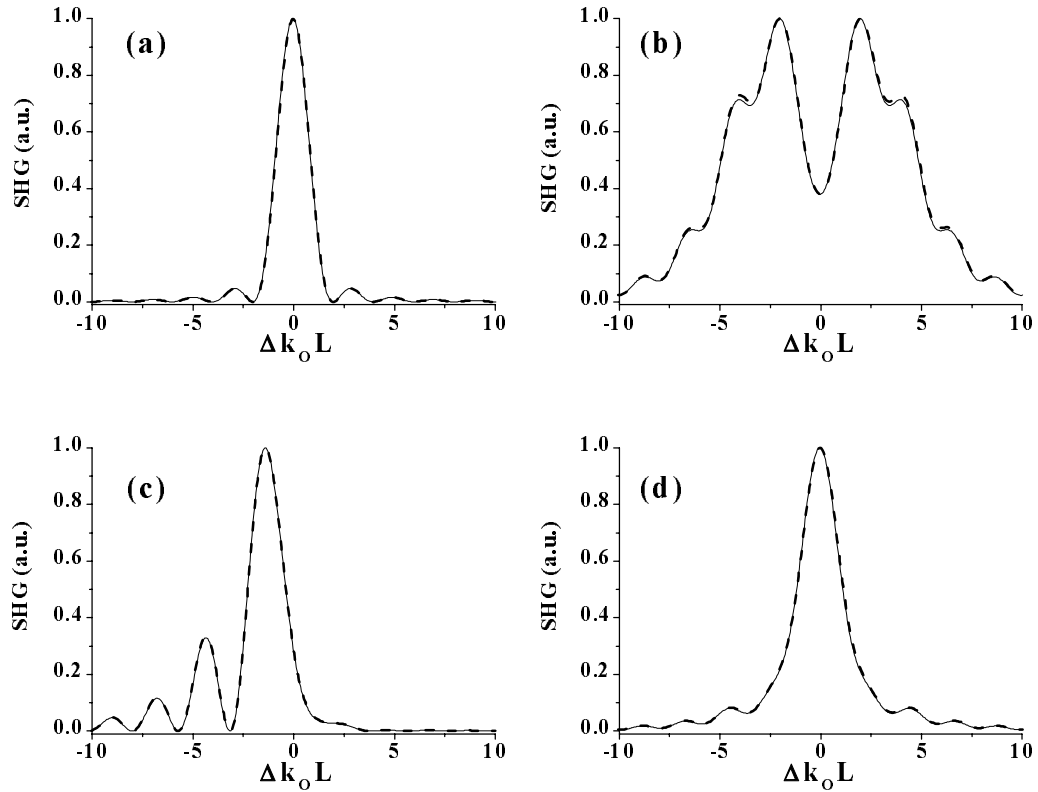


Figure 5.1 Normalized SHG detuning curves in the low depletion regime for a uniform nonlinear strength and different nonuniform wavevector distribution along the axis of the form $K(\tilde{z})=\beta(\tilde{z}-0.5)^n$. Values of $\beta = 21 \cdot 2^n$ for (a) $n = 0$, (b) $n = 1$, (c) $n = 2$, and (d) $n = 3$ were used. Solid lines were calculated solving (5.1) with a fourth order Runge-Kutta method with $\kappa|\mathbf{A}_\omega(\mathbf{0})|\mathbf{L} = 0.04$. Dashed lines were calculated using the result (5.6).

The calculations in the low depletion regime can be done either by direct integration of the coupled mode equations (5.1), or by using the result (5.6). Notice the remarkable numerical agreement between both approaches as observed in Figure 5.1. The only difference is in computational time. The exact solution requires several minutes to complete, while the calculation using (5.6) is almost instantaneous, i.e. takes just a few seconds.

From these simple calculations we can deduce a variety of characteristics found in the detuning curve that are common to most of the numerical calculations studied. Due to the form of the polynomial chosen, $K(\tilde{z})$ is either symmetric for even values of \mathbf{n} ($K(\tilde{z})=K(1-\tilde{z})$), or antisymmetric for odd values of \mathbf{n} ($K(\tilde{z})=-K(1-\tilde{z})$). Based on previous discussions, the outcome of the simulations is reciprocal for even powers of \mathbf{n} , but nonsymmetrical with respect to Ω . For odd powers of \mathbf{n} the outcome cannot be predicted *a priori*. The case $\mathbf{n}=0$ (Figure 5.1(a)) is the sinc²-like response studied in the traditional SHG problem. The case $\mathbf{n}=1$ (Figure 5.1(b)) is perhaps the most widely studied nonuniform profile. It exhibits properties that are different from all the other polynomial wavevector distributions studied. The central lobe in the detuning curve is usually the broadest amongst the different nonuniform profiles, and the cascaded nonlinear phase shift imposed onto the fundamental is reduced, overlapping with the region of strong harmonic generation.

For $\mathbf{n}=2$ (Figure 5.1(c)) the basic characteristics associated with higher order nonuniform polynomial wavevector profiles are present. The detuning curve is asymmetric with respect to $\Omega=0$. On one side large oscillations in the second harmonic are present, on the opposite side the conversion is small. Also the cascaded phase shift in the region of small harmonic generation is larger and relatively flat. This behavior was experimentally observed with yet more complex wavevector distributions [13]. The selection of the particular form of $K(\tilde{z})$ used to exemplify nonuniform profiles is evident in the case $\mathbf{n}=3$ (Figure 5.1(d)). Due to the inflection point at the middle of the propagation, the evolution of fields is compensated causing a symmetrical detuning curve with respect to $\Omega=0$. Then the detuning curve is reciprocal with the propagation direction. If the inflection point is chosen to be different from

the mid point of the propagation, the resulting detuning curve exhibits characteristics similar to the curve shown in Figure 5.1(c). Higher order polynomial wavevector distributions exhibit general characteristics similar to the last two cases ($n=2,3$) discussed with but small variations.

Similar calculations in the high depletion regime for the same four cases just discussed are shown in Figure 5.2. All the basic characteristics mentioned for the low depletion regime are preserved, with additional features due to cascaded effects present.

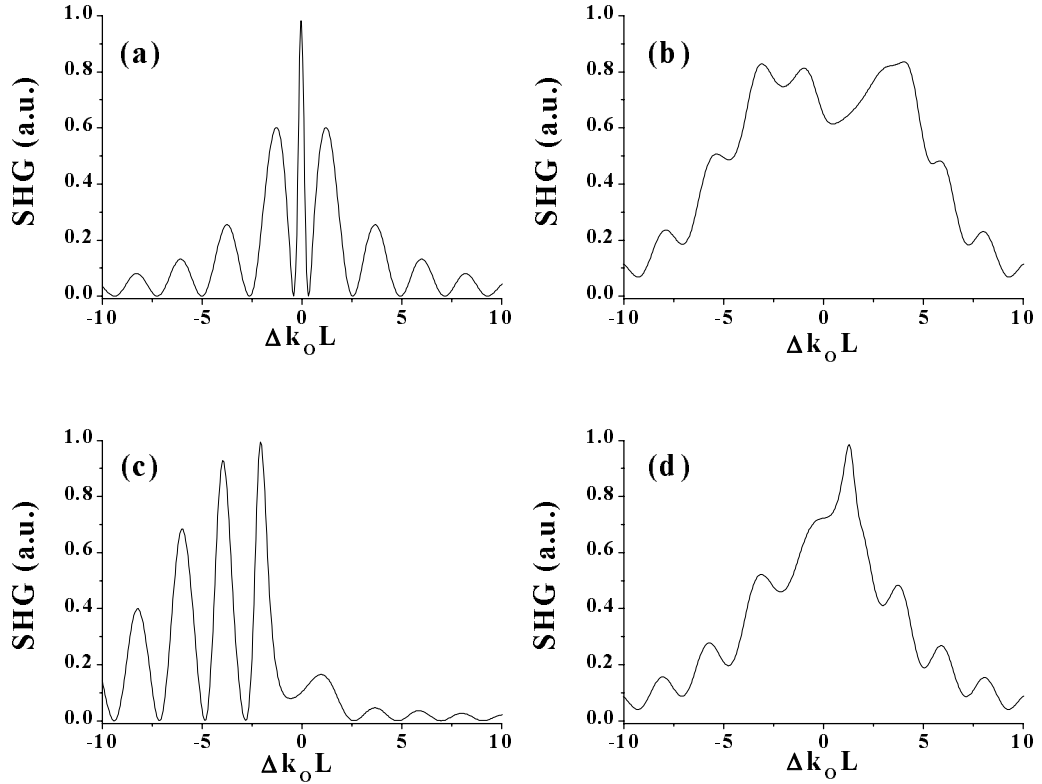


Figure 5.2 High depletion regime SHG detuning curves for a uniform nonlinear strength and different nonuniform wavevector distribution along the axis of the form $K(\tilde{z})=\beta(\tilde{z}-0.5)^n$. Values of $\beta = 21 \cdot 2^n$ for (a) $n = 0$, (b) $n = 1$, (c) $n = 2$, and (d) $n = 3$ were used. Calculation was done solving (5.1) with a fourth order Runge-Kutta method with $\kappa|\mathbf{A}_\omega(\mathbf{0})|\mathbf{L} = 4$.

For this figure the numerical calculations were not normalized, in contrast to Figure 5.1. The uniform case (Figure 5.2(a)) exhibits all the cascaded features discussed earlier. The distortion due to the nonlinear phase shift imposed onto the fundamental also modifies the polynomial nonuniform distribution studied. For the linear case ($n=1$), we observe in Figure 5.2(b) that, just as in the low depletion regime, the bandwidth of the central lobe is the broadest amongst the different curves. We can also observe that the generated harmonic is smaller than in the other examples. For $n=2$ and $n=3$ (Figure 5.2(c) and (d), respectively) the detuning curve is different from the corresponding low depletion regime calculations. However, the main features of the detuning curve highlighted earlier are present in the high depletion regime. Because of cascading effects, the magnitude of the side-lobes increases and the distance between peaks decreases. Additionally some asymmetric distortion due to the presence of the nonuniform profile can be observed, but preserving the overall response.

The nonlinear phase shift imposed onto the fundamental corresponding to the curves depicted in Figure 5.2 is shown in Figure 5.3. Distinctive features characteristic of cascaded nonlinearities are present in all of them. A change in the sign of the phase shift is the predominant feature in this figure. For the uniform case (Figure 5.3(a)) the nonlinear phase shift is symmetric with respect to $\Omega=0$, as discussed in chapter 2. For a linear variation (Figure 5.3(b)) the phase shift is smaller and has a larger bandwidth than in the uniform case. Comparing with Figure 5.2(b), the regions where the nonlinear phase shift is the largest correspond to the most efficient harmonic generation. Therefore this profile is not useful for all-optical switching, but it proves valuable for enhancement in the SHG bandwidth of the structure. The smaller conversion efficiency is a price for this enhanced bandwidth.

The quadratic variation (Figure 5.3(c)) has a region with a large phase shift that coincides with a region of small harmonic generation. Here the phase shift is obtained without “loss” of the fundamental field manifested as harmonic generation. Similar behavior was observed for higher even power nonuniform wavevector distributions. For $n=3$ the nonlinear phase shift (Figure 5.3(d)) is also enhanced relative to the uniform distribution. Here the large phase shift coincides with a region of large harmonic generation. This behavior was also common to odd powers in the polynomial wavevector distribution.

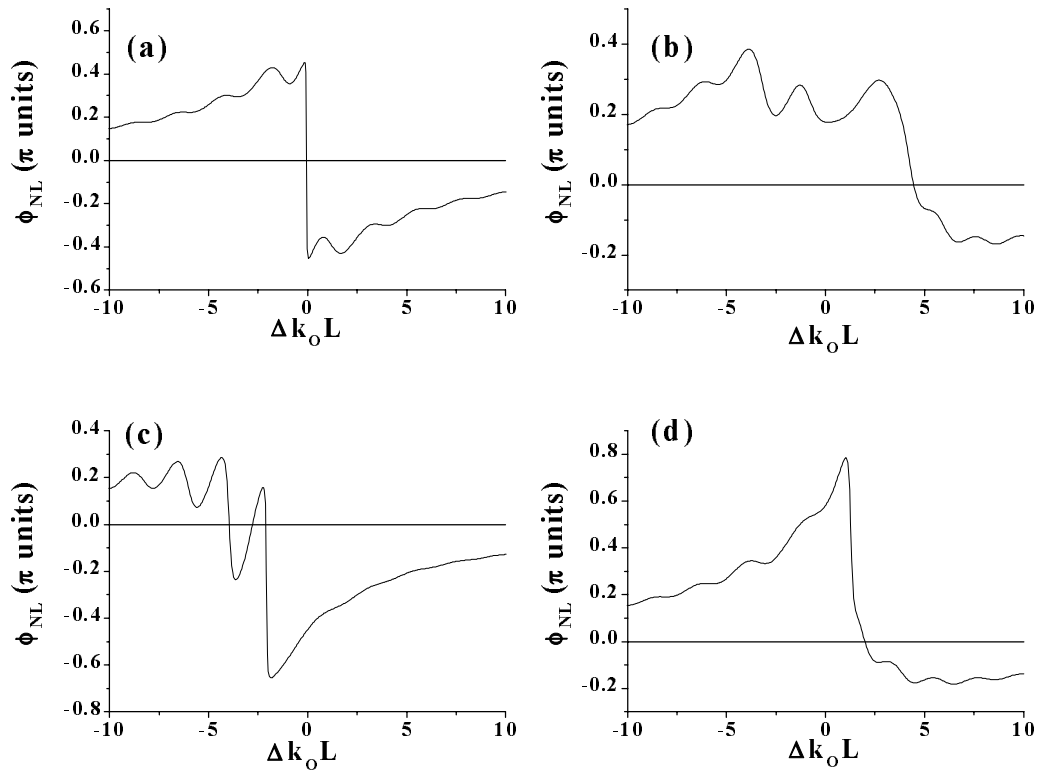


Figure 5.3 Cascaded nonlinear phase shift corresponding to the curves in Figure 5.2. A wavevector distribution along the axis of the form $K(\tilde{z}) = \beta(\tilde{z}-0.5)^n$ is assumed. Values of $\beta = 21 \cdot 2^n$ for (a) $n = 0$, (b) $n = 1$, (c) $n = 2$, and (d) $n = 3$ were used. Calculation was done solving (5.1) with a fourth order Runge-Kutta method with $\kappa |A_\omega(\mathbf{0})| L = 4$.

The analysis was extended up to the 15th power in the polynomial nonuniform wavevector distribution. Except for some differences in the relative height of the different side lobes, the general characteristics were preserved by even and odd powers. A common feature was observed amongst the different calculations, namely that the position of large and smooth nonlinear phase shifts, depending on a change of curvature in the spatial distribution, corresponds to a region of high or low harmonic generation. That is, for even powers of the spatial distribution, the region of large phase shift coincides with regions of low harmonic generation. The opposite occurs for odd powers in the polynomial wavevector distribution.

Some of the different distributions studied have potential applications. The linear variation ($n=1$) could be useful for enhancing the SHG bandwidth. Even powers of the polynomial distribution present advantages for all-optical processes as described elsewhere [13]: large nonlinear phase shift in a region of small harmonic generation.

A numerical curiosity was identified from these calculations. If the sign of the nonuniform wavevector distribution changes sign (i.e., inverted: $K(\tilde{z}) \rightarrow -K(\tilde{z})$) the detuning curves depicted in Figure 5.1 and Figure 5.2 are inverted with respect to $\Omega=0$. Additionally, the nonlinear phase shift imposed onto the fundamental, as shown in Figure 5.3, is inverted with respect to the line $\Omega=\phi_{NL}$. These symmetry properties were general to all calculations.

Several wavevector distributions with a constant nonlinear coupling strength were studied. The amount of information provided by these calculations is overwhelming. From these numerical simulations only a few features could be extracted. A systematic theoretical and numerical analysis is required to achieve a complete understanding of the SHG problem in the presence of nonuniform spatial distributions.

5.3 Inverse Problem

Second harmonic generation in the presence of nonuniform wavevector distributions presents an interesting theoretical problem. For standard SHG in spatial uniform distributions the theory is elegant and complete. The inclusion of distance-dependent changes in either the nonlinear strength or the wavevector distribution introduces a variety of additional degrees of freedom for achieving a controlled SHG detuning curve. So far the study has been focused on departures from a given nonuniform distribution and observing the outcome of the second order process. In the low depletion regime, under special considerations, it is possible to extract the nonuniform distribution information along the propagation direction that leads to the given collective behavior of the second order process. This analysis is called the **inverse problem** solution.

The inverse problem solution is a tool used to synthesize a spatial nonuniform wavevector or spatial nonlinear strength distributions to enhance one or more of the collective characteristics of second harmonic generation, namely the SHG bandwidth or the nonlinear cascaded phase shift. It relies on retrieving information from a given detuning curve and deducing the spatial distribution that causes it.

We can obtain information about the mismatch response function $G(\tilde{z})$ in the low depletion regime by either deconvolving the information from the intensity detuning curve using (5.6), or by direct inverse Fourier transform of the reduced electric field $A_{2\omega}^{(iv)}(\Omega)$ using (5.5). Either approach is hard to implement. The use of the deconvolution requires additional information regarding the phase of the $G(\tilde{z})$ which is the information we want to retrieve. The best approach is to use the expression (5.6) to retrieve the information about the spatial

nonlinear coupling strength and the spatial nonuniform wavevector distributions along the propagation axis. In the low depletion regime, from (5.6) this gives:

$$\begin{aligned}\kappa(0 < \tilde{z} < L) &= |G(\tilde{z})| \\ &= \frac{1}{L|A_\omega(0)|^2} \left| \mathcal{F}^{-1}\{A_{2\omega}^{(iv)}(\Omega)\} \right|\end{aligned}\quad (5.9)$$

$$\begin{aligned}K(0 < z < L) &= \frac{d}{d\tilde{z}} \left[\frac{1}{L} \angle G(\tilde{z}) \right] \\ &= \frac{1}{L} \frac{d}{d\tilde{z}} \left[\angle \mathcal{F}^{-1}\{A_{2\omega}^{(iv)}(\Omega)\} \right]\end{aligned}\quad (5.10)$$

Here “ \angle ” represent the complex phase argument and $\mathcal{F}^{-1}\{\}$ is the inverse Fourier transform. These expressions are only valid in the low depletion regime, and only for using the type IV anzats. If some other anzats is used the result differs from the actual spatial distributions.

To illustrate the difference, the solutions in the low depletion regime using the coupled mode equations types III and IV are shown in Figure 5.4. Here the wavevector spatial profile is the same as in section 5.2, with $n=1$, $\beta=12.6$ and $\kappa|A_\omega(0)|L= 0.04$. Although the calculation is performed in the low depletion regime ($\eta \approx 0.15\%$), numerically there is some depletion of the fundamental. There is also a negligible cascaded phase shift imposed onto the fundamental. We observe differences in the calculated phases using the type III or type IV equations for the fundamental and second harmonic (Figure 5.4(c) and (d)) where-as for the intensities (Figure 5.4(a) and (b)) there are none.

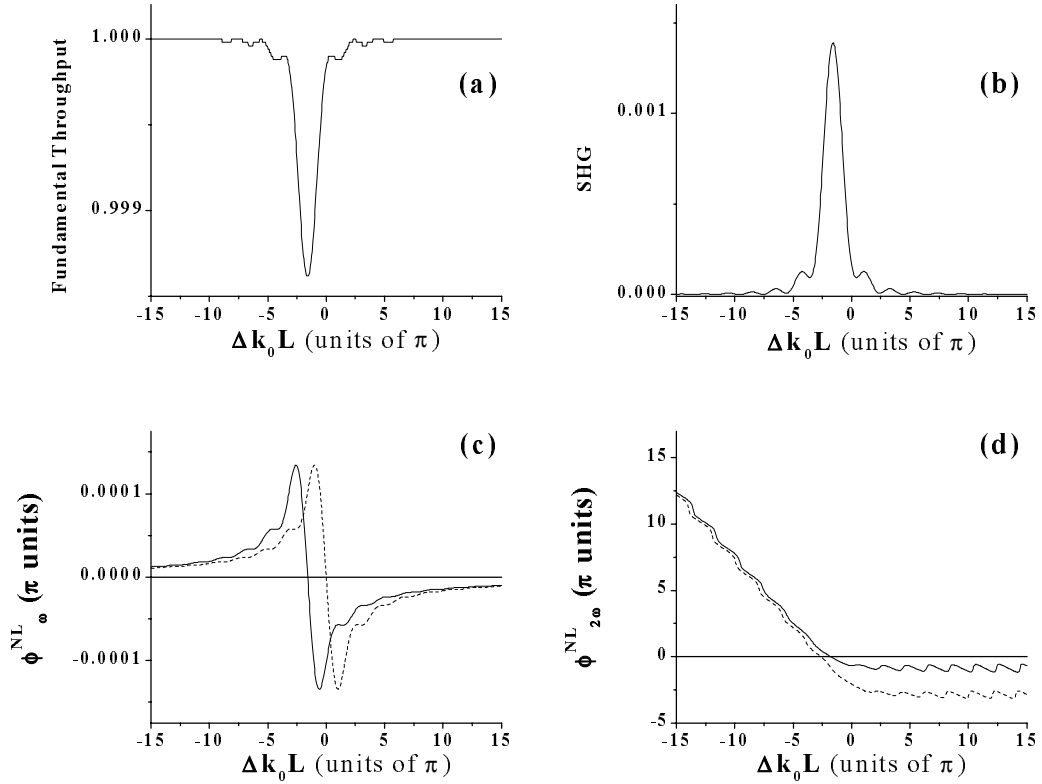


Figure 5.4 Exact coupled mode equation solutions in the presence of a linear nonuniform wavevector variation in the low depletion regime ($\kappa |A_{\omega}(0)|L = 0.04$). (a) Fundamental intensity throughput, (b) second harmonic intensity generated, (c) fundamental cascaded nonlinear phase shift using the coupled mode equations type III (dashed) and type IV (solid), and (d) second harmonic nonlinear phase shift using the coupled mode equations type iii (dashed) and type iv (solid).

Experimentally it is possible to measure the intensity and phase of the fundamental and harmonic fields. These measurements correspond to the ansatz used in the coupled mode equations type I. In order to apply the inverse method, *a priori* knowledge of the spatial distribution of the wavevector is required. But this is the information that the method is meant to extract, therefore creating a vicious circle. From these measurements the inverse problem solution can't be directly applied unless there is additional information collected.

Examples of this method are shown in Figure 5.5. Two different nonuniform spatial wavevector distributions are shown using a uniform nonlinear strength: a linear variation (Figure 5.5(a)) and an adiabatic profile (Figure 5.5(b)) as discussed elsewhere [59]. Solid lines show the reconstruction from the detuning curves back to the spatial profile. Dashed curves show the assumed spatial variation used to calculate the detuning curves using (5.1). The inverse calculations are in excellent numerical agreement with the original input.

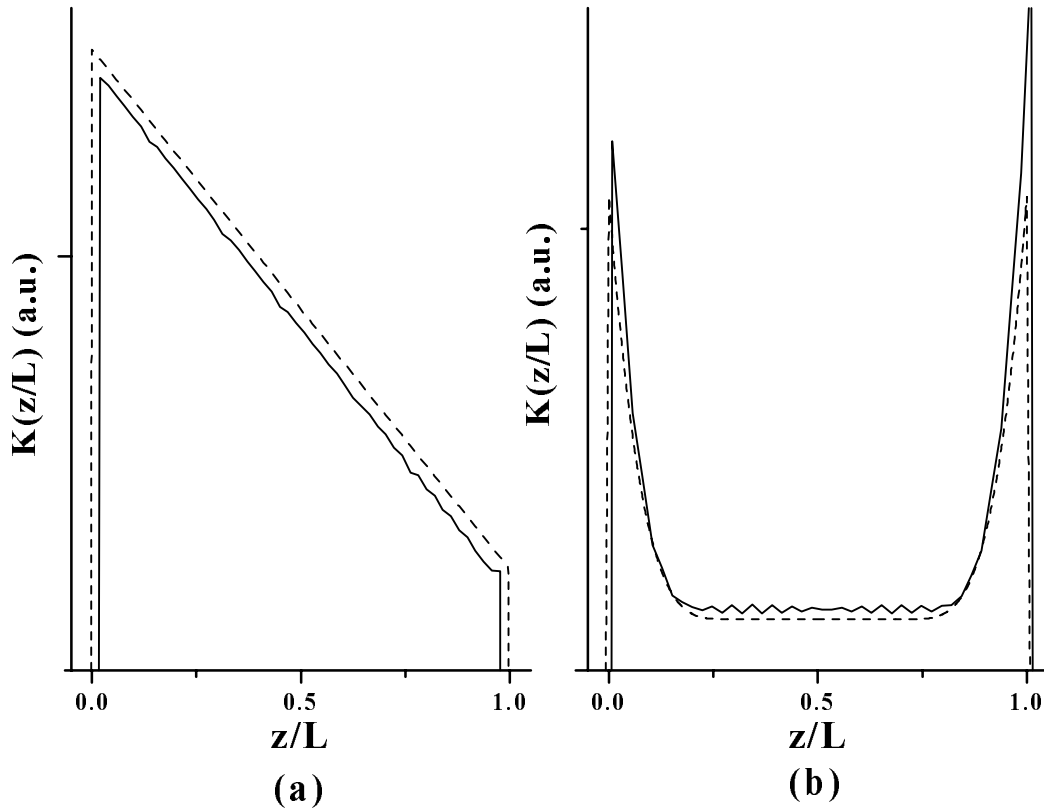


Figure 5.5 Result from the inverse problem method for (a) linear and (b) adiabatic spatial nonuniform profiles. Dashed line show the original profiles used to calculate the detuning curves using (5.1). Solid lines are the reconstruction using the invese problem method.

While investigating the differences between the inverse problem results using the four different sets of coupled mode equations, an interesting numerical property was observed. For the type I coupled mode equations, the second harmonic detuning curve (Figure 5.4(b)) and the nonlinear phase shift imposed onto the fundamental (Figure 5.4(c)) are closely related by a Hilbert transform [55]. This result was consistent in the high and the low depletion regimes. In the context of general nonlinear optics similar results exist [60]. The dispersion relations which relate the real part of the optical susceptibility (refraction) and imaginary part (absorption) are related with a Hilbert transform. These are known as the Kramers-Krönig relations. It involves only odd powers of the optical susceptibility (2.2) that are related with physical changes in the refractive index (2.12). As discussed in section 2.1, it causes a change in the phase of the electric field. For cascaded second order nonlinearities there is no physical model supporting a similar result. A possible explanation for the numerical observation can be proposed: SHG can be interpreted as a two photon absorption of the fundamental. A similar relationship has been observed numerically in the low depletion regime for a uniform wavevector mismatch distribution [61]. If this point of view is accepted, SHG imposes a change in the phase of the fundamental field manifested as the cascaded phase shift imposed onto the fundamental, without creating a real change in the refractive index. This statement will remain in this work just a numerical observation, although it certainly requires further consideration.

Accepting this relation between the SHG detuning curve and the cascaded NL phase shift imposed onto the fundamental, under the non-seeded lossless assumption, relates three of the four curves depicted in Figure 5.4. The fundamental and harmonic intensity curves are

the complement of each other to the input fundamental field, $|A_{\omega}(0)|^2$. The harmonic intensity curve and the nonlinear cascaded phase shift imposed onto the fundamental are related by a Hilbert transform. Unfortunately, a relationship between the phase of the second harmonic and any of the other quantities has not been found. Because the nonlinear phase shift of the fundamental is due to a succession of second order processes, the information of each individual process is lost. It is not possible to relate the phase of the fundamental to the harmonic, although there is the relation (4.9) between the phases for the four different ansatz.

The inverse problem solution still has some practical points that require further research. It is an extremely powerful tool for engineering a nonuniform profile. With this method a spatial distribution along the propagation axis can be synthesized. In an iterative process the spatial distribution can be adjusted to achieve the desired performance to enhance either the SHG bandwidth or the nonlinear phase shift properties. For example, if one desire to have a flat top SHG detuning curve to enhance the tolerances using (5.9) and (5.10) a uniform nonlinear strength distribution with a spatial wavevector distribution of the form $K(\tilde{z}) \propto \text{sync}(\tilde{z})$ is required.

A variety of spatial distributions can be conceived. As mentioned before, there are an infinite number of possibilities for constructing $G(\tilde{z})$. It may not be possible to transfer all of these into a real physical device, and some remain as theoretical curiosities. Before attempting a numerical study in more complex spatial nonuniform distributions, experimental evidence of the viable engineerable distributions is required. The first steps towards this goal are presented in the next section.

5.4 Experimental Results in a General Profile

The complex response due to a spatially nonuniform wavevector distribution along the propagation axis has been experimentally reported [6, 13, 30, 51, 62]. These observations were made in waveguide SHG where the phasematching technique induced a certain amount of nonuniformity (temperature tuned or grating assisted).

In this work controlled, grating assisted, phasematching was studied. In particular, the low depletion SHG response of an engineered, nonuniform-nonsymmetric wavevector distribution along the propagation axis was investigated. The specific variation in the wavevector mismatch was achieved by a nonuniform chirp (i.e., not a linear chirp) in the grating period of a LiNbO₃ periodic segmented waveguide (PSW). The approach used here is different from the traditional method used to study grating assisted phasematching [29]. Normally it consists of decomposing the grating response into its Fourier components and analyzing the response of the structure from the material point of view. All grating assisted phasematching techniques (QPM, segmented waveguides, periodic domain inversion, ...) can be studied using the Fourier decomposition approach. We can interpret this type of phasematching in a different way, as mentioned previously in chapter two. Here we do not assume phasematching caused by a grating wavevector added to the material phase mismatch. Instead we assume that there is “a” phasematching condition perturbed by other phasematched processes. This is similar to the point of view used to describe multimode competition. The additional SHG processes mentioned are the material phase mismatch and phasematching through different grating orders. Although the physics is the same for both approaches, the mathematical formalism and the interpretation are different. The mathematical

description presented earlier in the chapter can be applied directly with the approach presented here. The presence of the grating is interpreted as a reduced nonlinear strength dependent on the grating order involved in the process. The agreement between the experimental results and the simulations supports this simplification.

To establish the conditions needed to fabricate the desired chirped grating, uniform PSW waveguides with periods in the 17.5-20 μm range were fabricated and their SHG response measured. Typical SHG responses of these waveguides are shown in Figure 5.6.

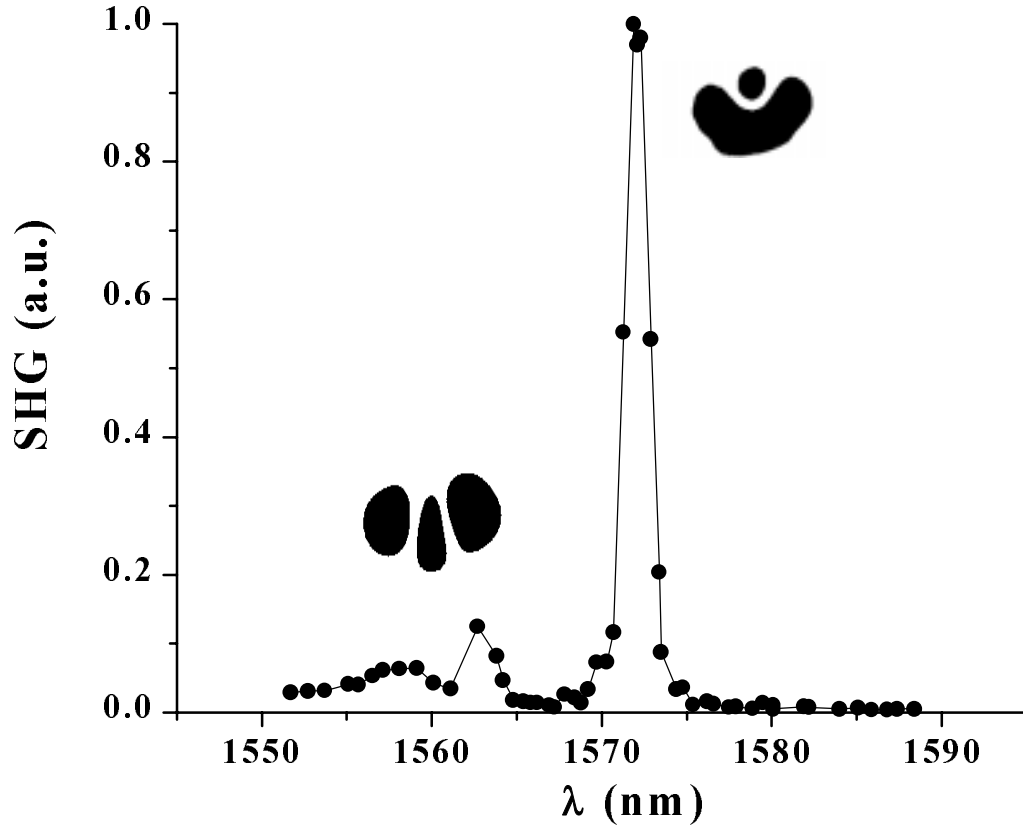


Figure 5.6 Experimental uniform PSW detuning curve. This curve is for a segmented grating period of 19 μm . A binary representation of the phasematched modes is also shown.

The PSW waveguides were fabricated at the University of Glasgow by titanium indiffusion into a 1 cm z-cut sample of LiNbO₃ by standard lithographical techniques. Estimated dimensions were 6 μm wide by 5 μm depth. Only the TM₀₀(ω) was supported in the 1495 nm to 1625 nm wavelength region. Using the lossy Fabry-Perot method [63], the fundamental losses were measured to be 1.9 dB/cm, which is 0.9 dB/cm more than an equivalent continuous waveguide.

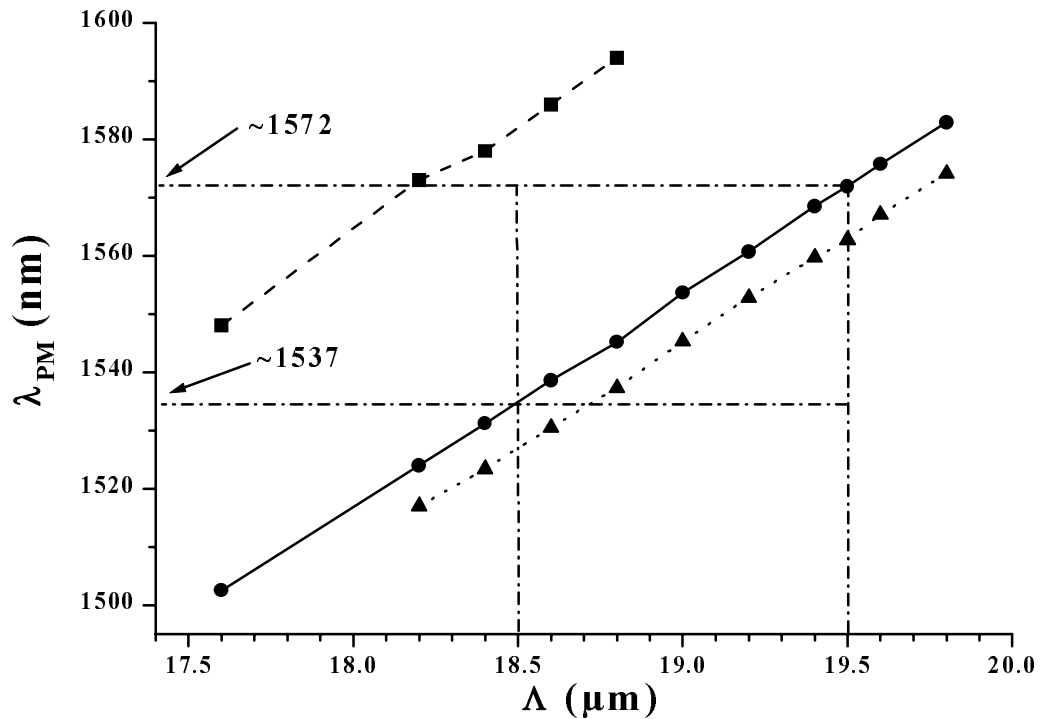


Figure 5.7 Phase matching wavelength vs. PSW grating period for the TM₀₀(ω) → TM₀₀(2ω) (dashed line), TM₀₀(ω) → TM₀₁(2ω) (solid line) and TM₀₀(ω) → TM₂₀(2ω) (dotted line). Average SHG conversion efficiencies for 100 W input fundamental are 0.09%, 1.5%, and 0.2%, respectively. The dash-dotted lines represents the PSW grating period range used in the nonuniform profile mask design.

The interactions $TM_{00}(\omega) \rightarrow TM_{00}(2\omega)$, $TM_{00}(\omega) \rightarrow TM_{01}(2\omega)$ and $TM_{00}(\omega) \rightarrow TM_{20}(2\omega)$ occurred in the wavelength region scanned. They had bandwidths of ~ 1.3 nm. Care was taken to assure the correct polarization labeling. Conversion efficiencies of 0.09%, 1.5% and 0.2%, respectively, for a 100 W fundamental input from a the color center laser were observed. The complete characterization of these waveguides is shown in Figure 5.7. The nonuniform waveguides selected for further experiments had chirped grating periods between 18.5 μ m and 19.5 μ m, suitable for first grating order phasematching between 1537 nm and 1572 nm for the $TM_{00}(\omega) \rightarrow TM_{01}(2\omega)$ interaction, as depicted in Figure 5.7.

To create a nonuniform wavevector distribution the required chirp was synthesized by first calculating the smoothly varying wavevector mismatch needed to have the desired response function. For this work a quadratic chirp grating distribution was selected. This generates a quadratic wavevector mismatch distribution. The distribution was discretized into different sections whose period was chosen to give the appropriate average mismatch for each section. To obtain the periodicity of the grating as a function of distance,

$$\Lambda(z) = A \cdot z^2 + \Lambda_0 \quad (5.11)$$

where \mathbf{A} is the amplitude of the function and Λ_0 is the initial period. If the function is discretized into N sections along the propagation distance, \mathbf{L} ($=N \cdot \Delta z$), the average period for each section is given by

$$\Lambda_i = (A \cdot \Delta z^2) \cdot i^2 + \Lambda_0 = \frac{\Lambda_f - \Lambda_0}{(N-1)^2} \cdot i^2 + \Lambda_0 \quad (5.12)$$

where Λ_f is the final grating period and $i \{= 0, \dots, N-1\}$ is an indexing number.

A mask was then fabricated with a few (5-10) uniform segments making up each section to obtain a step-wise change in the grating period ranging between $\Lambda_0 = 18.5$ and $\Lambda_f = 19.5 \mu\text{m}$. The variations were done in $N=30$ or 60 different segments of equal periodicity in a stepwise fashion. Three different nonuniform designs including a quadratic profile were investigated (Figure 5.8).

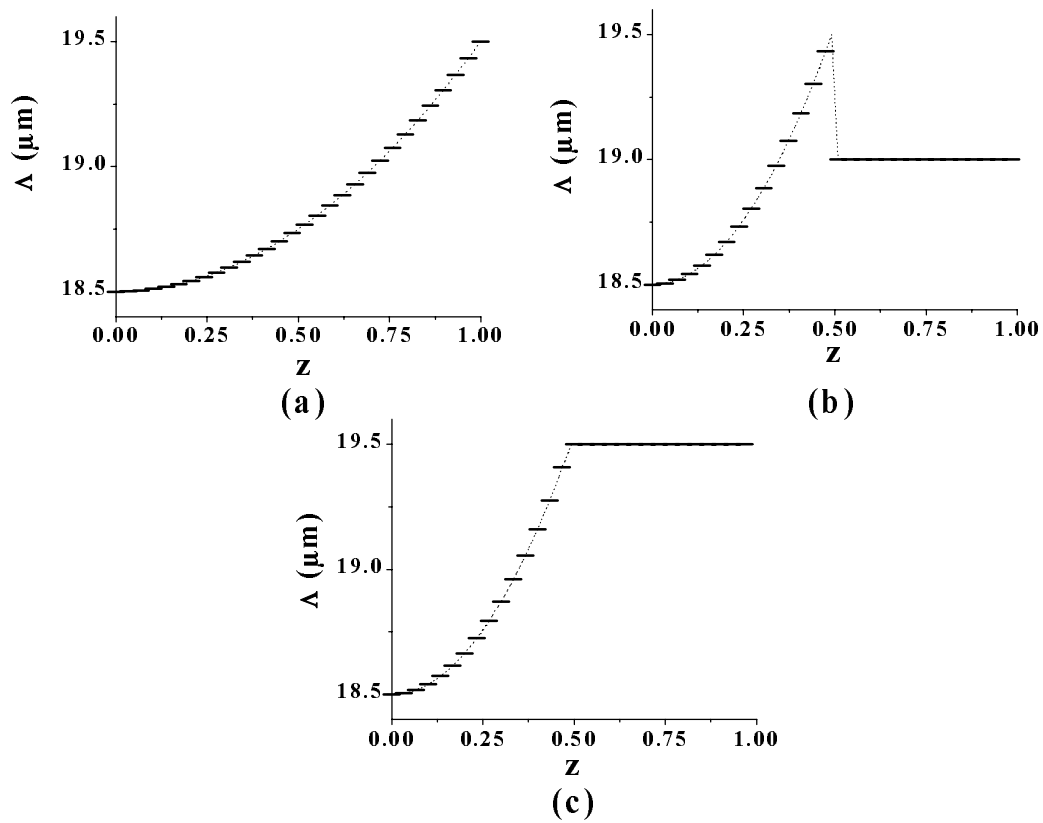


Figure 5.8 Engineer designs in a chirped PSW to observe controlled nonuniform profile response. (a) Quadratic grow (design 1), (b) quadratic grow with a sharp discontinuity (design 2), and (c) quadratic grow without the discontinuity (design 3).

Different segmented waveguide groups, with ten waveguides in each, were then fabricated with these designs. The mask was reproduced in both possible directions. For example using the “design 1” a quadratic growth and a quadratic decline in the grating period were duplicated in two different waveguides groups. This was done to observe reciprocal (or nonreciprocal) behavior in the same propagation direction within the material to isolate material imperfections. From the discussion at the beginning of this chapter we might expect a reciprocal response in the low depletion regime.

Representative low depletion SHG tuning curves for these waveguides are shown in Figure 5.9 for the 6 different possible combinations. All of these curves were obtained by end fire coupling into the same end of the device. In these curves we observed a broadening in the bandwidth of the SHG detuning curve relative to the uniform grating case (Figure 5.6) and a complicated dependence of SHG on the wavelength. By observing different waveguides within the same group we obtained a reproducible collective behavior. This can be observed in Figure 5.9 by comparing the two different detuning curves depicted for each case.

In all cases, 100 W of pulsed fundamental power was launched into the sample. On average a 20% throughput was observed. Considering 1.9 dB/cm losses (corresponding to ~65% throughput) and 15% Fresnel losses, the 40% coupling efficiency was consistent for this device. Correcting for losses, the average maximum conversion efficiencies obtained for 100 W of fundamental launched into the waveguide were 0.08%, 0.20% and 0.25% for the designs 1, 2 and 3, respectively. The curves in Figure 5.9 are normalized to these values.

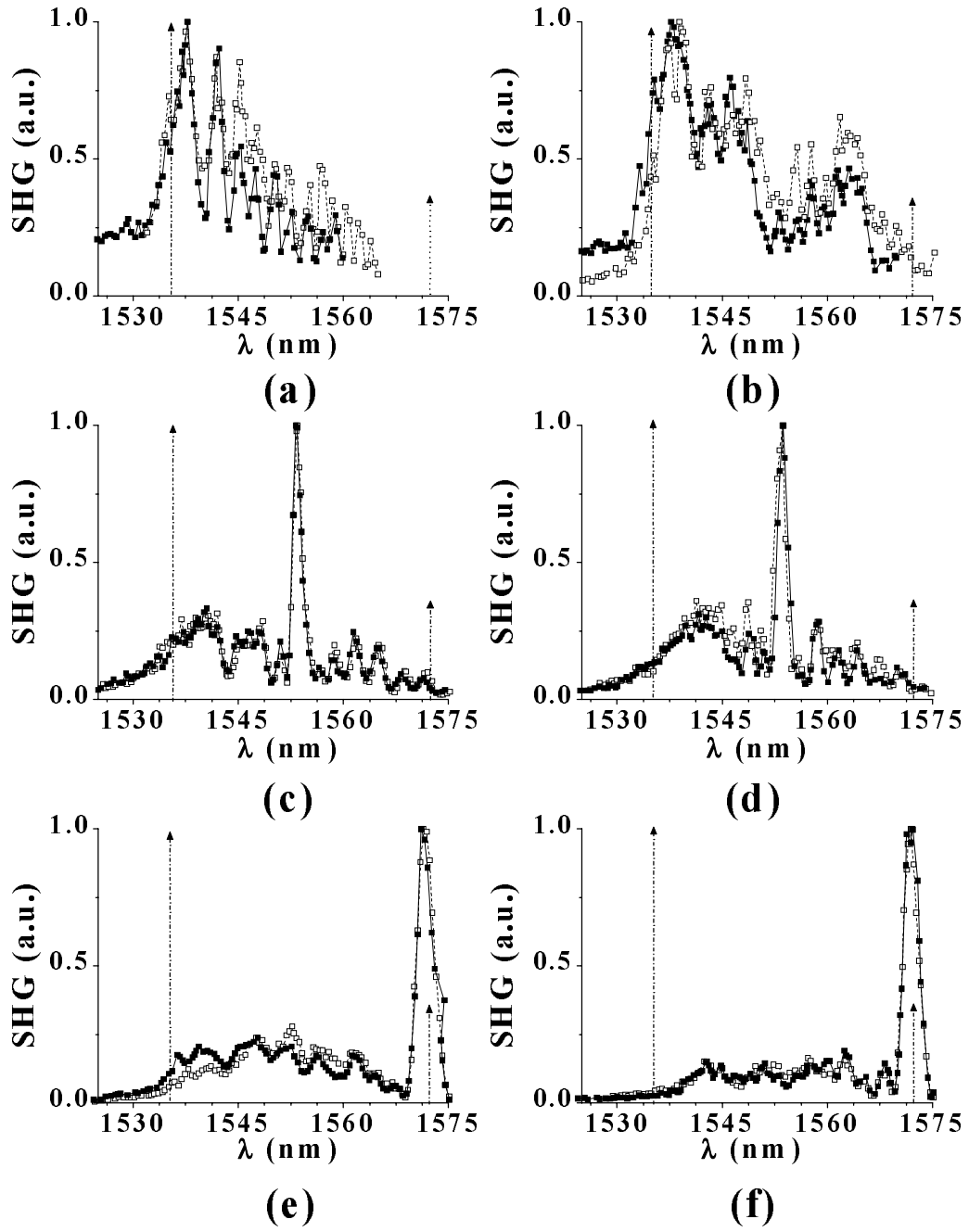
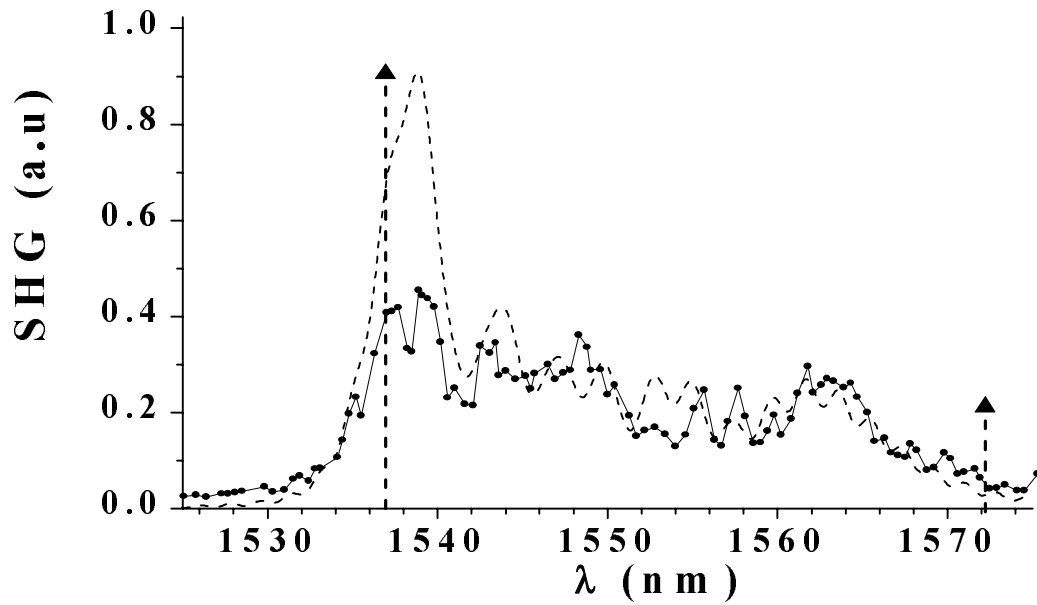


Figure 5.9 Experimental detuning curves for the spatial nonuniform profiles shown in Figure 5.8 in a chirped PSW. (a) Design 1 (forward), (b) Design 1 (backward), (c) Design 2 (forward), (d) Design 2 (backward), (e) Design 3 (forward), and (f) Design 3 (backward), Dotted arrows show the position for phasematching at the extremes values of the grating. Two different waveguides are shown in each graph to show reproducibility.

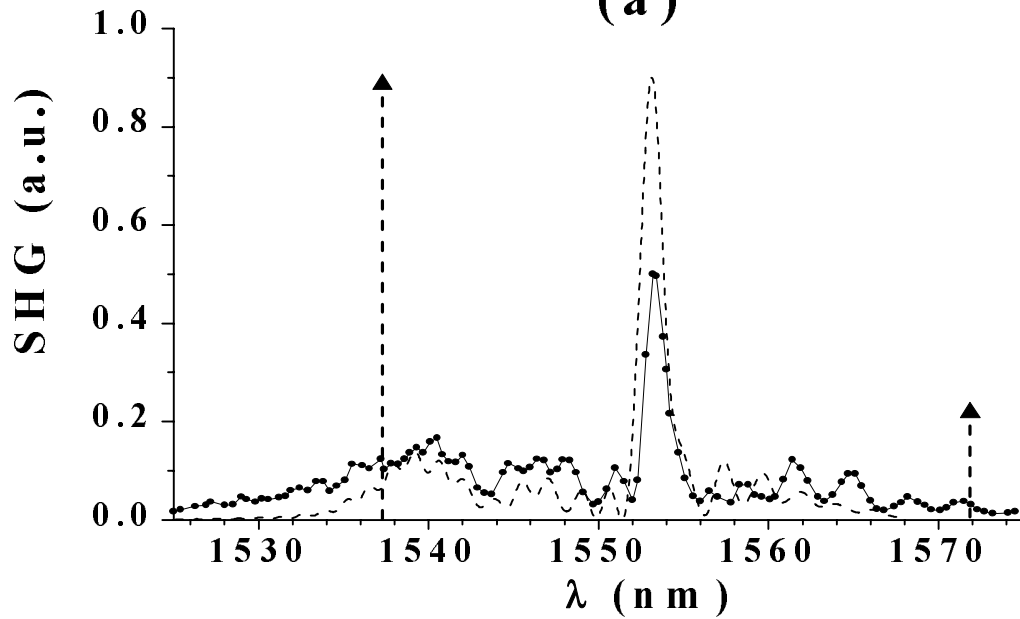
From these results, we observe that the detuning curves are limited to the region between ~ 1537 nm and ~ 1572 nm. This suggests that the $\text{TM}_{00}(\omega)\rightarrow\text{TM}_{01}(2\omega)$ interaction is responsible for the collective characteristics in the detuning curves shown. Comparing the result by endfire coupling into both sides of the device we may have expected a complementary behavior (curves on the right column replaced by the curves on the left column in Figure 5.9, and vice versa). Surprisingly this was not the case, although some degree of nonreciprocity was indeed present. This is a manifestation of a small contribution due to higher order effects such as multimode competition between $\text{TM}_{01}(2)$ and $\text{TM}_{20}(2\omega)$ for example. Some asymmetry in the waveguide due to discretization in the grating chirp (5.12) and defects in the mask are also possible causes for this lack of expected symmetry.

The curves depicted in Figure 5.9(a) and Figure 5.9(b) resemble the shape of the calculated curve in Figure 5.1(c) for a quadratic wavevector distribution. The main peaks in the other four curves correspond to the uniform grating at either the middle or the extreme grating values (Figure 5.8(b) and Figure 5.8(c)). From Figure 5.7, these values correspond to the $\text{TM}_{00}(\omega)\rightarrow\text{TM}_{01}(2\omega)$ interaction using first grating order assisted phasematching. This reinforces the assumption that this particular interaction is the main source for the details of the detuning curves shown in Figure 5.9.

Using a direct calculation with the wavevector mismatch distribution in Figure 5.8 and the result (5.6), it was possible to reproduce the experimental results shown in Figure 5.9. Two of these results are shown in Figure 5.10 for the designs 1 and 2 in the “backward” case (Figure 5.9(a) and (c) respectively). In these calculations the only fitted parameter was the amplitude of the function.



(a)



(b)

Figure 5.10 Detuning curves for the spatial nonuniform profiles shown in Figure 5.8 in a chirped PSW using 60 segments. Detuning curves (dashed line) were calculated using the engineer profile and (5.6). The amplitude of the profile was multiplied by 40.2. (a) Design 1 (backward) and (b) Design 2 (backward). Dotted arrows show the position for phasematching at the grating extremes Λ_0 and Λ_f for the interaction $TM_{00}(\omega) \rightarrow TM_{01}(2\omega)$.

Although the “backward” calculations shown here do not totally reproduce the peak’s magnitude shown in Figure 5.10, their position is correct. Most likely there are additional effects involved in this SHG process. To have a more complete description, the pulsed nature of the fundamental field input as well as other additional effects need to be included.

It is amazing to observe the similarity obtained for all the different curves, and all the curves required the same scale factor to within a 10% error. Therefore it is safe to assume that the nonuniform profile observed is mainly caused by the controlled nonuniform spatial chirp distribution along the propagation direction, affecting the $TM_{00}(\omega) \rightarrow TM_{01}(2\omega)$ resonance. The simple theory behind the low depletion calculation (5.6) reproduces these results in the first approximation. As a final comment on Figure 5.10, we mention that the detuning curves observed for the quadratic growth in the grating period (therefore the wavevector mismatch) as shown in Figure 5.9(a) exhibit the oscillatory behavior for most of the calculation exhibited in Figure 5.1(c). Such a typical shape for this detuning curve has been reported in some cases [13, 62] using different phasematching techniques. If the associated theory is correct for the wavelengths below the first peak (~ 1537 nm), a large cascaded nonlinear phase shift may be present.

The results shown in here are the first observation of a controlled, nonuniform chirped, grating assisted phase-matching with an arbitrary profile. The use of a PSW does not provide the best conversion efficiency, but it did allow better control of the grating chirp. These results are encouraging for the pursuit of all-optical switching devices at room temperature based on cascading, for new ways of enhancing the SHG bandwidth, etc. with a controlled the SHG evolution with an arbitrary, nonuniformly chirped grating.

CHAPTER 6

CONCLUSIONS

“Would you tell me, please, which way I ought to go from here?”

“That depends a good deal on where you want to get to,” said the Cat.

“I don’t much care where ---” said Alice.

“Then it doesn’t matter which way you go,” said the Cat.

“---- so long as I get somewhere,” Alice added as an explanation.

“Oh, you’re sure to do that,” said the Cat, “if you only walk long enough.”

Alice in Wonderland
Lewis Carroll

This dissertation has presented research which resulted in the identification of novel effects in waveguide second harmonic generation. This work started by investigating experimental and numerical inconsistencies that departed from the traditional scope of second harmonic generation. Some of these inconsistencies were caused by conditions usually overlooked while studying second harmonic generation, namely SHG in waveguides that support many modes and the SHG field evolution in waveguides with spatially nonuniform-

nonsymmetrical distribution of parameters along the propagation path. Examining second harmonic generation in detail under these conditions led to the identification of two fundamental effects in second harmonic generation, namely waveguide multimode competition and spatial nonreciprocity. This study provided additional mathematical tools to investigate the evolution of second harmonic generation for spatially nonuniform distribution of parameters along the propagation path further. In this chapter the basic results of this research will be summarized, conclusion will be drawn from these results.

6.1 Summary of Results

In this work some novel effects in waveguide second harmonic generation were investigated experimentally and numerically. A large amount of basic research remains to be done before the full potential limitations of these novel effects are appreciated. Additions to the SHG theory were incorporated by carefully explore the assumptions under which these effects are relevant. These additions were chosen to be as simple as possible, unfortunately the outcome is such that in order to anticipate the dynamics of these effects a numerical analysis is required. The experimental observations obtained in this dissertation were done in the 1490-1620 nm range using either QPM or segmented phasematched LiNbO₃ waveguides.

Examining the effective SHG detuning curves in waveguides that support many modes we found numerically that for one fundamental mode interacting with two second harmonic modes for low fundamental depletion (less than 10% conversion efficiency) or large “resonant” separation ($\Delta K_0 L$ larger than 25π) always behaved independently for the two

second harmonic modes. For larger depletion and/or closer separation, the two second harmonic modes "talk" to each other via the fundamental mode. Some general features that we found are that the wavelength and peak conversion efficiency for the two different harmonic modes change with input fundamental intensity and that power-dependent competition occurs between them at high powers. Additional study is required for mode interaction involving more than three modes. The phase-space of the interaction becomes complicated fast. Although the analysis and the experimental observation were done for SHG, it can be generalized to other second order processes. In summary, second harmonic generation can be a very complex process when multiple, closely spaced harmonic mode interactions are possible. Competition for power occurs due to the common coupling to the fundamental beam and the peak efficiency wavelength shifts due to the nonlinear phase shifts introduced by the neighboring mode. This effect has been predicted numerically and verified experimentally in QPM LiNbO₃ waveguides.

Observing the SHG field evolution in waveguides with spatially nonuniform distribution of parameters along the propagation path, a rich variety of effects were highlighted. The parameters that we are referring are the nonlinear coupling strength and the wavevector phase-mismatch between the fundamental and the second harmonic optical fields, combined in the mismatch response function $G(z)$. We developed a simple theory to describe the collective characteristics of nonuniform structures in four sets of the coupled mode equations suitable for description in different reference frames. The description ranges from a full description of the material characteristics at both frequencies, like for the equations type I, up to just the relative difference among the wavevectors as is the case for the equations

type IV. In the low depletion regime this simple theory leads to the elegant result (5.6). It consists on obtaining in a simple way the SHG detuning curve in the low depletion regime from knowledge of the axial spatial distribution of the wavevector mismatch and nonlinearity.

This theory now allows an additional tool for obtaining a spatially varying wavevector mismatch to tailor the SHG detuning curve. Experimentally this theory was confirmed in a controlled, nonuniform chirped, grating assisted PSW phase-matching with an arbitrary profile. The use of a PSW does not provide the best conversion efficiency, but it did allow better control of the grating chirp.

It has also been shown that in the case of SHG in a waveguide with an asymmetric wavevector mismatch, the outcome of the process depends on which side of the waveguide is the input end. Therefore, if a nonsymmetric condition for the mismatch response distribution is imposed, the SHG output depends on the direction into which the fundamental is launched and hence is spatially nonreciprocal. We have demonstrated numerically and experimentally the existence of spatial nonreciprocity in SHG in spatially nonsymmetrical structures, as a direct consequence of the perturbation in the coherent evolution between the fundamental and the second harmonic. This result was obtained in PSW LiNbO₃ waveguides with an arbitrary nonuniform-nonsymmetrical wavevector distribution and by introducing a sharp discontinuity in the wavevector mismatch and nonlinear coupling constant in a QPM LiNbO₃ waveguide.

In conclusion we observed a new kind of effects in waveguide second harmonic generation for: (a) SHG in waveguides that support many modes, and (b) the SHG field evolution in waveguides with spatially nonuniform-nonsymmetrical distribution of parameters along the propagation path.

For SHG in waveguides that support many modes some of the general features that we found are that the wavelength and peak conversion efficiency for different harmonic modes changes with input fundamental intensity and that power-dependent competition occurs between them at high powers. This is an important effect to consider, and if possible avoid, in the design of waveguides to be used for harmonic generation.

For the SHG field evolution in waveguides with spatially nonuniform-nonsymmetrical distribution of parameters along the propagation path we found that the SHG output depends on the direction into which the fundamental is launched and hence is spatially nonreciprocal. This opens the possibility for an optical diode using second order processes. In a more general context the results obtained are encouraging for the pursuit of all-optical switching devices at room temperature based on cascading, for new ways of enhancing the SHG bandwidth, etc. with a controlled the SHG evolution with an arbitrary, nonuniformly chirped grating.

REFERENCES

- [1] J. A. Armstrong, N. Blombergen, J. Ducuing and P. S. Pershan, "Interaction between light waves in a nonlinear dielectric," *Phys.Review* **127**, 6 (1962).
- [2] G. I. Stegeman, E. M. Wriqth, N. Finlayson, R. Zanoni, and C. T. Seaton, "Third order nonlinear integrated optics," *J.Lightwave Tech.* **QE-6**, 953 (1988).
- [3] G. P. Agrawal, *Nonlinear Fiber Optics*, Academic Press, San Diego, 1989.
- [4] S. M. Jensen, "The nonlinear coherent coupler," *IEEE J.Quantum Electron.* **QE-18**, 1580 (1982).
- [5] R. De Salvo, D. J. Hagan, M. Sheik-Bahae, G. I. Stegeman, E. W. Van Stryland, and H. Vanherzeele, "Self-focusing and self-defocusing by cascaded second-order effects in KTP," *Opt.Lett.* **17**, 28 (1992).
- [6] M. L. Bortz, M. Fujimura and M. M. Feyer, "Increased acceptance bandwidth for quasi-phase-matched second-harmonic generation in LiNbO₃ waveguides," *Elect.Lett* **30** 1 (1994).
- [7] J. Wu, T. Kondo, and R. Ito, "Optimal design for broadening quasi-phase-matched second-harmonic generation using simulated annealing," *IEEE J.Lightwave Tech.* **13**, 3 (1995).
- [8] P. Franken, A. E. Hill, C. W. Peters and G. Weinreich, "Generation of optical harmonics," *Phys.Rev.Lett* **7** 118 (1961).
- [9] L. A. Ostrovskii, "Self-action of light in crystals," *JETP Lett (Eng.Transl.)* **5**, 272 (1967).
- [10] Y. N. Karamzin and A. P. Sukhorukov, "Nonlinear interaction of diffracted light beams in a medium with quadratic nonlinearities: mutual focusing of beams and limitations on the efficiency of optical frequency convertors," *JETP Lett.* **20**, 339 (1974).
- [11] Y. N. Karamzin and A. P. Sukhorukov, "Mutual focusing of high-power light beams in media with quadratic nonlinearity," *Zh.Eksp Teo.Fiz* **68**, 834 (1975). (*Sov. Phys.-JETP* **41**, 414 (1976)).

- [12] M. L. Sundheimer, Ch. Bosshard, E. W. VanStryland, G. I. Stegeman and J. D. Bierlein, "Large nonlinear phase modulation in quasi-phasematched KTP waveguides as a result of second-order processes," *Opt. Lett.*, **18**, 1397 (1993).
- [13] Y. Baek, R. Schiek and G. I. Stegeman, "All-optical response of a hybrid Mach-Zender interferometer due to the cascaded nonlinearity," *Opt. Lett.*, **20**, 21 (1995).
- [14] D. J. Hagan, M. Sheik-Bahae, Z. Wang, G. I. Stegeman and E. W. VanStryland, "Phase controlled transistor action by cascading second-order nonlinearities in KTP," *Opt. Lett.*, **19**, 1305 (1994).
- [15] R. Schiek, Y. Baek, G. I. Stegeman, "One-dimensional spatial solitons due to cascaded second-order nonlinearities in planar waveguides," *Phys. Rev. E* **53**, 1138 (1996).
- [16] W. E. Torruellas, Z. Wang, D. J. Hagan, E. W. Van Stryland, G. I. Stegeman, L. Torner, and C. R. Menyuk, "Observation of two-dimensional spatial solitary waves in a quadratic medium," *Phys.Rev. Lett.* **74**, 5036 (1995).
- [17] F. A. Hopf and G. I. Stegeman *Applied Classical Electrodynamics, Vol. 2 Nonlinear Optics* John Willey & Sons, New York, 1986.
- [18] R. W. Boyd, *Nonlinear Optics*, Academic Press, Boston, 1992.
- [19] Y. R. Shen, *The Principles of Nonlinear Optics*, Wiley, New York, 1983.
- [20] M. Born and E. Wolf, *Principles of Optics*, 6th Ed., Pergamon Press, Oxford, 1980.
- [21] P. Franken, A. E. Hill, C. W. Peters and G. Weinreich, "Generation of optical harmonics," *Phys.Rev.Lett.*, **7**, 118 (1961).
- [22] R. Loudon, "Theory of non-linear optical processes in semiconductors and insulators," *Proc.Phys.Soc.* **80**, 952, (1962).
- [23] J. E. Midwinter and J. Warner, *Brit.J.Appl.Phys.* **16**, 1135 (1965).
- [24] A. Yariv, *Quantum Electronics*, John Wiley & Sons, 3rd Edition, New York (1988).
- [25] R. C. Eckart and J. Reintjes, "Phase matching limitations of high efficiency second harmonic generation," *IEEE J.Quantum Electron.* **QE-20**, 1178, (1984).
- [26] M. Jäger and G. I. Stegeman, "Model dispersion phase matching over 7 mm length in overdamped polymeric chain waveguides," *Appl.Phys.Lett* **69**, 4139 (1996).

- [27] L. Torner, D. Mazilu, and D. Michalache, "Walking solitons in quadratic nonlinear media," *Phys.Rev.Lett.* **77**, 2455 (1996).
- [28] Y. Ueno, G. I. Stegeman and K. Tajima, "Large phase shift due to $\chi^{(2)}$ cascading nonlinearity in large-walk-off and loss regimes in semiconductors and other dispersive materials," *Jpn.J.Appl.Phys* **36**, 613 (1997).
- [29] M. M. Feyer, G. A. Magel, D. H. Jundt, and L. Byer, "Quasi-phase-matched second harmonic generation: tuning and tolerances," *IEEE J.Quantum Electron.* **28**, 2631 (1992).
- [30] T. Suhara and H. Nishihara, "Theoretical analysis of waveguide second-harmonic generation phase matched with uniform and chirped gratings," *IEEE J.Quant. Elec.* **26**, 1265 (1990)
- [31] C. J. Van der Poel, J. D. Bierlein, J. B. Brown, and S. Colak, "Efficient type I blue second-harmonic generation in periodically segmented KTiOPO₄ waveguides," *Appl.Phys.Lett.* **57**, 2074 (1992).
- [32] G. I. Stegeman and C. T. Seaton, "Nonlinear integrated optics," *J.Appl.Physics*, **58**, R57 (1985).
- [33] E. J. Lim, M. M. Fejer, R. L. Byer, and W. J. Kozlovsky, "Blue light generation by frequency domain in periodically poled lithium niobate channel waveguide," *Electron.Lett.* **25**, 174 (1989).
- [34] C. G. Treviño-Palacios, G. I. Stegeman, M. P. De Micheli, P. Baldi, S. Nouh, D. B. Ostrowsky, D. Delacourt, and M. Papuchon, "Intensity dependent mode competition in second harmonic generation in multimode waveguides." *Appl.Phys.Lett* **67**, 170 (1995).
- [35] C. A. Balanis, *Advance Engineering Electromagnetics*, John Wiley & Sons, New York (1989).
- [36] D. Marcuse, *Theory of Dielectric Optical Waveguides*, Academic Press, New York, (1974).
- [37] D. L. Lee, *Electromagnetic Principles of Integrated Optics*, John Wiley & Sons, New York, (1986).
- [38] N. S. Kapany and J. J. Burke, *Optical Waveguides*, Academic Press, New York (1972).
- [39] T. Tamir, *Guide-Wave Optoelectronics*, Springer-Verlag, New York (1988).

- [40] G. I. Stegeman, "Nonlinear guided wave optics" in *Contemporary Nonlinear Optics*, G. P. Agrawal and R. W. Boyd eds., Academic Press. New York (1992).
- [41] R. Schiek, "Nonlinear refraction caused by cascaded second-order nonlinearity in optical waveguide structures," *J.Opt.Soc.Am. B*, **10** 10 (1993).
- [42] D. Delacourt, F. Armani, and M. Papuchon, "Second harmonic generation efficiency in periodically poled LiNbO₃ waveguides," *IEEE J.Quantum Elec.* **QE-30**, 1090 (1994).
- [43] P. Baldi, C. G. Treviño-Palacios, G. I. Stegeman, M. P. De Micheli, D. B. Ostrowsky, D. Delacourt, and M. Papuchon, "Simultaneous generation of red, green and blue light in room temperature periodically poled lithium niobate waveguides using single source," *Elect.Lett.* **31**, 1350 (1995).
- [44] P. Baldi, S. Nouh, M. P. De Micheli, D. B. Ostrowsky, D. Delacourt, X. Banti, and M. Papuchon, "Efficient quasi-phase matched generation of parametric fluorescence in room temperature lithium niobate waveguides," *Electron.Lett.* **29**, 1539 (1993).
- [45] J. A. Giordmaine and R. C. Miller "Tunable coherent parametric oscillation in a periodically domain-inverted LiNbO₃ at optical frequencies," *Phys.Rev.Lett.* **14**, 973 (1965).
- [46] N. Uesugi, "Parametric difference frequency generation in a three-dimensional LiNbO₃ optical waveguide," *Appl.Phys.Lett* **36**, 178 (1980).
- [47] M. L. Sundheimer, A. Villeneuve, G. I. Stegeman, and J. D. Berlein, "Simultaneous generation of red, green and blue light in a segmented KTP waveguide using a single source," *Electon.Lett.* **30**, 1919 (1994).
- [48] J. Webjorn, V. Pruneri, P. St. J. Russell, J. R. M. Barr, and D. C. Hanna, "Quasi-phase-matched blue light generation in bulk lithium niobate electrically poled via periodic liquid electrodes," *Electron.Lett.* **30**, 894 (1994).
- [49] Y. P. Svirko and N. I. Zheludev, "Reversibility of optical interactions in noncentrosymmetric media," *Opt.Lett.* **17**, 1809 (1995).
- [50] C. G. Trevino-Palacios, G. I. Stegeman, and P. Baldi "Spatial nonreciprocity in waveguide second order processes," *Opt.Lett.* **21** 1442 (1996).
- [51] K. Mizuuchi, K. Yamamoto, M. Kato, and H. Sato, "Broadening of phase-matching bandwidth in quasi-phase-matched second-harmonic generation," *IEEE J.Quantum Elec.*, **30**, 1596 (1994).

- [52] S. Helmfrid and G. Arvidsson, "Influence of randomly varying domain lengths and nonuniform effective index on second-harmonic generation in quasi-phase-matching waveguides," *J.Opt.Soc.Am.B*, **8**, 797, (1991).
- [53] J. Trull, R. Vilaseca, J. Martorel, and R. Corbala, "Second-harmonic generation in local modes in a truncated periodic structure," *Opt.Lett* **20**, 1746 (1995).
- [54] M.L. Bortz, M. Fujimura, and M.M. Feyer, "Demonstration of artificially structured tuning curves and enhanced acceptance bandwidth for quasi-phaseshifted frequency conversion in LiNbO₃ waveguides," *Electron.Lett* **30**,34 (1994).
- [55] R. Bracewell, "The Fourier Transform and its Applications" MacGraw-Hill, New York, p.112 (1965).
- [56] M. Nazarathy and D. W. Dolfi, "Spread-spectrum nonlinear optical interactions: Quasi-phaseshift with pseudorandom polarity reversals," *Opt.Lett.* **12**, 823 (1987).
- [57] S. Helmfrid, G. Arvidsson, and J. Webjörn, "Influence of various imperfections on the conversion efficiency of second-harmonic generation in quasi-phase-matching lithium niobate waveguides," *J.Opt.Soc.Am.B* **8**, 797, (1991).
- [58] F. R. Nash, G. Boyd, M. Sargent III, and P. M. Bridenbaugh, "Effect of optical inhomogeneities on phase matching in nonlinear crystals," *J.Appl.Phys.* **41**, 2564 (1970).
- [59] Y. Baek, R. Schiek, G.I. Stegeman, G. Krijnen, I. Baumann, and W. Sohler, "All-optical integrated Mach-Zender switching due to cascaded nonlinearities," *Appl.Phys.Lett.* **68**, 2055 (1996).
- [60] D.C. Hutchings, M. Sheik-Bahae, D.J. Hagan, and E.W. Van Stryland, "Kramers-Krönig relations in nonlinear optics," *Opt. Quantum Electron.* **24**, 1 (1992).
- [61] L. Kador, "Kramers-Krönig relations in nonlinear optics," *Appl.Phys.Lett.* **66**, 2938 (1995).
- [62] P. G. Kazansky, V. Pruneli, O. Sugihara, L. Dong, and P. St J. Russell, "CW quasi-phase-matched second-harmonic generation of blue light in poled optical fiber," *CLEO proceedings*, paper **CthE2**, OSA (1995).
- [63] L. S. Yu, Q. Z. Liu, S. A. Pappert, P. K. L. Yu, and S. S. Lau, "Laser spectral linewidth dependence on waveguide loss measurement using the Fabry-Perot method," *Appl.Phys.Lett* **64**, 536 (1994).